Beauty Production in π^-A collisions at 530 *GeV/c*

BY

RICHARD JESIK
B.S., Wichita State University, 1986
M.S., University of Illinois at Chicago, 1989

THESIS

Submitted as partial fulfillment of the requirements
for the degree of Doctor of Philosophy in Physics
in the Graduate College of the
University of Illinois at Chicago, 1993

Chicago, Illinois

THE UNIVERSITY OF ILLINOIS AT CHICAGO
Graduate College
CERTIFICATE OF APPROVAL

5-28-1993

I hereby recommend that the thesis prepared under my supervision by

Richard Jesik

entitled **Beauty Producation In π^- A Collisions at 530 GeV/c**

be accepted in partial fulfillment of the requirements for the degree of

Doctor of Philosophy

S. Magurno
Adviser (Chairperson of Defense Committee)

I concur with this recommendation Uday Sukhatme
Department Head/Chair

Recommendation concurred in:

S. Magurno
H. Haggerty
Tom Kirk
Dennis Perkins
[illegible]

Members of Thesis or Dissertation Defense Committee

UIC The University of Illinois at Chicago

This thesis is dedicated to my wife, Kendra Jo Jesik, who's love and support made it all possible.

ACKNOWLEDGMENTS

This thesis is the culmination of six years of education and work at the University of Illinois at Chicago and in Fermilab experiment E672. It is impossible to give proper recognition to all who have contributed to this work, and I apologize up-front to anyone I have overlooked.

Foremost, I want to thank my thesis advisor, Seymore Margulies, for his guidance, encouragement, and attention to detail over the years (not to mention his endless paperwork battles to keep our funding coming). I greatly appreciate the many opportunities he has provided for me, and the freedom he has given me in the last few years while working on the analysis presented in this thesis. I would also like to thank my other two advisors at UIC, Howard Goldberg and Julius Solomon. Julius was a wonderful guide through the Vax and Fortran world, teaching me to fear no computer or piece of code. Howard's enthusiasm for new physics has inspired me on many occasions and his other enthusiasms have brightened many a dull day (if only he would wise-up and find a *major* league baseball team to support). From these three gentlemen, I have received a near perfect mix of guidance, support, inspiration, and freedom.

I would like to thank the other professors, staff, and students at UIC who have made my studies here interesting and enjoyable; especially my other thesis committee members Wai Yee Keung and Tom Imbo. I learned most of my high-energy theory from Yee in what was the best class I have ever taken, and Tom schools me, almost daily, on the basketball court.

Andrzej Zieminski, the spokesman of experiment E672, has helped me in more ways than I can begin to mention. He has taught me very much, and his trust in me during the run, and later on in the analysis of the data, has allowed me to grow as a physicist. The other members of our collaboration have also been much help to me; thanks to the Victors, the Sashas, Kartik, Andrei, Loretta, Tom, and Hector. Jack Martin and Volodia Sirotenko deserve special thanks. I have benefited greatly from Volodia's expertise in Monte Carlo and physics analysis; much of the work presented in this thesis is the result of our many discussions. All of the results presented in this thesis are a direct consequence of Jack Martin's tracking wizardry. I have learned (and am still learning) much from him. I would also like to thank my fellow E672 graduate students Rui Li and Francisco Vaca. I have really enjoyed working and learning with you.

The members of our sister (sometimes evil step-sister) experiment E706 also deserve many thanks. All kidding aside, the E706 tracking system was essential to this work. I would like to especially thank George Ginther for his help while we were running, and also for his hard questions about my analysis, which helped make it all the more solid (Andrzej deserves credit for this also). Thanks to all the E706 collaborators who made me feel welcome at the lab: Rob (who took all my data for me and even showed me where the J/ψ was), Nick, Mani (who helped get me started in B physics), Dane, Brij, Dhammika, V.J., Casey, Chris, Dan, Lucy, Jim, Steve, Lenny, Paoti... etc.

I especially want to thank my family for the love and support that they give me.

RLJ

TABLE OF CONTENTS

TABLE OF CONTENTS (continued)

TABLE OF CONTENTS (continued)

LIST OF TABLES

LIST OF FIGURES

LIST OF FIGURES (continued)

LIST OF FIGURES (continued)

LIST OF FIGURES (continued)

LIST OF FIGURES (continued)

SUMMARY

Beauty hadroproduction was investigated in at the Fermilab Tevatron by experiment E672/E706 using a large-aperture, open-geometry spectrometer with the capability of studying high-mass muon pairs. The E672 muon spectrometer consisted of a toroid magnet with proportional wire chambers (PWCs) located both upstream and downstream of the magnet. Two scintillation counter hodoscopes were also located in the muon detector for triggering purposes. The upstream part of the charged particle tracking system consisted of a 16-plane silicon microstrip vertex detector, a dipole magnet, and a PWC-strawtube array. Dimuon pretriggers were formed by coincidences between interaction counters and the muon hodoscopes. A fast (10 μs) processor calculated the effective mass of track combinations in the muons system and generated a trigger if the mass was above an adjustable value.

Data was taken during the 1990 Fermilab fixed-target run using a negative pion beam with 530 GeV/c momentum incident on Cu and Be targets. Approximately 5 million dimuon triggers were recorded (corresponding to a luminosity of 8 pb^{-1}) yielding approximately twelve-thousand reconstructed $J/\psi \rightarrow \mu^+\mu^-$ events. Bs were detected through their decay modes with J/ψ in the final state. Since the B decays weakly it travels on the order of a cm before decaying; these decays are therefore characterized by J/ψs emerging from secondary vertices.

A dimuon-oriented secondary-vertex finding procedure was developed, and after extensive quality cuts, a sample of 73 secondary vertex J/ψ events was found. A significant background to the signal of secondary vertex J/ψs from B decays is from events in which a high-momentum particle produced in the primary collision interacts further downstream in

the target and produces a J/ψ (secondary interactions). Ten of the 73 events have the J/ψ vertex clearly in a region where only air is present; the background from secondary interactions is negligible for these events. A beauty cross-section of (28 ± 9 ± 8) nb/nucleon in the forward direction ($x_F > 0.1$) was extracted from the air-gap secondary-vertex J/ψ signal. Extrapolating this cross section to all x_F regions gives a total cross-section on the order of forty nb/nucleon.

The sample of 73 secondary vertex J/ψ events was searched for the exclusive decay modes $B^{\pm} \rightarrow J/\psi + K^{\pm}$, and $B^0 \rightarrow J/\psi + K^{0*}$. In these decays, all the final state particles are charged, which gives an opportunity to fully reconstruct the B mass and lifetime. A Monte Carlo driven procedure and set of cuts was developed which yielded 5 events with a reconstructed invariant mass in the expected B range.

CHAPTER 1

INTRODUCTION

This thesis presents results from Fermilab experiment E672, specifically on the hadroproduction of b-hadrons. Experimental studies of heavy-quark production provide important information for our understanding of the strong interaction. Experiment E672 was designed to look at processes that result in multiple muons in the final state: specifically Drell-Yan and heavy-quark (c, b) production. Heavy quark QCD production diagrams up to order α_s^3 have been calculated [1], and predictions have been made for the beauty cross section [1, 2]. Measurements of this cross section, as well as being a test of QCD, provide information on the parameters of the calculation such as the b-quark mass, the QCD factorization/renormalization scale μ, and parton distribution functions. Interest in beauty production has been generated by predictions of significant $B\overline{B}$ mixing in which CP violation may be present and observable. While E672 is statistically limited in this study, the analysis methods described in this thesis as well as the total B-meson cross-section measurement presented are useful information for future high-statistics "b-factory" experiments.

1.1 Theoretical overview

The lowest order ($O(\alpha_s^2)$) QCD tree level diagrams for open heavy-quark production are shown in Figure 1.1. In these interactions, either two gluons fuse or a light quark annihilates with a light antiquark to produce a heavy quark-antiquark pair:

$$gg \rightarrow Q\overline{Q}, \qquad q\overline{q} \rightarrow Q\overline{Q}.$$

Internal lines in these diagrams are off-shell by order of the heavy-quark mass (M_Q) leading

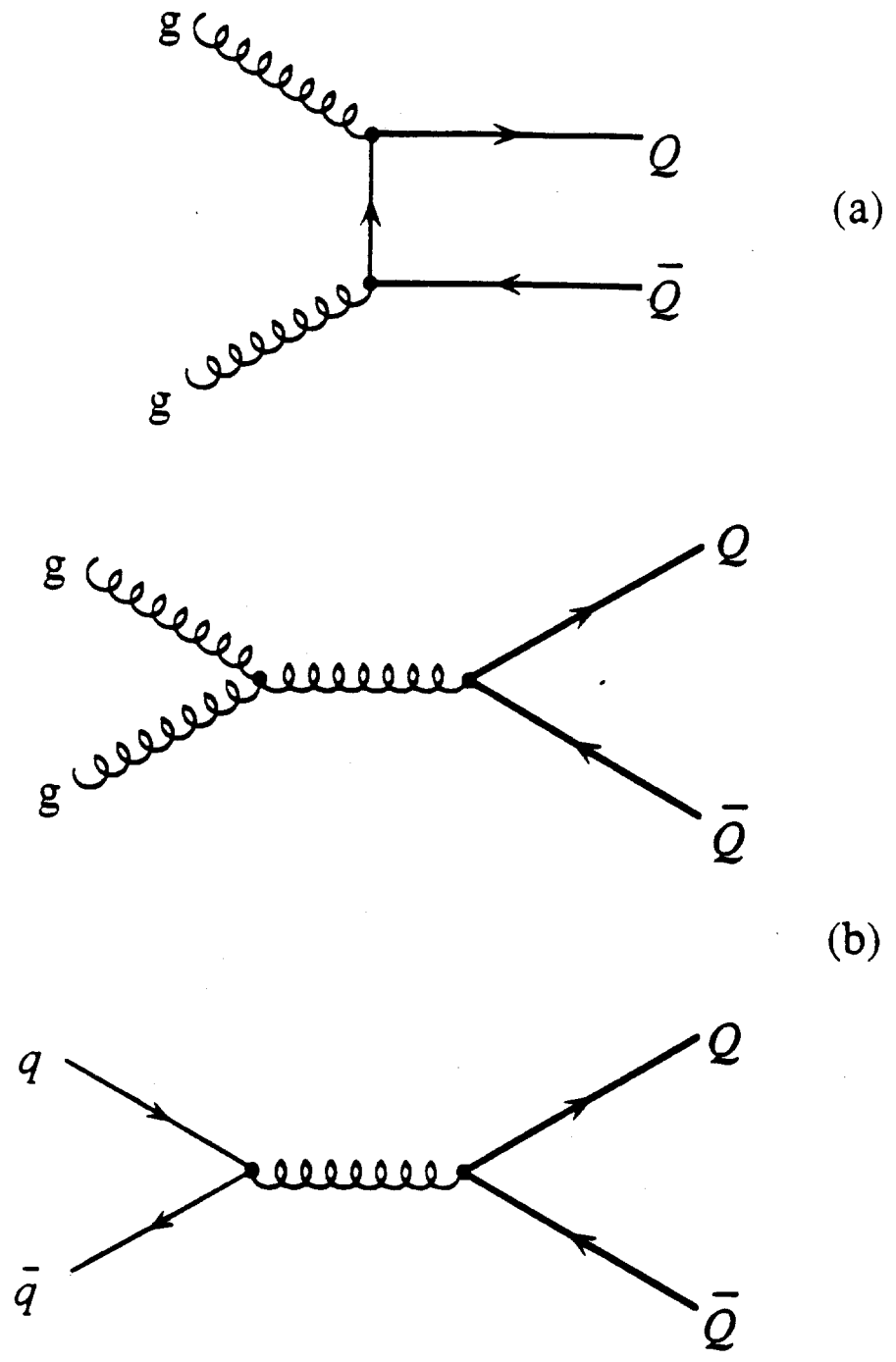

Figure 1.1. Lowest order ($O(\alpha_s^2)$) QCD tree-level diagrams for heavy quark hadroproduction: (a) gluon fusion; (b) quark-antiquark annihilation.

to a short-range interaction; perturbation theory is therefore justified in the cases of large M_Q [3].

The dynamical properties of the lowest order diagrams are as follows: The Q and $\overline{Q}$ are produced back-to-back in the parton-parton center-of-mass system. Hadronization of the quarks to their final state introduces some smearing, but the B and the $\overline{B}$ should also be found approximately back-to-back. Since the parton momentum is almost exclusively in the longitudinal direction (neglecting k_T smearing of the target partons), the resultant transverse momentum of the $B\overline{B}$ pair should be essentially zero. The mean transverse momentum of the separate quarks is predicted to be on the order of their mass, and since the parton densities in both the beam and target fall off rapidly with the parton's fractional momentum, the quarks should be produced in the central region of the scaled longitudinal momentum variable, x_F [4]. The subprocess cross sections, $\hat{\sigma}$, are predicted to be proportional to $\alpha_s^2/\hat{s}$ [4], where $\hat{s}$ is the square of the parton-parton center-of-mass energy, $\hat{s} = (p_1 + p_2)^2$, with p_1 and p_2 being the beam parton and target parton four-momentum, respectively.

Examples of the order α_s^3 processes are shown in Figure. 1.2. They include virtual corrections to the lowest-order diagrams and processes in which two partons interact to produce a $Q\overline{Q}$ pair plus a third light quark or gluon:

$$gg \rightarrow Q\overline{Q}g, \qquad gg \rightarrow Q\overline{Q}q.$$

In addition to the gluon fusion and quark-antiquark annihilation processes, initial-state gluon-quark interactions are present to this order:

$$gq \rightarrow Q\overline{Q}q, \qquad g\overline{q} \rightarrow Q\overline{Q}\overline{q}.$$

These $2 \rightarrow 3$ processes have final-state topologies that can be quite different from those of the lower-order $2 \rightarrow 2$ processes; e.g., the presence of an extra jet in the final state means that the $Q\overline{Q}$ pair may no longer be back-to-back.

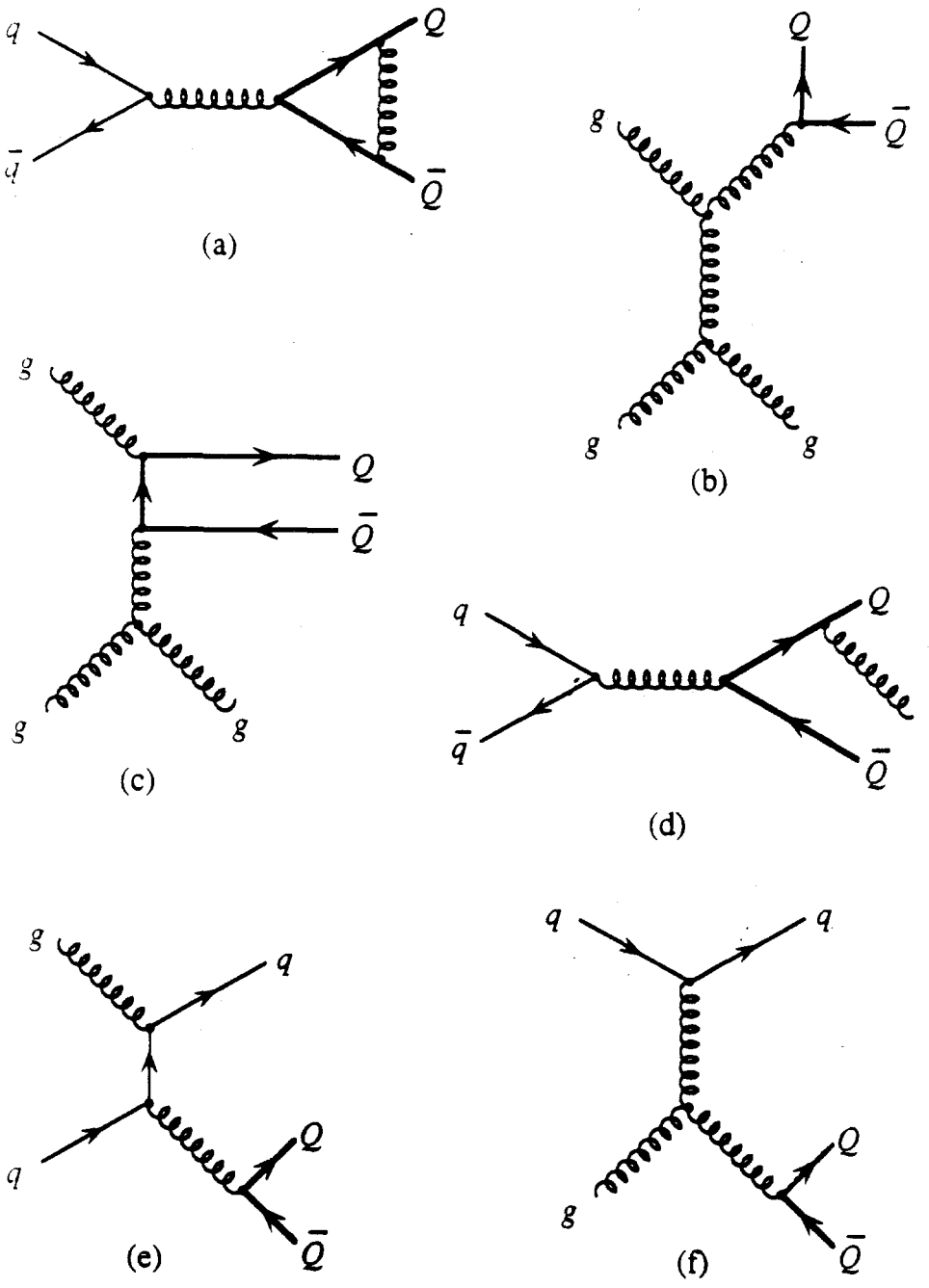

Figure 1.2. Examples of next-to-leading-order ($O(\alpha_s^3)$) heavy-quark hadroproduction diagrams: (a) virtual corrections to lowest-order ($O(\alpha_s^2)$) diagrams; (b, c) gluon splitting; (d) gluon emission; (e, f) quark-gluon initial-state interactions.

The heavy quark inclusive cross-section is expressed as a convolution of the hard-scattering subprocess cross-sections ($\hat{\sigma}_{ij}$) and the parton density functions of the beam particle and target nucleus summed over the possible light parton initial states:

$$\sigma(s,M_Q^2) = \sum_{ij} \int_0^1 dx_1 \int_0^1 dx_2\, G_{j/2}(x_2,\mu) G_{j/2}(x_2,\mu) \hat{\sigma}_{ij}(\hat{s}, M_Q, \mu, \alpha_s(\mu)). \qquad (1.1)$$

In this expression, index 1 refers to the beam particle's parameters, and 2 refers to those of the target nucleus. The *i* and *j* indices refer to the type of partons involved in the interaction: gluons, light quarks (*u*, *d*, *s*, and *c*), or antiquarks; *x* is the parton fractional momentum; and the *G* functions are the parton densities which represent the probability of finding a parton at a particular value of *x*. M_Q is the heavy quark mass; μ is the QCD factorization/evolution scale; *s* and $\hat{s}$ are the squares of the center-of-mass energy in the beam-target and parton-parton systems, respectively ($\hat{s} = x_1 x_2 s$); and α_s is the strong coupling constant.

It is important to note that Equation 1.1 is based on the assumption of parton model factorization. The parton density functions and subprocess cross-sections are assumed to be universal process-independent properties of the initial state hadrons. This assumption is common to many perturbative QCD calculations, but it is by no means trivial; for example gluon exchange between the "spectator" and interacting partons can modify the parton density functions. Arguments for the validity of factorization in heavy-quark production can be found in Refs. [3] and [5].

Complete calculations of the hard-scattering subprocess cross-sections to order α_s^3 have been performed by Nason, Dawson, and Ellis (NDE) [1].

They express the cross sections as

$$\hat{\sigma}_{ij}(\hat{s}, M_Q, \mu, \alpha_s(\mu)) = \frac{\alpha_s^2(\mu^2)}{M_Q^2} f_{ij}\left(\rho, \frac{\mu^2}{M_Q^2}\right), \tag{1.2}$$

where $\rho = 4M_Q^2/\hat{s}$. The f_{ij} functions are expressed as a perturbative expansion

$$f_{ij}\left(\rho, \frac{\mu^2}{M_Q^2}\right) = f_{ij}^{(0)}(\rho) + 4\pi\alpha_s(\mu^2)\left[f_{ij}^{(1)}(\rho) + \bar{f}_{ij}^{(1)}(\rho)\ln\left(\mu^2/M_Q^2\right)\right] + O(\alpha_s^2), \tag{1.3}$$

and calculated using an extension of the $\overline{\text{MS}}$ renormalization and factorization scheme [6]. Explicit expressions for the set of functions f_{ij} can be found in Ref. [1].

It should be noted that the cross section determination is independent of μ only if all of the terms in the expansion are calculated. To calculate the inclusive beauty cross-section for pion/proton collisions, Berger [2] uses the convolution expression (Eq. 1.1), with the NDE subprocess cross-sections; parton structure functions of Owens [7]; and sets M_Q = 5 GeV/c^2. Figure 1.3 shows his cross-section prediction as a function of beam momentum for two choices of the evolution scale, $\mu^2 = M_Q^2$, and $\mu^2 = 4M_Q^2$. A cross section on the order of tens of nanobarns is expected at E672's beam momentum of 530 GeV/c. Due to a different choice of parton structure functions, Berger's predictions are systematically higher than estimates made by NDE themselves [1], but the results are consistent within the theoretical uncertainties. The uncertainties in these calculations arise from the choice of evolution scale, the value of the heavy-quark mass, the form of the strong coupling constant, the renormalization/factorization scheme, and the choice of parton density functions.

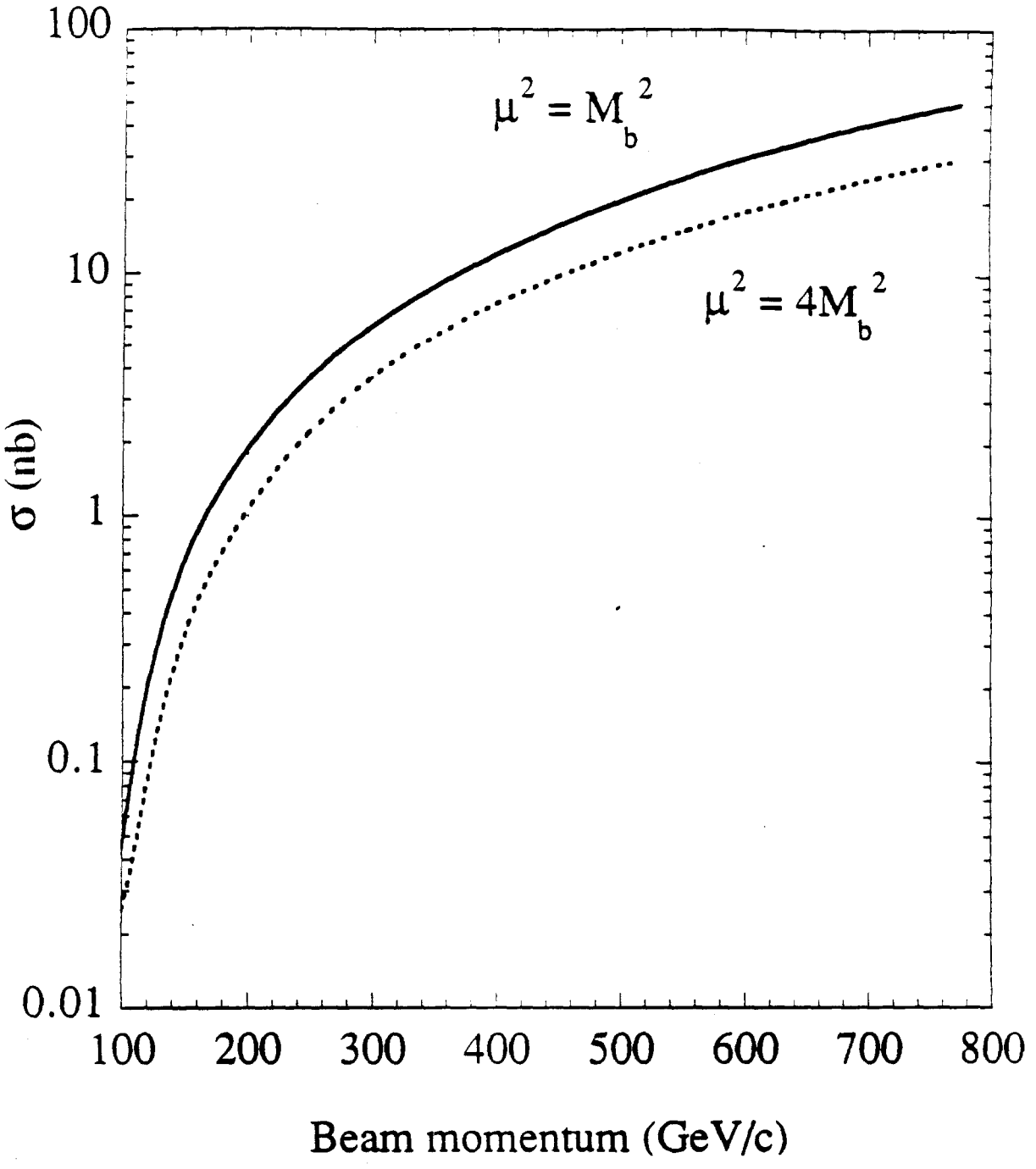

Figure 1.3 Berger's cross-section predictions through order α_s^3 for $\pi^- p \to b\bar{b} + X$ interactions as a function of lab momentum. Here, $M_b = 5\ GeV/c^2$ and two choices are shown for the evolution scale: $\mu^2 = M_b^2$ (solid line), and $\mu^2 = 4M_b^2$ (dashed line).

1.2 Previous experimental results

Since the first observation of a single $B\overline{B}$ pair by WA75 [8], experimental data on beauty hadroproduction has come from five experiments: NA10, WA78, UA1, CDF, and E653. All of these experiments observe Bs through decays containing leptons. CDF and UA1 have reconstructed invariant-mass signals in exclusive decay modes involving the J/ψ. In addition to these hadroproduction experiments, much information on B-mesons has come from e^+e^- accelerators. ARGUS and CLEO tune their beams to produce the upsilon $4S$ $b\overline{b}$ bound state which decays into $B\overline{B}$ pairs [9, 10], and the LEP experiments also observe Bs through the decay of the Z^0 into $b\overline{b}$ pairs [11]. Although many important results have come from these experiments, only hadroproduction results are reviewed in this section.

1.2.1 Collider experiments

Both the UA1 and CDF measurements were based on high p_T lepton samples. The UA1 analysis used a sample of 6103 events having muons with $p_T > 10$ GeV/c [12]. The muon was required to be isolated and the event is required to have at least one high p_T jet. Additional cuts were made to remove muons from W and Z decays. The relative p_T distribution of the muon with respect to the jet axis was fit to a Monte Carlo simulation of background and b production distributions. The result of this fit gave the fraction of $b\overline{b}$ events to be 33%. The cross-section (in bins of relative p_T) was calculated from this fraction, and is in good agreement with the NDE calculations [1]. CDF performed a similar analysis using its inclusive electron spectrum [13].

UA1 and CDF both obtained b-quark cross-sections using dimuons from J/ψ decays [14, 15]. The J/ψ p_T distribution was fit using a Monte-Carlo simulation of direct charmonium

and b production with subsequent decay into J/ψ. CDF has been able to reconstruct the exclusive decay modes $B^{\pm} \rightarrow J/\psi + K^{\pm}$, and $B^{0} \rightarrow J/\psi + K^{*0}$ (and its charge conjugate) [13, 16]. UA1 has also been able to reconstruct the $J/\psi + K^{*0}$ exclusive channel, as well as a signal for the decay $\Lambda_b \rightarrow J/\psi + \Lambda$ [17]. These experiments have demonstrated the usefulness of the J/ψ as a tag for b production.

It should be noted that all of the CDF b-quark cross section measurements (from inclusive electron, inclusive and exclusive J/ψ modes) are systematically higher than the NDE predictions at the level of 1.5 standard deviations [16].

1.2.2 Fixed-target experiments

NA10 and WA78 are CERN beam-dump experiments. These experiments consist of a beam dump which absorbs all of the hadronic and electromagnetic energy of the primary interaction, followed by a muon spectrometer. NA10 used an incident pion beam of 286 G*eV/c* momentum, and studied reactions with three muons in the final state [18]. This state is a signature of double semileptonic $B \rightarrow D$ cascade decays in which both *B*s in the event result in muons and one of the *D*s decays semileptonically as well. There are, however, large backgrounds to this signal, the largest being double semileptonic $D\overline{D}$ decay events in which a beam halo muon is also present. NA10 analyzed events that had a muon above a minimum transverse momentum to increase the signal-to-background ratio and obtained a three muon sample that is estimated to be 15% due to $B\overline{B}$ decays. Assuming A^1 target nuclear-number dependence, they obtained a cross section of [19]

$$\sigma_{B\overline{B}} = (14\ ^{+7}_{-6})\ \text{nb/nucleon.}$$

The muon acceptance used in this calculation was based on a "unrealistic" model of heavy

quark production, and the extrapolated cross section is therefore thought to be a factor of two or so too high [2].

WA78 also studied the production of three muon final states using a 320 GeV/c pion beam [19]. Their beam dump was equipped for calorimetric measurement, so cuts could be made on missing energy from neutrinos in addition to muon p_T in order to increase the B signal-to-background ratio. They were also able to perform a similar analysis using like-sign dimuons. After cuts, they were left with a sample of 68 like-sign dimuon events and 11 three muon events. The estimated backgrounds to these signals are 5 and 1 event(s), respectively. Assuming a QCD production model by Berger [2], an A^1 nuclear target production dependence, and a $B^0 - \overline{B^0}$ mixing probability of 10%, they obtained a cross section of [20]

$$\sigma_{B\overline{B}} = (3.6 \pm 0.4 \pm 1.1) \text{ nb/nucleon},$$

where the first uncertainty is statistical and the second is systematic.

The apparent discrepancy between the WA78 and NA10 cross-section measurements is not due to the data, but to the model used to calculate the acceptance of muons from $B\overline{B}$ decays. WA78 has, in fact, used their data with the same model and assumptions as NA10 and found a cross-section value of about 19 nb which is consistent with the NA10 value [20]. It should also be noted that in the WA78 model itself the cross-section can increase by a factor of two for reasonable variations in the assumed b-hadron x_F distribution and mixing parameters [20].

E653 is an open-geometry hybrid emulsion experiment in which the primary interaction point and short-lived decay vertices were observed [21]. The emulsion was followed by 18 planes of silicon-microstrips for detection of longer-lived decay vertices. The rest of the apparatus included a charged-particle spectrometer, a liquid-argon calorimeter, and a muon

spectrometer. This experiment differs from the previously mentioned fixed-target experiments in that the decay vertices were reconstructed and that charged particles other than muons also had their momenta analyzed. Data were taken during the 1987 Fermilab fixed-target run with a 600 *GeV/c* incident pion beam. 6320 events containing a muon having transverse momentum greater than 1.5 *GeV/c* were selected for scanning in the emulsion. In 353 of these events, the muon was found to be inconsistent with coming from the primary vertex. These events were then analyzed using information from the full spectrometer. Nine beauty pairs with at least one decay in the emulsion target have been found; all have at least three reconstructed decay vertices. The experiment reported a preliminary cross-section measurement from these events of [22]:

$$\sigma_{b\bar{b}} = (33 \pm 11 \pm 7) \text{ nb/nucleon},$$

in agreement with QCD predictions [2].

1.3 The E672 experiment

E672 is a Fermilab fixed-target experiment designed to study hadronic processes that result in final-state muons. E672 shared the Meson-West beamline with experiment E706, an experiment studying direct-photon production. All detector signals were shared between the two experiments. The combined apparatus employed an open geometry configuration (all charged particles had their momenta analyzed), with a muon acceptance in the forward region only. With its dimuon trigger, E672 could search for Bs by their decay into J/ψs which subsequently decays into muons, and also via muons from semileptonic decays. This thesis presents a determination of the beauty hadroproduction cross-section using the J/ψ modes.

CHAPTER 2

EXPERIMENTAL APPARATUS

Fermilab experiments E672 and E706 were in an unique situation in that they shared the same beamline and experimental hall. Detector signals were shared as well. E672's physics interest was the study of hadronic processes which result in muons in the final state: specifically, Drell-Yan and heavy quark (charmonium in particular) production [23]. E706, on the other hand, was interested in direct-photon physics [24]. The two collaborations' apparatus responsibilities reflected, to a certain extent, their different physics goals. E672's main responsibility was the muon spectrometer, while E706 was responsible for the upstream charged-particle tracking and the calorimetry; however, the E706 upstream spectrometer, especially the silicon-strip detector, was essential to the B-physics analysis of this thesis. The trigger hardware and software responsibilities were shared between the experiments. Data from both experiments were read out simultaneously, with information from all detector elements written on tape when either experiment had a valid trigger.

This chapter describes the elements of the E672/E706 apparatus that were used in the analysis presented in this thesis. The beam Čerenkov counter, the straw-tube chambers, and the calorimetry, although invaluable to the experiment as a whole, will not be described as they were not used in this analysis.

2.1 Layout of the combined E672/E706 apparatus

A schematic of the combined E672/E706 apparatus is shown in Fig. 2.1 (the beam travels from left to right in this figure). The equipment begins with a beam Čerenkov counter (not shown), followed by a hadron shield and scintillation-counter "Veto Wall" array.

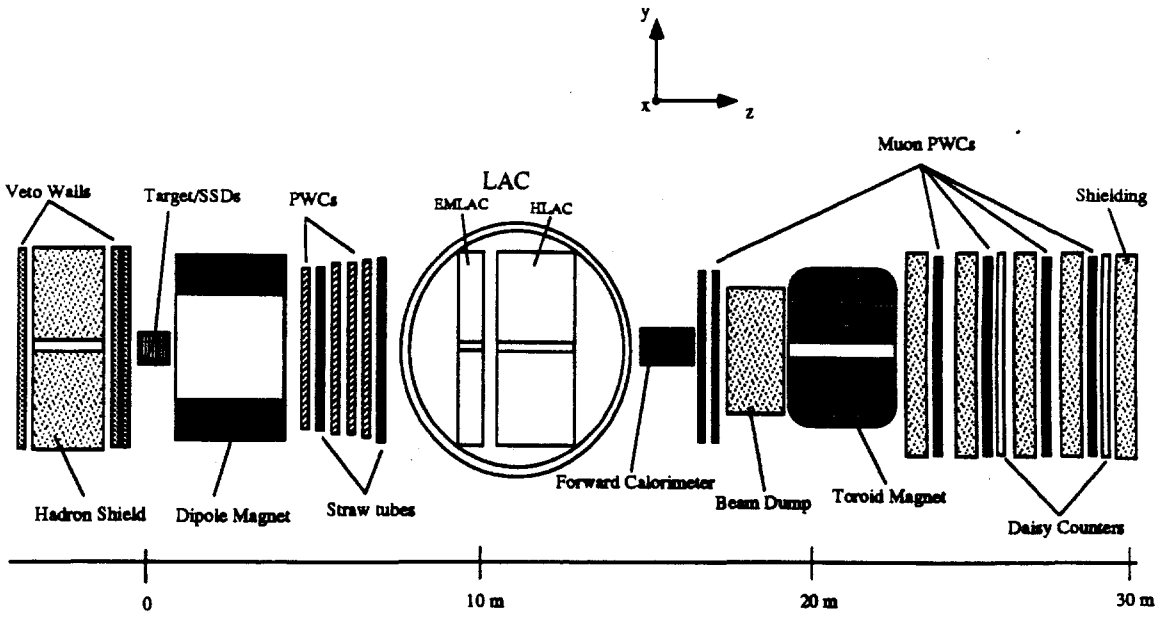

Figure 2.1. The combined E672/E706 apparatus.

The upstream charged-particle spectrometer follows. The spectrometer consists of a silicon-strip detector (SSD), a dipole analysis magnet, and a PWC/straw-tube array. Next comes the calorimetry, consisting of a liquid-argon calorimeter (LAC) with both electromagnetic and hadronic sections, and a "forward" steel/scintillator calorimeter. The muon spectrometer follows the calorimeters. It consists of a set of upstream muon PWCs, a beam dump and toroid analysis magnet, and downstream muon chambers separated by iron/concrete shielding. Two "Daisy Counter" scintillation hodoscopes are positioned between the downstream muon PWCs and shielding, as shown. The positive z-axis is chosen to be along the beam direction, with the positive x-axis to the right when looking downstream. The positive y-axis is vertically upwards, thus forming a right-handed orthogonal coordinate system. The entire apparatus (excluding the beamline devices) extends approximately 35 meters in length.

2.2 The Meson-West beamline

The E672/E706 apparatus was located at the downstream end of the Meson-West (MW) beamline. This beamline was designed to transport secondary beams of both positive and negative charge, with momenta ranging from 25 *GeV/c* to 1000 *GeV/c*. Secondary beams were produced by extracting 800 *GeV/c* protons from the Tevatron and colliding them with a one-interaction-length aluminum target. The Tevatron operated on a 57.2 second long cyclic basis, with the actual spill of beam to the experimental areas lasting 23 s. The protons in the primary beam occurred in very narrow time intervals known as "buckets". Each bucket was about 1 ns wide, and they were spaced 19.7 ns apart. The probability of a bucket being occupied by a single proton was 10%, and the double occupancy probability was 2%. An incident primary flux of 10^{12} protons/spill impinging on the aluminum production target produced a usable secondary pion beam of approximately 30 million pions/spill [25].

During the 1990 fixed-target physics run, E672/E706 ran with a 530 *GeV/c* negative pion beam. The beam momentum spread was approximately 10%, and the kaon contamination was estimated to be 3% using the beam Čerenkov counter [25]. During the optimal data taking part of this run, a secondary pion beam of 150 million particles/spill was achieved from a primary intensity of 5×10^{12} protons/spill. During the 1991-92 fixed target run, data were also recorded with 800 *GeV/c* and 530 *GeV/c* proton beams. This thesis, however, uses only the pion data taken in 1990.

2.3 Beam-halo shield and veto walls

The secondary beam to the experiment was accompanied by a halo of muons from pion decays and hadrons from beamline interactions. "Spoiler" magnets were employed in the

upstream beamline in order to sweep these particles away from the beam. A large iron hadron shield located in the most upstream portion of the experimental hall attenuated any remaining hadrons. Muons, however, passed easily through this shield. These muons are detected in three "veto-wall" scintillation detectors, one was placed just upstream of the hadron shield, and the other two were located just downstream of it (see Fig. 2.1).

The upstream veto wall (VW3) consisted of 18 scintillation counters and covered a total area of approximately 3 m x 3 m. The downstream veto walls (VW1 and VW2) each consisted of thirty-two 50 cm x 50 cm scintillation counters. These two walls had a 10 cm overlap in the x-y plane in order to cover gaps between scintillators. All of the walls had openings in the central region to allow beam particles to pass without generating a signal. Coincidences between the walls, VW = (VW1 + VW2)*VW3, were used to veto an event at the pre-trigger level. The veto system was important for both experiments in that the E672 dimuon trigger could be fooled by a halo particle, while the E706 trigger could be set of by a bremsstrahlung photon produced by a high-energy halo-muon.

2.4 The upstream spectrometer

The upstream charged-particle spectrometer consisted of a set of silicon-strip detectors (SSDs), a dipole analysis magnet, a set of proportional wire chambers (PWCs), and two straw-tube chambers (the straw-tubes were not used in this analysis and will not be described here). This tracking system was used to determine the beam-particle trajectory, the interaction and secondary (if present) vertices, and the momenta of the charged tracks accepted by the spectrometer.

2.4.1 The silicon-strip detector system

The silicon-strip detector system consisted of eight modules of silicon wafers, each containing one vertically and one horizontally oriented micro-strip wafer. The strips are essentially an array of PIN diodes. Charged particles passing through this array create electron-hole pairs that are, under the influence of a reverse bias voltage, collected on electrodes. This signal is amplified by a charge sensitive pre-amplifier, then fed to an amplifier-discriminator unit for readout. [26, 27].

The configuration of the SSD system is shown in Fig. 2.2. There are three 3 cm x 3 cm x-y modules placed upstream of the target for beam tracking purposes (the most upstream module is not shown in the figure). These modules are referred to as the "beam" SSDs. Following the target are five 5 cm x 5 cm x-y modules that determine event vertices and charged particle trajectories; these are the "vertex" SSDs. The modules are instrumented in such a way as to reflect the acceptance of the upstream spectrometer determined by the PWC coverage. All of the modules have 50 micron pitch, except for the most upstream vertex SSD module which has 25 micron pitch strips in its central region.

The target used in the 1990 run consisted of beryllium and copper -- different materials were used in order to study atomic number dependence. At the upstream end of the target are two copper disks of 0.08 cm thickness separated by a 0.26 cm air gap. Downstream of the second piece of copper is a 0.55 cm gap, followed by a 3.71 cm thick Beryllium cylinder, a 1.02 cm gap, and another Beryllium cylinder of thickness 1.12 cm. This target was designed for varying physics studies, and so did not have an optimal configuration for *B*-physics.

Silicon-Strip Detector and Target Configuration

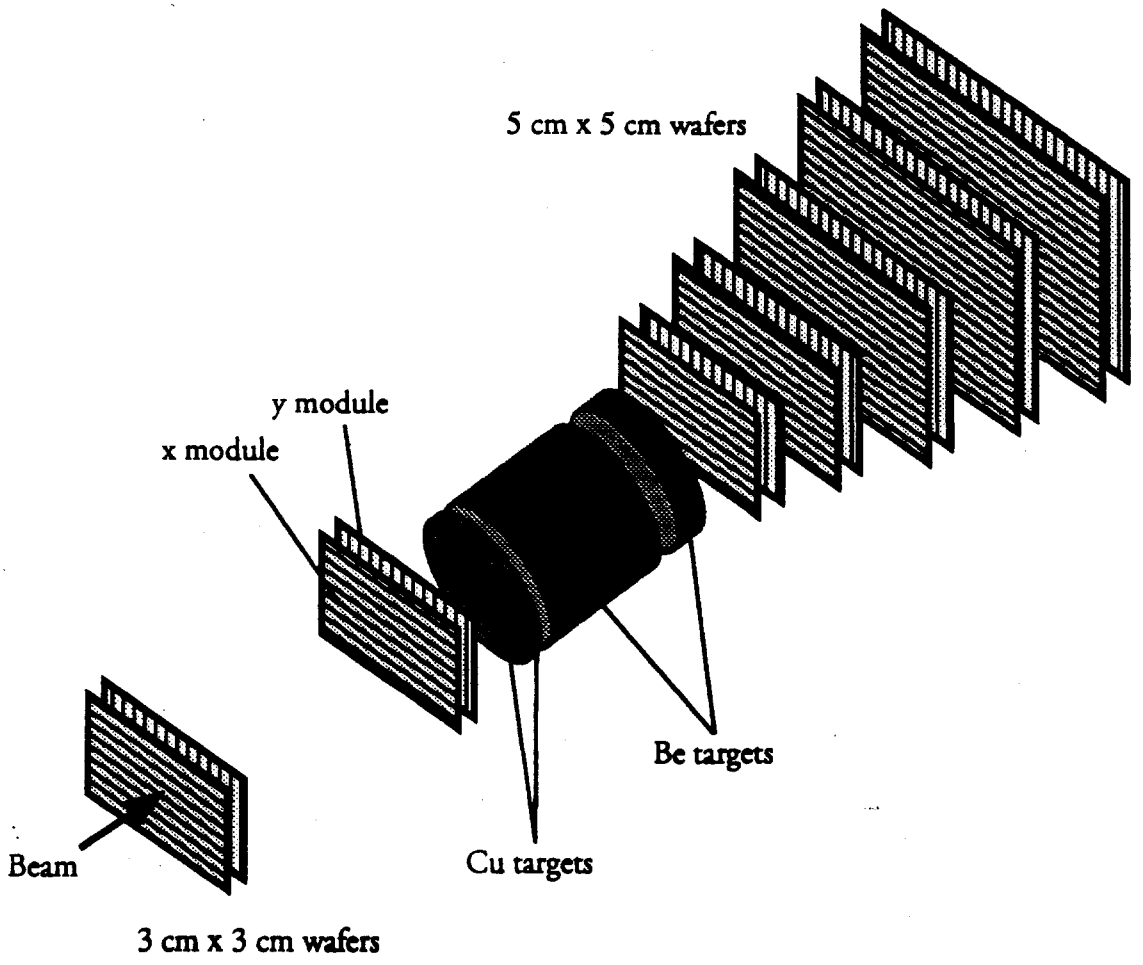

Figure 2.2. Silicon strip detector (SSD) and target configuration (The first beam module is not shown). All modules have 50 micron pitch, except the first module downstream of the target, which has 25 micron pitch strips in its central region.

Figure 2.3 demonstrates the spatial resolution obtained using the SSD system during the 1990 run. It shows the distribution of the charged-track impact parameter with respect to the reconstructed primary vertex. The width of this distribution is consistent with the expected detector resolution of 10 microns.

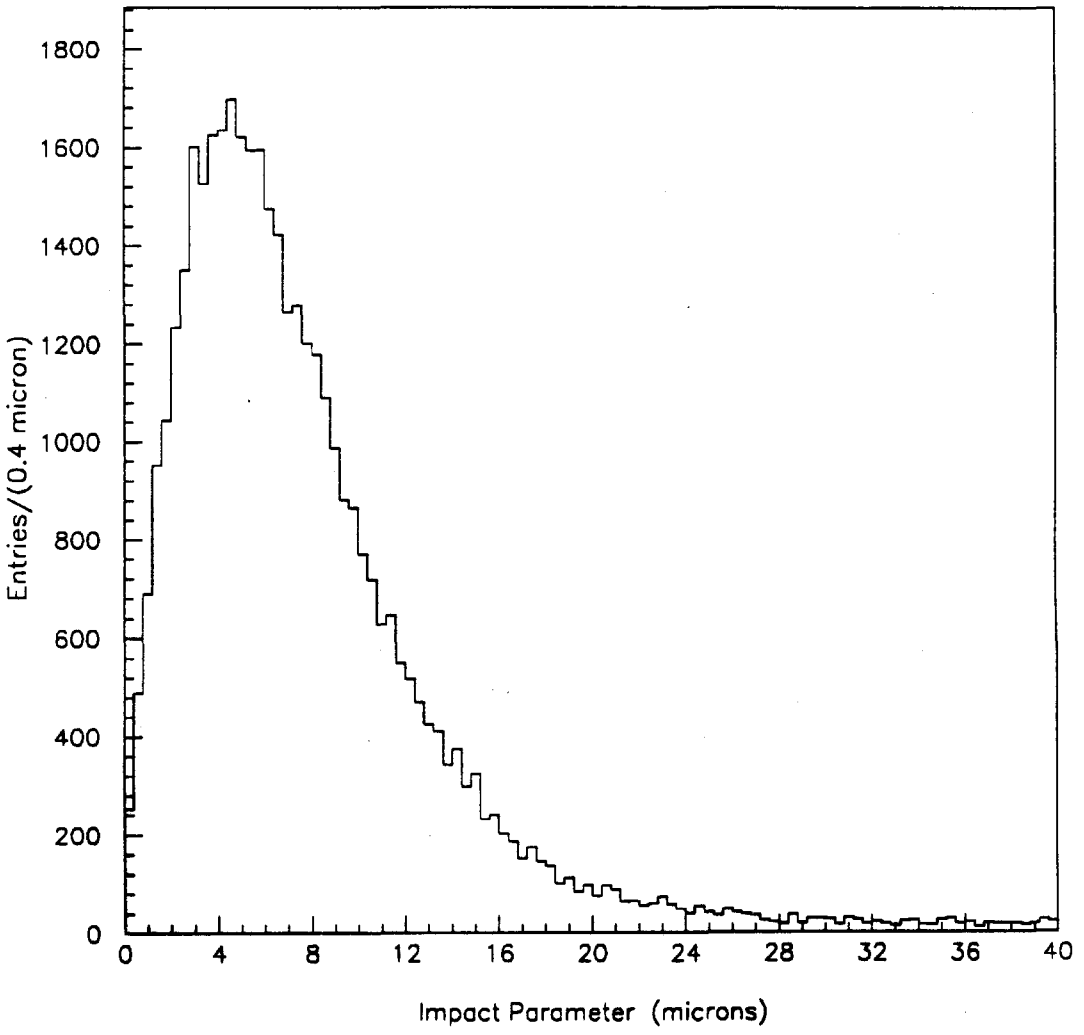

Figure 2.3. Impact parameter of charged tracks with respect to primary vertex.

2.4.2 The dipole analysis magnet

In order to measure the momentum of charged particles a dipole analysis (designated as MW9AN) magnet was located between the SSDs and PWCs (see Fig. 2.1). This dipole provided a p_T kick in the x-direction; the momentum of a track is found by a measurement of its trajectory before and after this kick. In order to reduce the effects of multiple scattering, a polyethylene bag filled with Helium gas was installed in the magnet's central region.

The magnet had an effective length of 328 cm along the beam direction. Twenty cm mirror plates were installed on both ends of the magnet to reduce the fringe field, making a nearly uniform field in the vertical (y) direction. The magnetic field was mapped using the ZIPTRACK system [28], and details of mapping can be found in Ref. [29]. The dipole was normally operated at a current of 1050 A, producing a vertical magnetic field of strength 6.24 kG, which corresponds to a p_T kick of 450 *MeV/c*.

The geometrical acceptance of the dipole magnet was defined by rectangular holes in the mirror plates. The size of the upstream mirror-plate hole was 35.56 cm x 25.4 cm, and that of the downstream hole was 127 cm x 91.4 cm.

2.4.3 The proportional wire chambers

The proportional wire chambers and straw-tube detectors constitute the downstream end of the upstream spectrometer. Four PWC chambers, each with four anode signal planes (x, y, u, v) were located downstream of the dipole magnet. Two straw-tube chambers were located between the PWCs as shown in Fig. 2.1; these chambers were not used in this analysis and will not be described here. The PWC u-planes were tilted at an angle of 37° to the vertical, and the v-planes were tilted at an angle of -53° to the vertical.

The anode signal planes were made of 0.8 mil-diameter gold-plated tungsten wires of spaced at 2.54 mm. For each anode plane, there is a pair of cathodes planes, one on either side of the anode, separated by a distance of 5.74 mm. The cathode planes were constructed of graphite-coated, 1.0 mil thick Mylar sheets, segmented into three rectangular regions extending concentrically from the center of the planes. This segmentation enabled the high voltage to be set independently in the three regions, thereby allowing reduced sensitivity in the beam-region by application of lower voltage to the inner-most segment without affecting sensitivity in the outer segments.

The four PWCs were sized to maintain a relatively constant angular acceptance. The most upstream chamber was 1.63 m wide x 1.22 m high, the second and third were 2.03 m square, and the fourth chamber was 2.44 m square. The PWC system had 13,440 active channels that were read-out by the same Nanometrics system as the SSDs [26]. The PWC system is described in detail elsewhere [29].

2.5 The E672 muon spectrometer

The E672 muon spectrometer is shown in Fig. 2.4. It consists of two upstream muon proportional wire chambers, a beam dump made of steel and tungsten imbedded in concrete, and a toroid analysis magnet. Four more muon PWCs, separated by iron and concrete shielding, are located downstream of the toroid. Two trigger hodoscope planes ("daisy counters"), each made of sixteen sector-shaped scintillation counters, are also located in this region as shown in Fig. 2.4. All particles which make it through the material of the upstream apparatus and the muon system shielding are assumed to be muons. The muon spectrometer provides muon identification and momentum measurement on both the trigger and off-line levels.

The E672 muon spectrometer

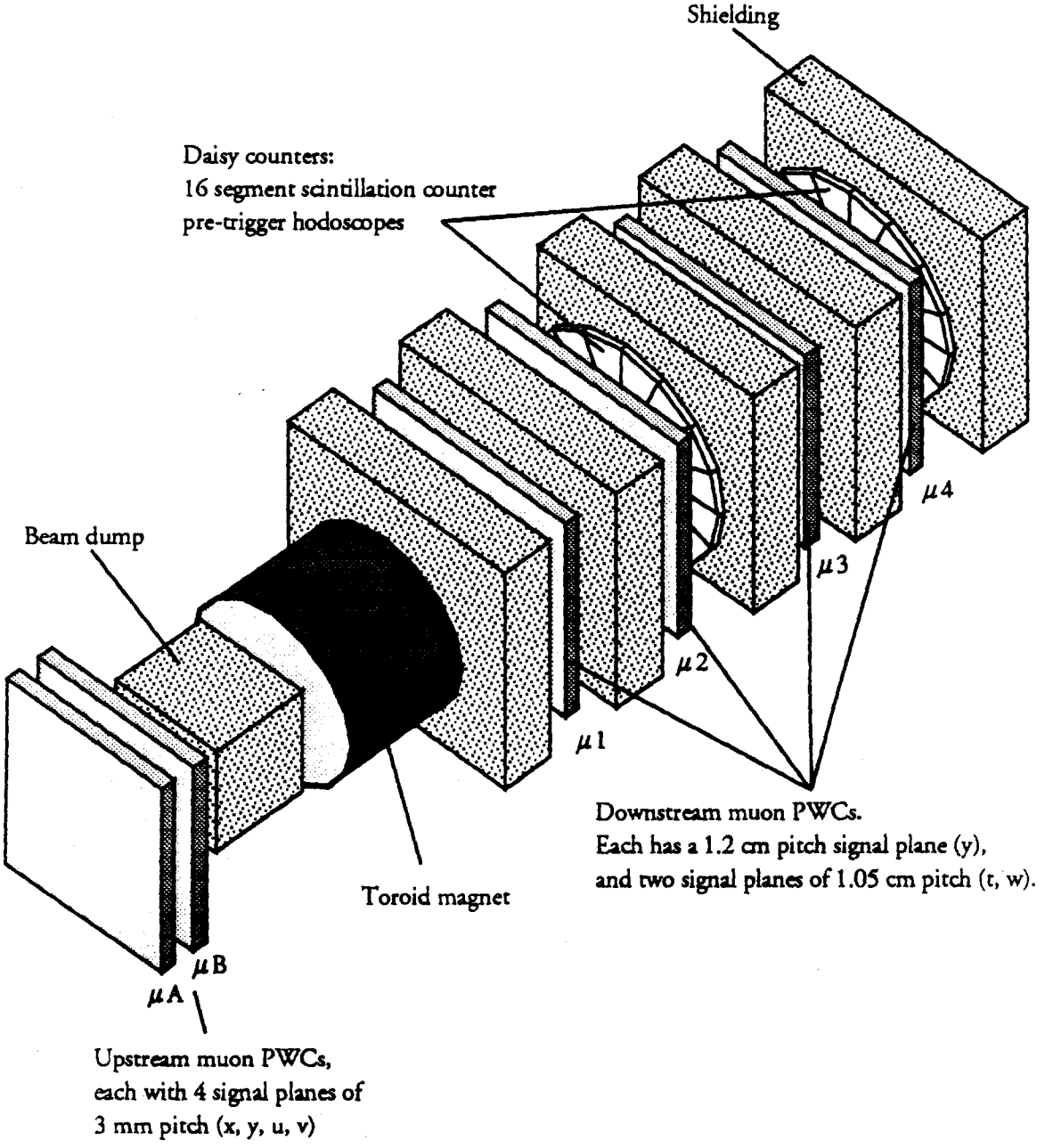

Figure 2.4. The E672 muon spectrometer.

2.5.1 The upstream muon PWCs

The E672 muon spectrometer begins with the μA and μB PWCs, each consisting of four anode signal planes (x, y, u, v). The u-planes are tilted at an angle of 10° to the vertical, and the v-planes are tilted at an angle of -10° to the vertical. The anode planes are composed of 1.0 mil diameter gold-plated tungsten wires with a pitch of 3.05 mm. Beam deadeners (5 cm diameter disks of 3 mil thick Kapton) were attached to the center of each anode plane. There are a total of 1520 channels for each chamber. Cathode planes, made of 1650 Cu/Be wires, were placed on each side of the anode planes. For electric field stability, two wire ground planes (1725 wires each) were placed in each chamber, one before the first cathode and one after the last. Both cathode and ground planes were made of 3.5 mil diameter Cu/Be wires having a 1.02 mm pitch [30].

Anode signals were amplified/discriminated by 16-channel Nanometrics N-277C cards [31], and sent to a LeCroy PCOS III encoding system over flat Spectrastrip cables. The gas used for these chambers was a mixture of 76% argon, 15% isobutane, 8.9% methylal, and 0.1% Freon. This mixture was based on the performance of similar chambers in previous experiments [32]. Figure 2.5 shows efficiency and noise rate, as a function of high-voltage for one of the planes. The chambers were typically operated at a high-voltage of approximately 4.5 kV. The orientation, number of channels, and active area of the upstream muon-chamber planes are summarized in Table 2.1

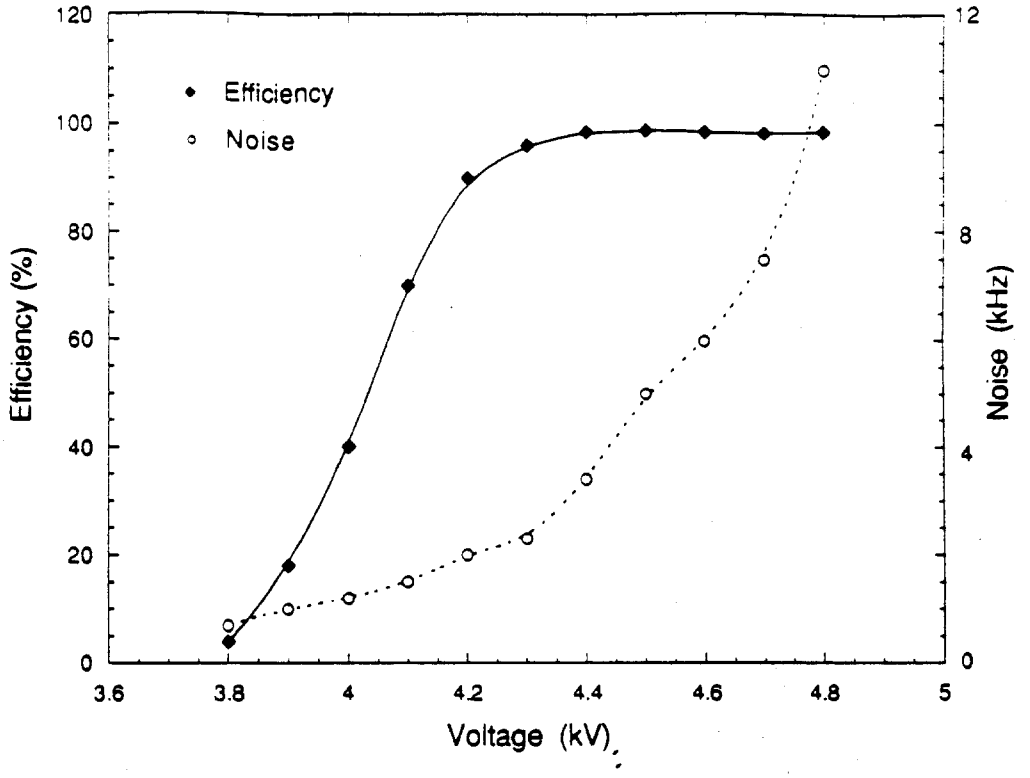

Figure 2.5 Typical high voltage curve (efficiency and noise) for upstream muon chamber planes.

Table 2.1. Upstream muon chamber specifications

chamber	plane	angle from vertical (degrees)	number of wires	active area (meters^2)
μA	x	90	256	1.7 x 0.8
μA	y	0	560	1.7 x 1.7
μA	u	10	352	1.7 x 1.1
μA	v	-10	352	1.7 x 1.1
μB	x	90	544	1.7 x 1.7
μB	y	0	544	1.7 x 1.7
μB	u	10	448	1.7 x 1.3
μB	v	-10	448	1.7 x 1.3

2.5.2 The toroid magnet

In order to determine muon momentum, a water-cooled, polarized-steel toroid magnet was located between the upstream and downstream muon chambers. The toroid was 2.44 m long, had an outer radius of 1.35 m, and weighed approximately 125 tons. The inner radius of the toroid was 16.8 cm at the upstream end and 19.7 cm at the downstream end, corresponding to a taper angle of about 11 milliradians. The toroid field was in the axial direction, and had no measurable dependence on azimuthal angle. The field strength did, however, become weaker with increasing radius. At a nominal operating current of 1700 A, the field was calculated to be 2.24 T at the inner radius and 1.74 T at the outside, which correspond to momentum kicks, in the radial direction, of 1.64 *GeV/c* and 1.27 *GeV/c*, respectively. Details of the field measurement can be found elsewhere [33]. The muon momentum measurement that the toroid provided was used on the trigger level, and is compared (off-line) to momentum measurements in the upstream spectrometer to help in linking tracks between the downstream and upstream systems.

2.5.3 The pretrigger hodoscopes

Two "daisy counter" scintillation hodoscopes (DC1, and DC2) were located in the downstream muon chamber array, as shown in Fig. 2.4. Coincidences between these hodoscopes provided a fast trigger on the presence of tracks in the muon chambers. The hodoscopes were both 1.5 m in radius, with active areas matched to the active area of the muon PWCs. Each hodoscope consisted of 16 triangular scintillator segments placed in a circular "petal" pattern, and were thus given the nickname "daisy counter". Each hodoscope was divided into four quadrants, and each had four triangular-shaped segments of PS-10

plastic scintillator encased in aluminum sheets. Light from each segment was collected by a BBQ doped waveshifting bar and transmitted, at a wavelength of 410 nm, to RCA 8575 photomultiplier tubes encased in μ-metal shields. Figure 2.6 shows a schematic diagram of one of the hodoscopes.

The photomultipliers were operated at a high voltage near 2.1 kV. At this voltage the counters were at least 90% efficient and had a noise rate of about 300 Hz per tube. Signals from the tubes were sent to a CAMAC module (described in the next chapter) which determined the muon multiplicity for a pretrigger signal.

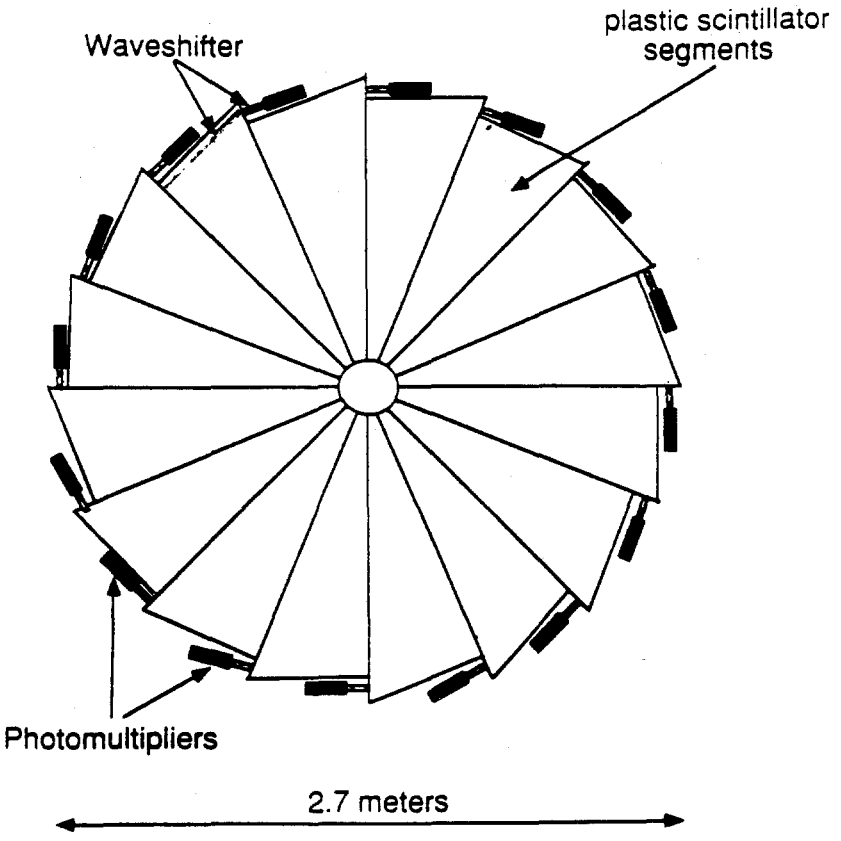

Figure 2.6. Schematic diagram of pretrigger hodoscope.

2.5.4 The downstream muon PWCs

The heart of the E672 muon spectrometer was a set of four muon PWC chambers (μ1, μ2, μ3, and μ4). These chambers provided the downstream muon trajectory for triggering purposes and off-line reconstruction. Each chamber consisted of two cathode planes (u, v), and one anode plane (w). The cathode planes were made of copper clad G-10 epoxy-fiberglass sheets of 1.6 mm thickness. The inside surface of a cathode plane is, effectively, a large printed circuit board, etched to give a pattern of 10.5 mm pitch parallel strips. The cathode strips were orientated at $\pm 45°$ to the vertical. The anode planes were traditional multiwire planes made of 25 micron diameter gold-plated tungsten wires oriented in the horizontal direction. The anode plane of the middle PWC (μ2) consisted of 669 wires of 0.4 cm spacing. Groups of three adjacent wires were connected to individual amplifier channels, giving an effective pitch of 1.2 cm and 223 channels. The anode planes of the other three chambers consisted of 446 wires with 0.6 cm spacing. Pairs of adjacent wires were connected to individual amplifier channels, giving them the same effective pitch and number of channels as μ2. The specifications for the downstream muon chambers are shown in Table 2.2.

Signals from the chambers were read out using three-stage, 16-channel amplifier/ discriminator cards designed and built at Indiana University [32]. ECL-level signals were sent from the discriminators to a LeCroy PCOS III encoding system by flat Spectrastrip cables. This is the same readout system used for the upstream muon chambers. Further details of the construction and operation of these chambers can be found in Ref. [33].

Table 2.2. Downstream muon chamber specifications

Inner radius	μ1	15 cm
	μ2	15 cm
	μ3	18 cm
	μ4	20 cm
Outer radius	all	1.35 m
Channels	u, v	255
	w	223
Effective pitch	u, v	10.5 mm
	w	12.0 mm
Anode-cathode gap	all	9.5 mm

CHAPTER 3

TRIGGER LOGIC AND DATA ACQUISITION

E672 and E706, in addition to sharing detector signals, also share triggers. E672 triggers on events with high-mass dimuons in the final state, while E706 has a variety of LAC based triggers [34]. The dimuon trigger consists of two levels. The level-one trigger (or pretrigger) requires hits in the "daisy counter" muon hodoscopes consistent with two or more tracks. The second level trigger is based on an invariant-mass calculation done by a dimuon trigger processor (DTP) which uses muon chamber information. The readout computers are interrupted when either experiment has a trigger, and signals from the entire apparatus are written to tape.

3.1 Muon system readout

Signals from the "daisy counter" hodoscopes (32 phototubes) are transmitted to a 32 channel CAMAC pretrigger module by RG58-C coaxial cable. The module discriminates the phototube signals and sets a latch for each channel that exceeded the threshold voltage during an externally set gate. The module then calculates the track multiplicity from the latched hit pattern and sets out a NIM level if this multiplicity is above an adjustable threshold (0-16) [35].

The muon chamber signals are read out using the LeCroy PCOS III system (Proportional Chamber Operating System) [36]. Signals from the chambers are sent to LeCroy 2731 latch modules. These latch modules reside in CAMAC crates; each crate can hold 23 latches and one controller. The brain of the system is the LeCroy 2738 crate controller module which queries each 2731 latch module in its crate and stores the addresses of active channels in an

internal buffer for transfer to the data acquisition (DA) system and trigger logic circuits. The system is used in "non-clusterized' mode, so each active channel produces a data word with 3 plane identifier bits and 8 wire address bits. Communication with the DA system (described later) is done through a LeCroy 4299 DataBus interface. The controller also has an ECL port which transfers data at a rate of 10 times that of CAMAC to the trigger logic circuits.

3.2 The dimuon trigger

The dimuon trigger begins with a coincidence of three signals signifying, respectively, the presence of a beam particle, an interaction, and the DA computers and logic modules not being busy. This signal is called START PRETRIGGER and is sent to the pretrigger module described in the previous section. This module calculates the muon track multiplicity using the "daisy counter" hits, and if it is greater or equal to two tracks a NIM signal is generated. This signal, in coincidence with a signal called $\overline{VW}$ is used to start the dimuon trigger processor (DTP). $\overline{VW}$ signifies that no particles were detected in the muon halo veto walls (it is the "NOT" of the VW signal described in the previous chapter). The DTP uses the muon chamber information to calculate the approximate invariant mass of the muons, and if this is above an adjustable value, a valid E672 trigger signal is sent to the data acquisition system.

3.2.1 The dimuon trigger processor

The dimuon trigger processor consists of 8 double-width CAMAC modules. Encoded data from the muon chamber PCOS system is sent to the trigger processor by the LeCroy 2738 crate controller through the fast ECL port. The encoding time for an average two

muon event is about 6 μs. Data from the first and last downstream muon chambers (μ1, and μ4) is sent to the first two modules of the DTP, which are called the POINT modules. A schematic diagram of the DTP is shown in Figure 3.1.

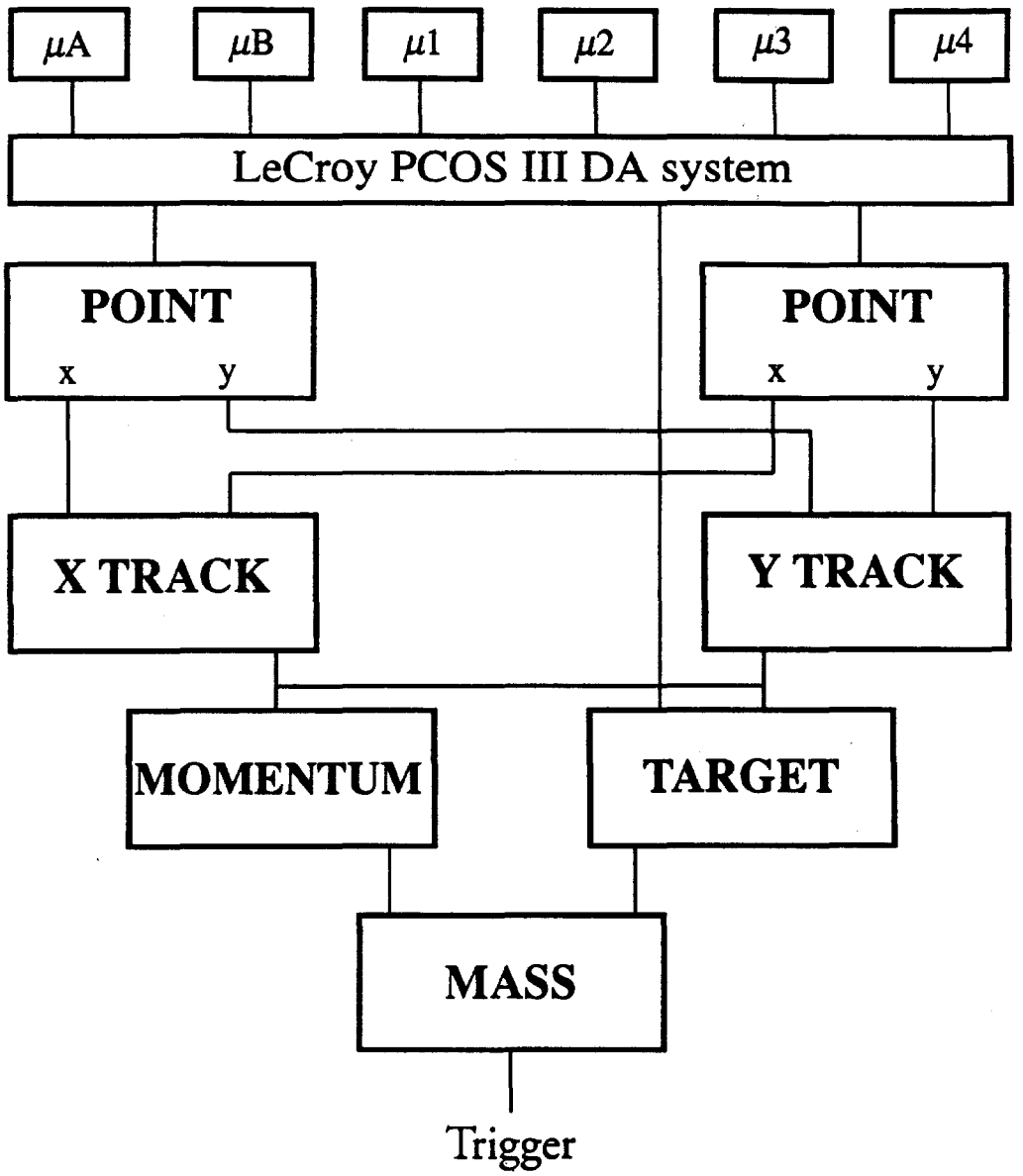

Figure 3.1. Schematic diagram of dimuon trigger processor (DTP)

The POINT modules calculate a set of space points, in parallel, by first clustering the hot chamber wires in groups of three wires maximum. Cluster intersections in the u, v planes are then compared to v clusters to look for matches, and a set of space points are found. This set of points is then checked against a look-up table stored in Programmable Read Only Memories (PROMs) to ensure that they are in the fiducial volume of the chamber. The list of valid points is stored in Random Access Memories (RAMs), and sent to the TRACK modules.

The two TRACK modules also receive the wire hit information from the remaining two downstream chambers, and a set of x and y view tracks are found (again in parallel). This track list is transferred to the TARGET and MOMENTUM modules. The TARGET module also reads upstream muon chamber (μA, and μB) data from the corresponding PCOS ECL ports. This module projects the downstream muon system tracks (found in the TRACK module) to the center of the toroid (see Fig. 3.2). It connects a straight line between the point at the toroid center and the center of the target for each track, and looks for hits in the upstream muon chambers consistent with these connections. The list of tracks having corresponding hits in at least 3 out of 4 planes in both chambers is sent to the MASS module.

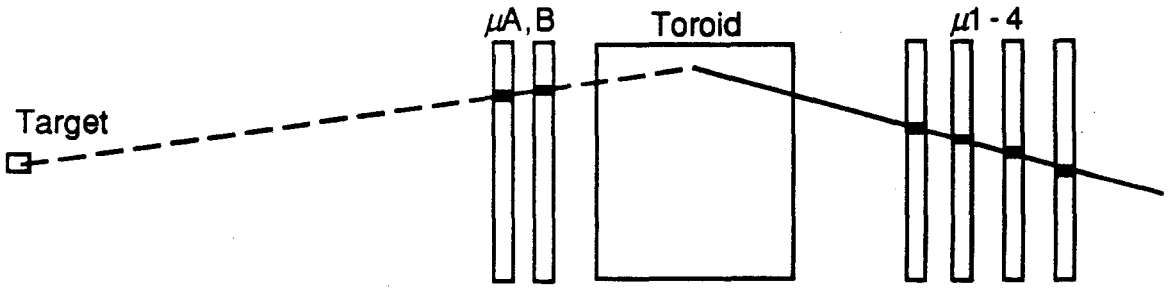

Figure 3.2. Target module algorithm (apparatus not to scale): solid line is downstream chamber track; dashed line is connection between this track's intersection point at the toroid center with the center of the target. The target module looks for hits in upstream muon chambers consistent with this connection.

In parallel with the TARGET module calculations, the MOMENTUM module calculates the momentum of the tracks by their apparent bend at the center of the toroid (assuming the tracks originated at the center of the target). The MASS module takes this information and calculates the approximate invariant mass for valid track pairs. A success signal is generated if the mass of at least one of these pairs is above a selectable threshold. For the 1990 run this threshold was varied between 0.5 GeV/c^2 and 1.0 GeV/c^2 in such a way as to keep a 25% ratio of dimuon to total E672/E706 triggers. The average decision time for the DTP was about 6 μs, excluding the PCOS encoding time. A detailed description of the dimuon trigger processor can be found elsewhere [37].

3.3 Data acquisition

The E672/E706 data acquisition system (DA) is divided into four main parts. Three of these are CAMAC based PDP-11 systems, while the fourth is a FASTBUS system. The LAC and strawtube information is read out by the FASTBUS system, and is controlled by a PDP-11 named MX. A PDP-11 named MU handles the muon system information. PDP-11s named NEU, and ROCH, read out the upstream spectrometer, and forward calorimeter, respectively. Data from all the sources was concatenated using a DEC MicroVAX II running Fermilab VAXONLINE software [38]. Figure 3.3 shows a schematic of the combined apparatus data acquisition system.

The MU PDP-11 communicates with the muon system CAMAC through a Jorway 411 interface which reads the CAMAC crates on a serial CAMAC highway. Muon Chamber information is controlled by a LeCroy 4299 PCOS III DataBus Interface. The pretrigger and DTP modules, as well as various ADCs, TDCs, scalers, and other devices are also read out through the highway. The PDP-11s are connected to the VAX through Communication

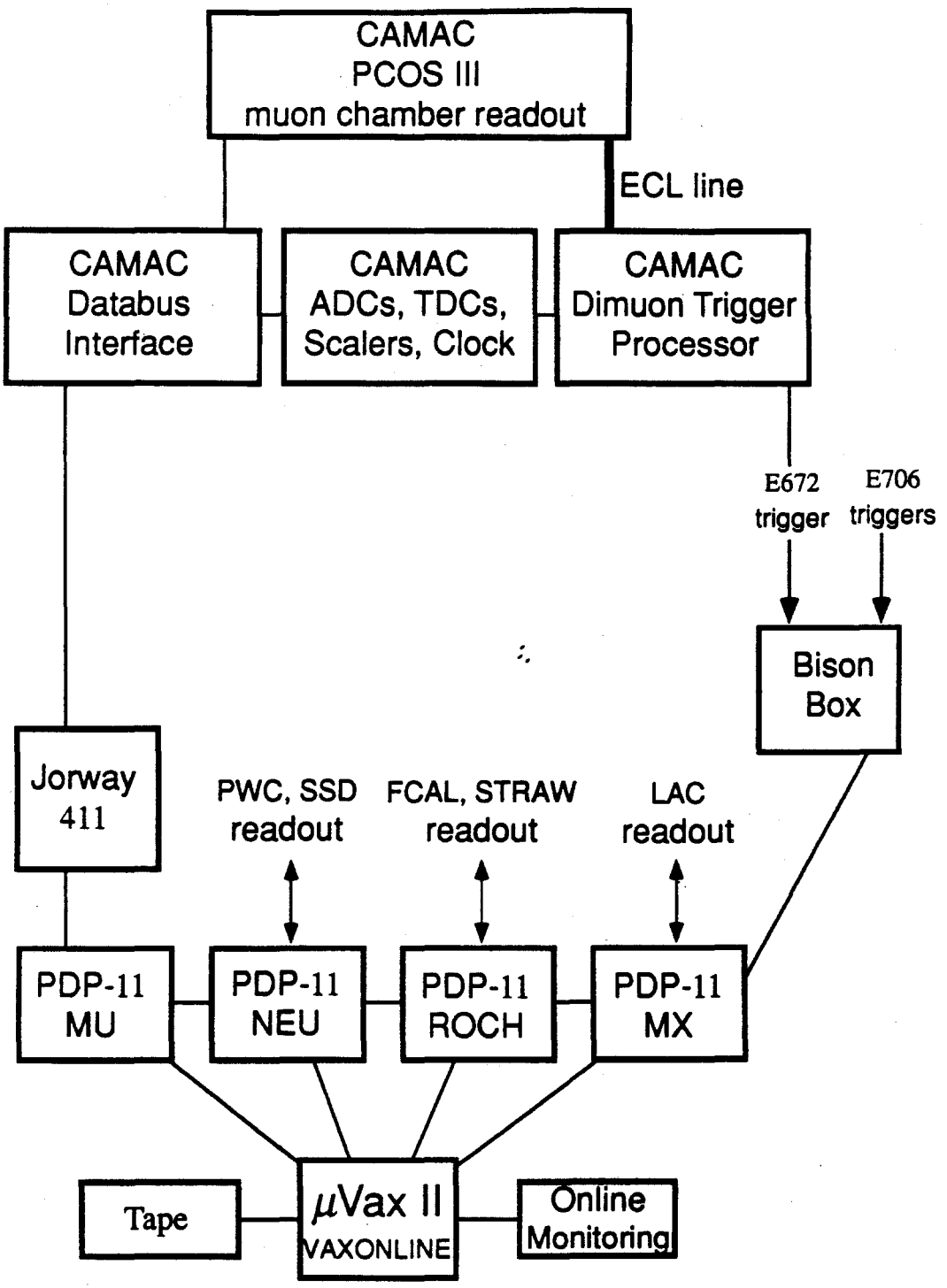

Figure 3.3. Schematic of the combined apparatus data acquisition system.

Device (CD) links [39]. Interrupts for the PDP-11s are controlled by the use of a device developed at Fermilab called a Bison Box [40]. This device accepts triggers, and begin and end spill interrupts, and sends interrupt signals to the PDP-11s. It has an input register where the devices to be read out can be specified by setting appropriate bits (by use of terminators) on the front panel.

The overall control of the run, tape logging, monitoring, etc. is done on the VAX using the VAXONLINE data acquisition software package [38]. Information from the PDP-11s is transferred to an "event pool" on the VAX, and several processes are run under the VAXONLINE umbrella. During the run, data was written to two 8 mm Exabyte tapes simultaneously.

CHAPTER 4

EVENT SELECTION AND RECONSTRUCTION

As mentioned in previous chapters, the raw data tapes contain all the triggers taken by E672 and E706 with information from the entire apparatus written out. In order to test tracking programs and to get to some select physics quickly, the subset of high-mass dimuons was selected. The first step in the dimuon data reduction was the extraction of E672 triggered events from the original event tapes. This reduced the number of events by a factor of 4. Approximately six million dimuon triggers were taken in 1990. To further reduce the size of the sample, a special stream of data was extracted which only contained information from the charged particle spectrometers of both E706 and E672. This exclusion of the calorimetry information reduced the event size by a factor of 8. A first pass muon reconstruction program was then run on the sample. Events with a least two reconstructed muons from the target region were sent to a program that linked the muons to the upstream spectrometer elements, reconstructed the other charged tracks, and found the event vertices.

4.1 Detector module track finding

4.1.1 Muon chamber track reconstruction

The muon chamber track reconstruction program, written by Jack Martin [41], first looks for clusters (adjacent wire hits) in the separate views (u, v, w) of the downstream muon chambers. The center of a cluster is used as a view hit with a corresponding uncertainty of half the cluster width. Single-view tracks are found by a binary search of all the possible roads containing a minimum number of planes (3 out of 4 possible) with hit clusters within the road. First, the active area of the chamber is divided into four roads as shown in Fig.

4.1, then the roads that contain more than the minimum number of hit planes are similarly divided into four roads. The process is continued until all the valid roads are small enough to contain only one hit cluster per plane. In the simple example demonstrated in Fig. 4.1 (one track plus a spurious noise cluster) only road number 3 of the first four chosen roads contains more than the minimum number (3) of planes hit.

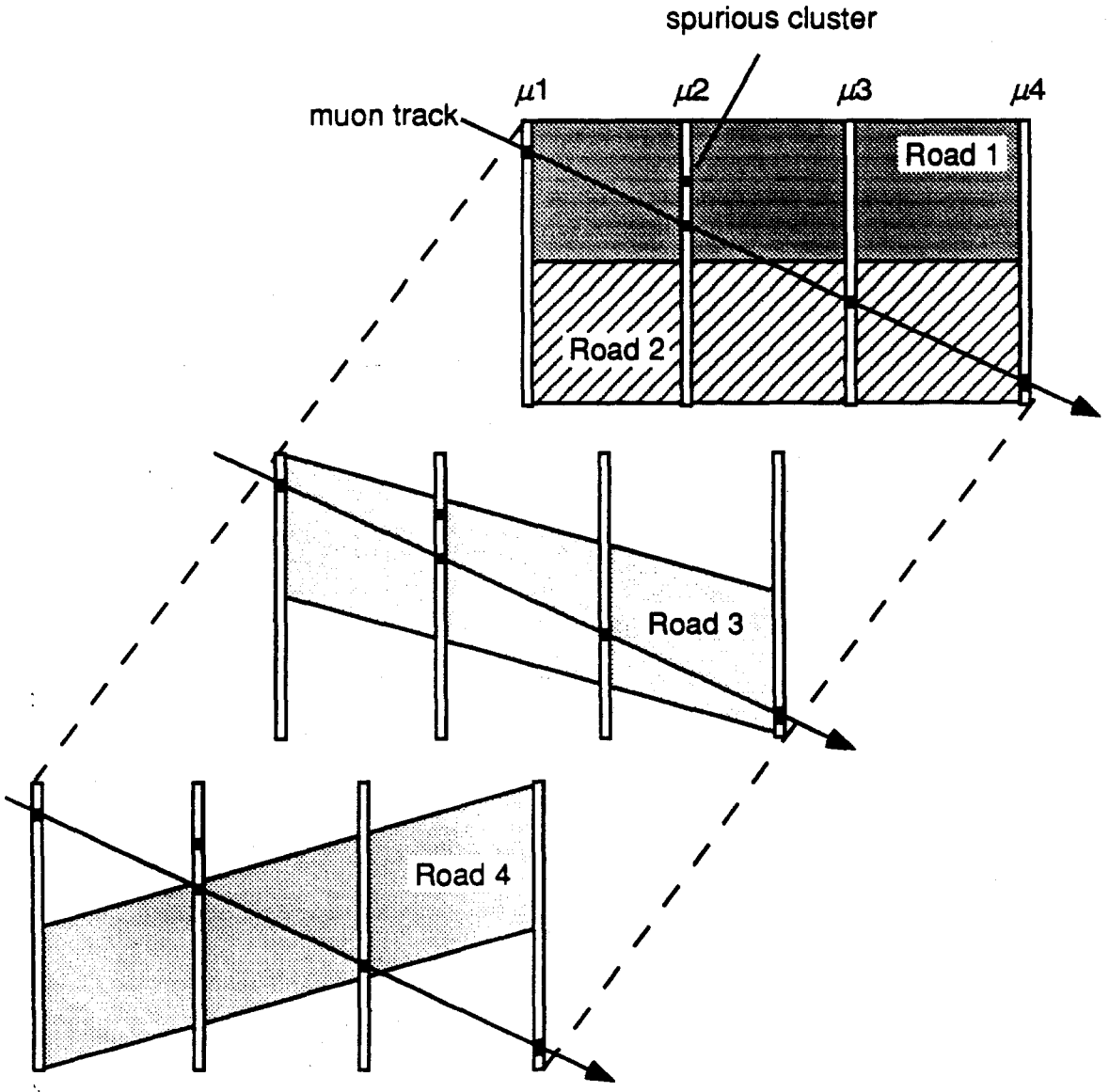

Figure 4.1. Illustration of the first roads chosen in the muon track finding algorithm.

This road is further subdivided into four roads (as shown in Fig. 4.2), since it contains a plane with more than one cluster within the road width. The subdivision yields only one road with more than 3 planes hit within (road 7), and this road need not be subdivided further since the extra plane hit no longer lies within its width.

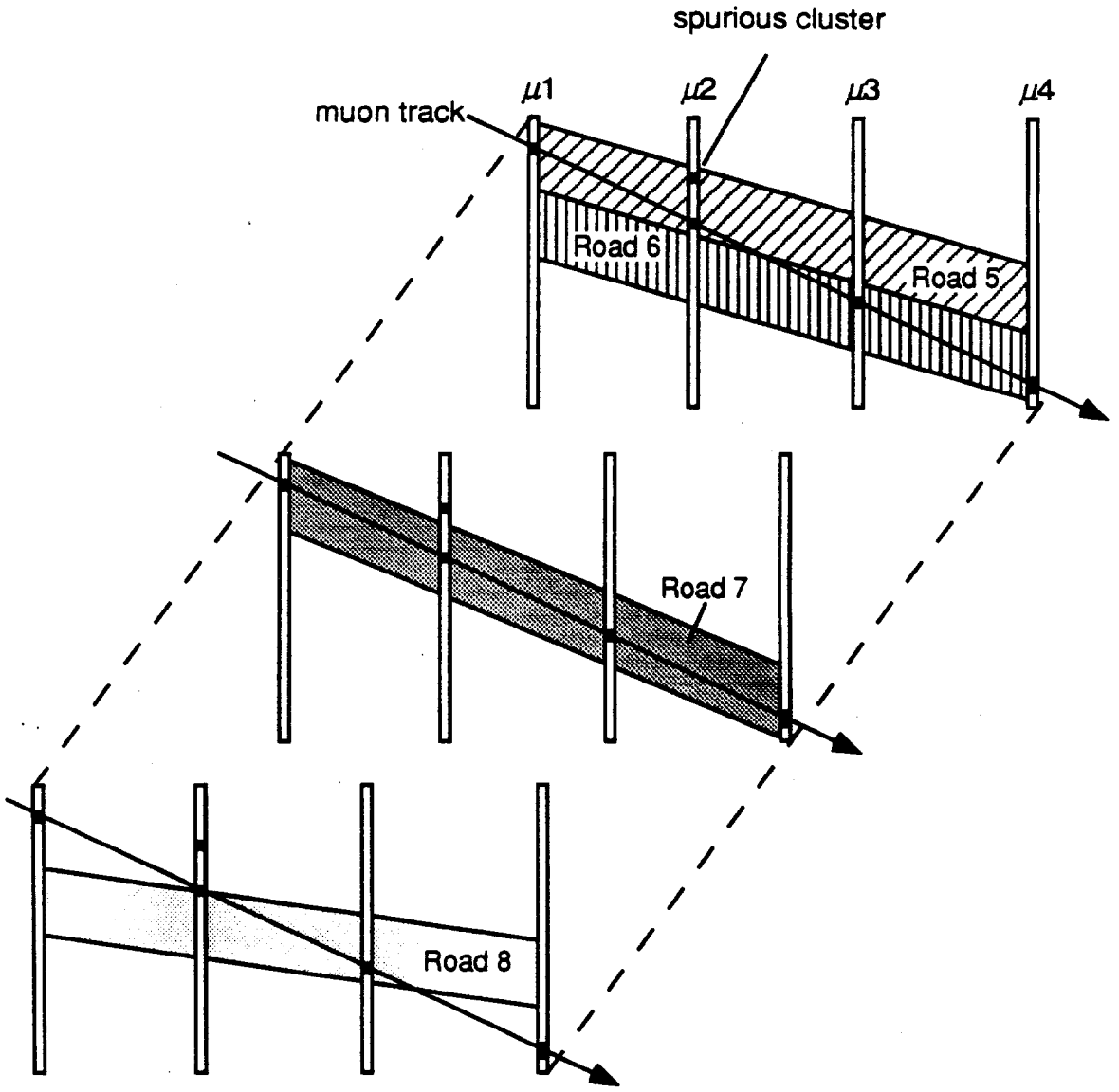

Figure 4.2. Illustration of the second set of roads chosen in the muon track finding algorithm.

The actual muon chamber cluster patterns are, of course, more complicated than this simple example. After the final set of valid roads have been obtained, a straight line fit is done to the clusters within each road to determine the view-track (x, y) slopes and intercepts.

Three dimensional space-tracks are found in a similar binary search of the view-track parameters. Space-roads are constructed and checked to see if any set of view-tracks are consistent with belonging to the road. Space-roads with a consistent set of view-tracks are then further sub-divided until a set of roads exists in which each road contains only one view-track in each view. Clusters belonging to these space-roads are input to a three-dimensional straight-line fit resulting in 3-D track parameters in the form of x-z and y-z plane slopes and intercepts.

4.1.2 PWC and SSD track reconstruction

The track finding algorithm for the upstream PWCs is essentially the same as that for the muon chambers described in the previous section with one addition. Due to high hit multiplicity in the SSDs and upstream PWCs, the cluster widths become spuriously large. A fit is, therefore, redone for the valid tracks by taking into account only one wire from each cluster. The final track parameters are taken from the single wire hit combination that results in the smallest χ^2. No space-track fit is done, however, for the SSD system since it lacks a third view.

4.2 Detector module linking

4.2.1 MUON-PWC linking

Muon system tracks are linked with the upstream PWC tracks by projecting x and y view segments from each system to the center of the toroid and looking for position matches.

Segments that meet at the center within a window of 12 cm in both views are considered linked track candidates (see Fig. 4.3) The fairly wide width of the matching window is chosen in consideration of the multiple scattering that occurs in the material between the two systems.

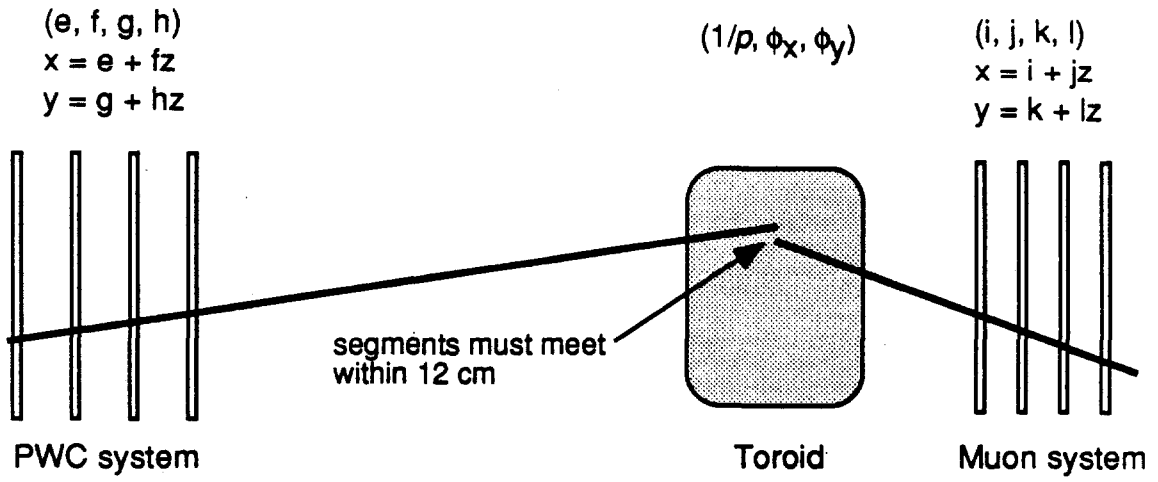

Figure 4.3. Illustration of PWC-MUON system linking.

The MUON-PWC linked track candidates are described by a vector of 8 measured parameters (X) consisting of x-z and y-z slopes and intercepts for both systems, and their error matrix (E). In addition to the measured parameters, the track's inverse momentum ($1/p$) and two multiple scattering angles: one in the x-view (ϕ_x), and the other in the y (ϕ_y), are desired. This gives a total of 11 parameters describing a track, out of which 7 are independent. A fit is done to determine the independent parameters (P) chosen as $1/p$, ϕ_x, ϕ_y, and the slopes and intercepts in the PWC system: e, f, g, and h.

A χ^2 is constructed as:

$$\chi^2 = (\mathbf{X} - \mathbf{A} \cdot \mathbf{P})^T \cdot \mathbf{E}^{-1} \cdot (\mathbf{X} - \mathbf{A} \cdot \mathbf{P}) \tag{4.1}$$

where X, E, P are the previously described vector of measured parameters; the measurement error matrix; and the vector of desired independent parameters, respectively. A is a matrix (of order 11 x 7 in this case) that connects the measurements with the independent parameters. Minimization of this χ^2 gives the independent parameters, which are taken as the muon track production parameters (at this level, the dipole kick in the x-direction can be neglected), subject to a $\chi^2 < 2$ cut. These tracks are referred to as MUON-PWC linked tracks. In the case of ambiguities, up to three PWC-MUON linked combinations are kept for each muon track at this stage. Matching of these tracks to the SSD system and vertex position are used to resolve the ambiguities at a later stage.

4.2.2 Event selection

Good dimuon events were selected by a program that utilized the MUON and PWC track finding and linking procedures described in the previous section. Only tracks passing the MUON-PWC fit with a $\chi^2 < 2$ were considered. At least two muons, each with momenta of at least 20 *GeV/c* were required. In order to remove the background from beam halo, both muons had to point back to the target region. These cuts reduced the sample by a factor of eight, yielding approximately 800K events from the 1990 run. These events are called DIM selected events. In order to get at the high-mass dimuons quickly, especially those from J/ψ, a further selection (called PSI), requiring at least two opposite sign muons with a dimuon invariant mass of greater than 2 GeV/c^2, was made. Thirty-five thousand events passed the PSI selection. All of the E672 physics results presented in this thesis are based on this sample.

4.2.3 Vertex finding and PWC-SSD linking

Muon events passing the selections mentioned in the previous section were sent to a full reconstruction program in which the muons were linked through the entire apparatus, and the other charged tracks in the event were reconstructed. Tracks were found in the separate detector modules in the manner outlined in section 4.1, then the PWC and SSD segments were linked together. Since the SSD system has only two views (x and y), space tracks can not be formed and the linking must be done in the two views separately. The SSD-PWC linking algorithm is illustrated in Fig. 4.4.

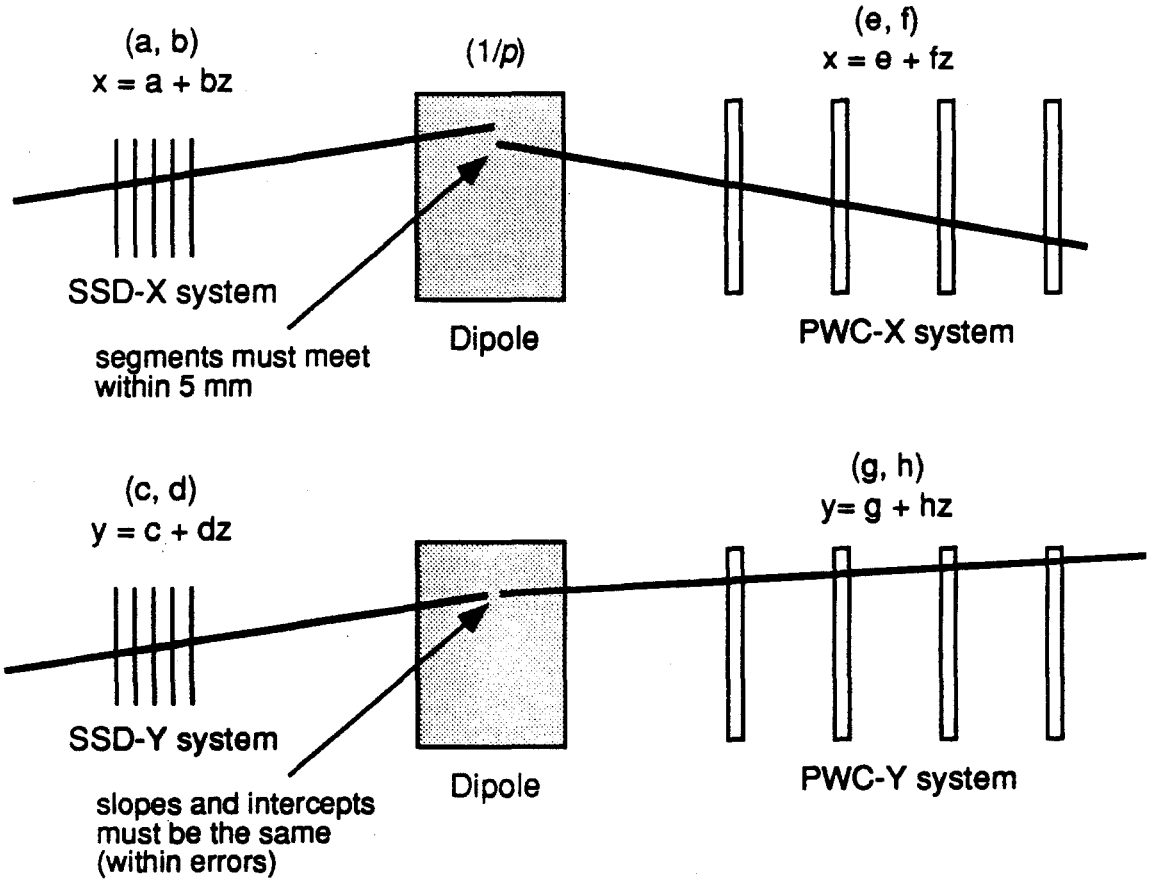

Figure 4.4. Illustration of the SSD-PWC linking algorithm.

The linking in the y view is simple since the dipole magnet between the two systems imparts no momentum kick in this direction. Segments with the same slope and intercept (within errors) in the SSD and PWC systems are considered linked in this view. The dipole imparts a constant p_T of 450 *MeV/c* in the x view. Linking in this view is therefore achieved by projecting SSD and PWC track x-segments to the center of the dipole. Segments are considered linked if they meet at the center of the dipole within a window of 5 mm. Again, in the case of ambiguities, up to three SSD x-links and three y-links are kept for each PWC space track. At this stage of the reconstruction a list of the SSD segments with possible PWC links is made, and these segments are then used to determine the event vertex.

The vertex finding algorithm finds all possible two segment intersections, and then combines intersections that occur at the same positions (within errors). This is done separately in the x and y views, and a list of possible multi-segment intersections is made for each view. The lists are then compared and only intersections that have an intersection occurring at the same z position in the other view (within errors) are kept. This procedure results in a group of three dimensional vertex positions (x, y, z) and a list of segments associated with each vertex. An three-dimensional impact-parameter minimizing fit is then done for these vertices. The reconstructed z-position distribution of primary vertices is shown in Fig. 4.5. The target structure (described in Section 2.4.1) is clearly seen, and comparisons between the apparent, and actual, material size indicate a resolution of 0.35 mm in the longitudinal direction. A transverse resolution of 10 microns has previously been demonstrated (see Fig. 2.3).

The SSD segments that are associated with a vertex in this procedure are then refit using the vertex position as an additional pseudo-plane hit The same type of χ^2 fit as used for the

MUON-PWC linked tracks (Eq. 4.1) was now performed on the SSD-PWC linked tracks, yielding their production momenta and view track parameters (slopes and intercepts).

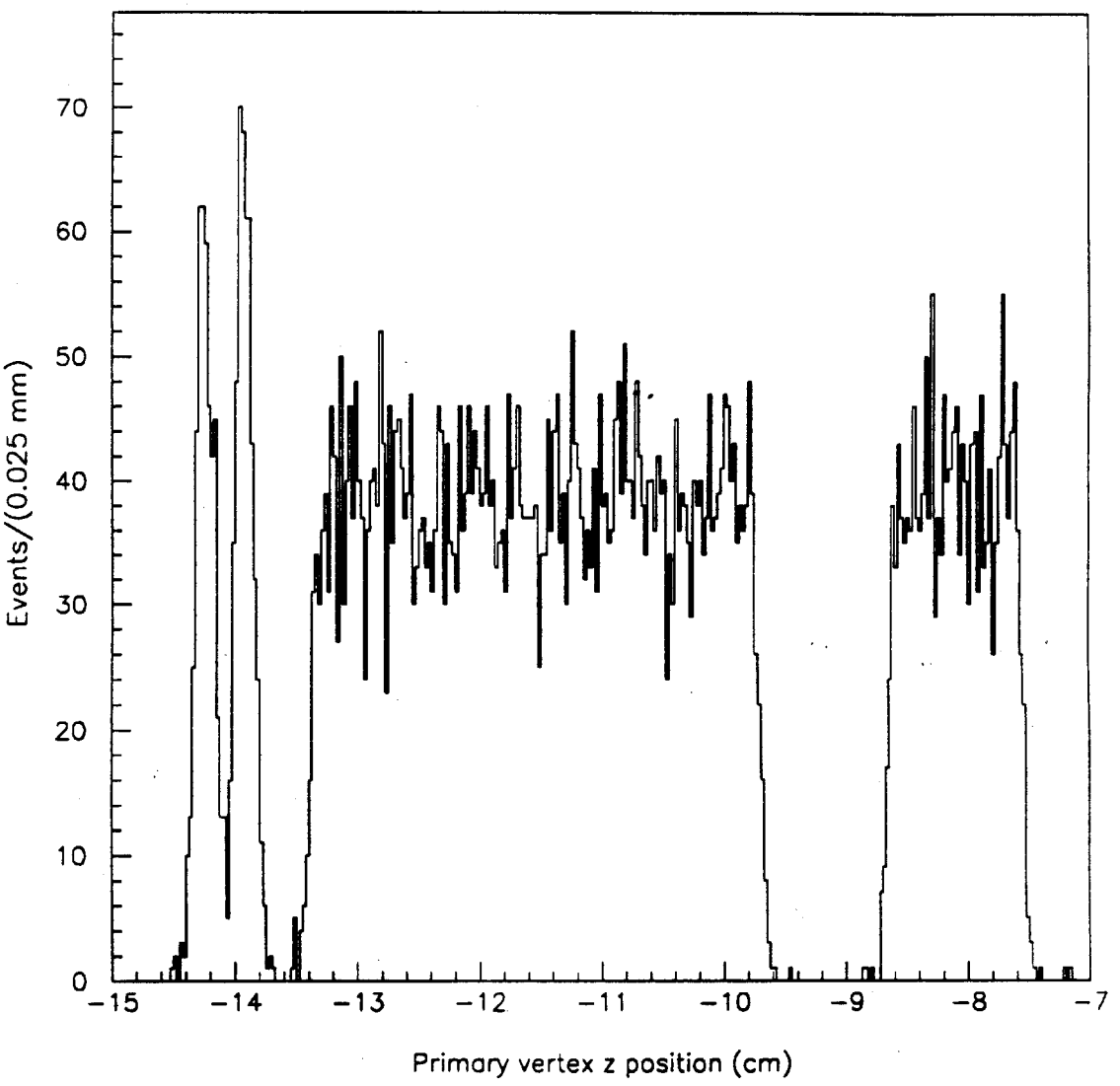

Figure 4.5. Primary vertex reconstructed z position.

4.2.4 SSD-PWC-MUON linking

The final stage of the full tracking program is the linking of muon tracks through the entire spectrometer. SSD-PWC linked tracks are projected to the center of the toroid and position matched to muon tracks in the manner described in section 4.2.1. These fully linked muon tracks are described by 12 measured slope-intercept parameters (4 for each detector module segment). Four additional unmeasured parameters are desired to describe a muon track: the inverse momenta at production ($1/p$) and in the muon system ($1/p_{\mu}$), and the two multiple scattering angles mentioned earlier. Of these 16 quantities 8 are independent, and once again a χ^2 fit (Eq. 4.1) is done to determine the momenta (2 parameters), production slopes and intercepts (4 parameters), and multiple scattering angles (2 parameters). A consistency, accounting for energy loss, between the production momentum (determined by the dipole bend) and the muon system momentum (determined by the toroid bend) is required in this fit. This procedure reconstructs muons with an efficiency of about 90% per track, with a momentum resolution of:

$$\frac{\delta p}{p} = 0.05\% p,$$

which is demonstrated by the slope of the fractional momentum error distribution as a function of momentum as shown in Fig. 4.6.

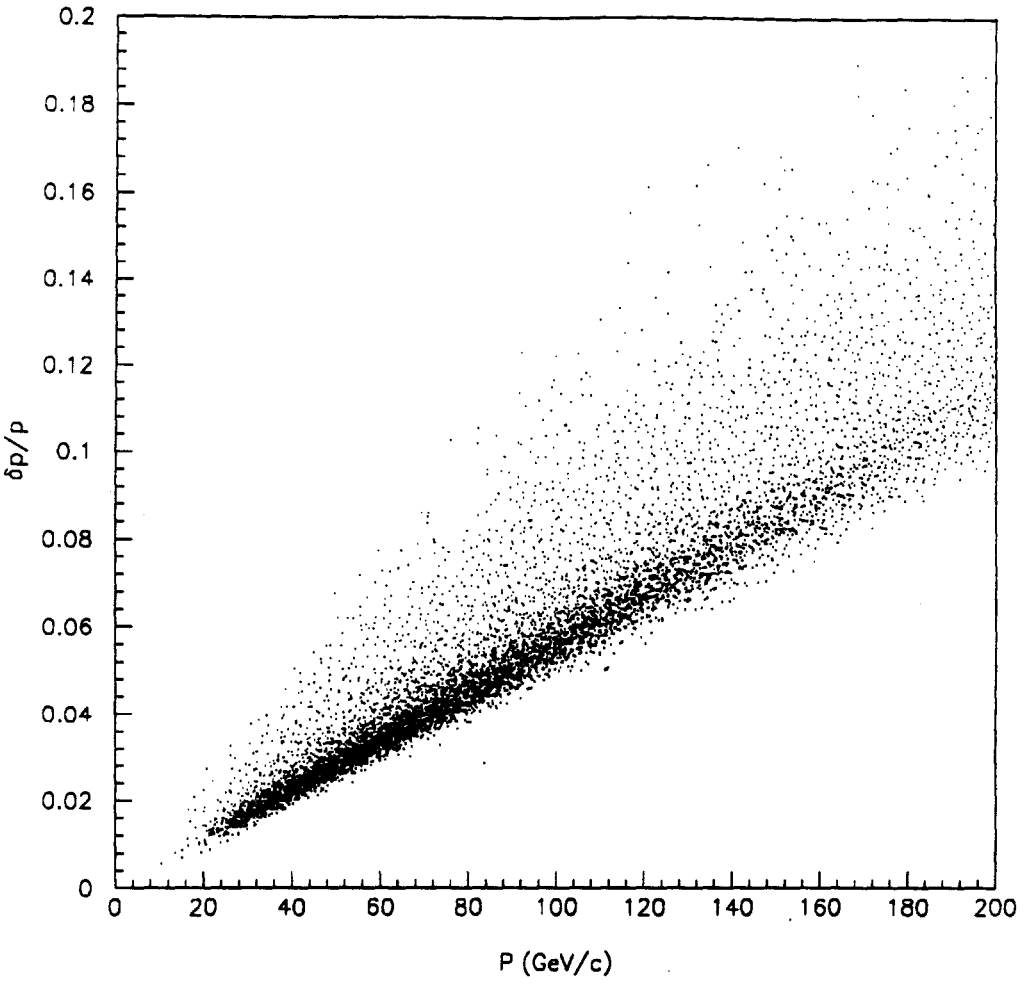

Figure 4.6. Fractional momentum error vrs. momentum for fully linked muon tracks.

4.3 Reconstructed event characteristics

The selection and reconstruction programs described in the previous sections yielded approximately six-hundred-thousand events in which two or more muons were fully linked. 438K events have opposite sign muon pairs, and 203K have like-sign pairs (181K negative pairs, and 22K positive pairs). There are also 1123 three-muon events in the sample.

The invariant mass distribution for opposite sign muon pairs is shown in Fig. 4.7. The vector mesons ρ/ω, ϕ, and J/ψ are clearly resolved.

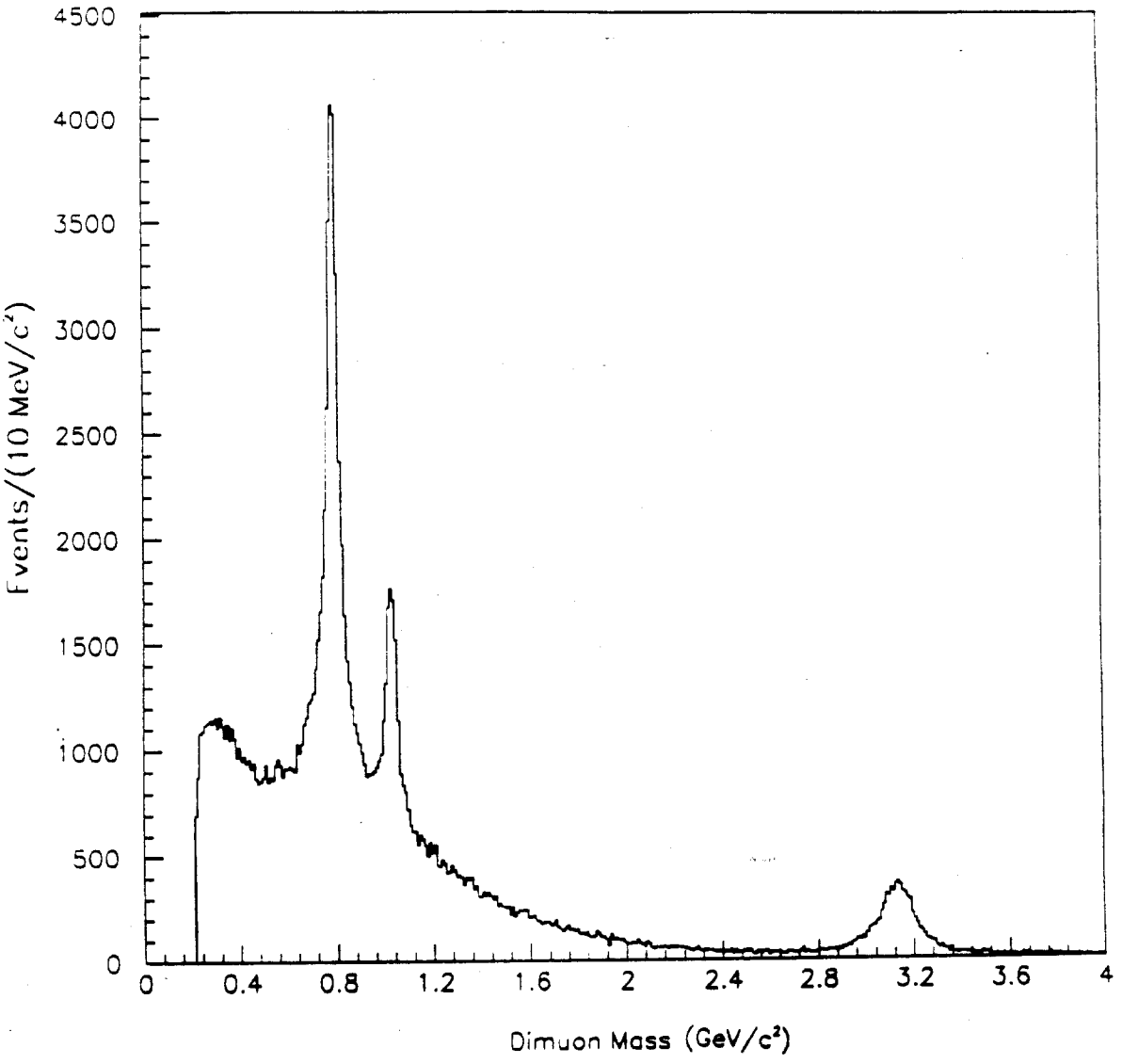

Figure 4.7. Reconstructed opposite-sign dimuon invariant mass.

Figure 4.8 shows the reconstructed opposite-sign dimuon mass distribution for the PSI selected events (see section 4.2.2). There are about thirty-five thousand opposite-sign dimuons in this sample. A two-resonance plus background fit to this sample yields 11,200 ± 440 J/ψs, and 341 ± 89 $\psi(2S)$s. Both resonances have a reconstructed mass resolution of 85 MeV/c^2.

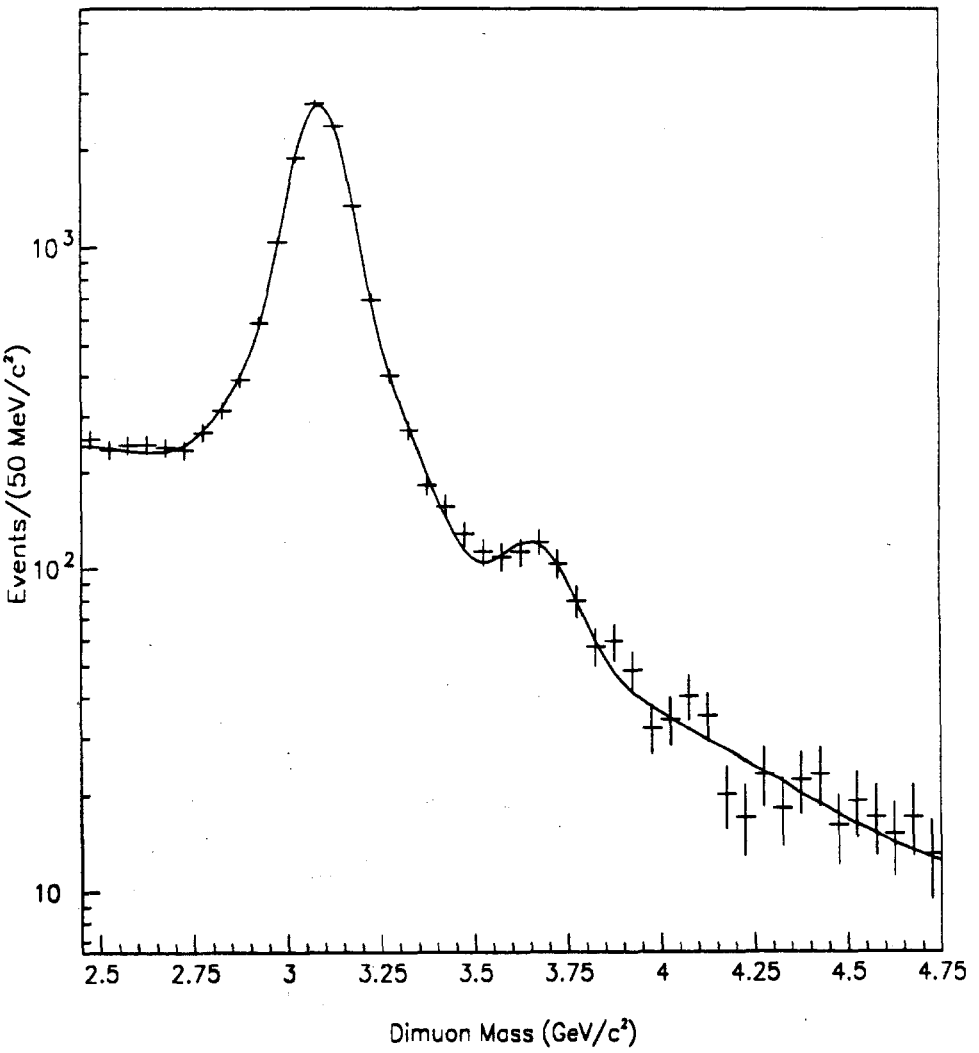

Figure 4.8. Reconstructed opposite-sign dimuon invariant mass for PSI selected events.

The $J/\psi\pi^+\pi^-$ invariant mass distribution as shown in Fig. 4.9 shows a clear peak at the $\psi(2S)$ mass. The number of $\psi(2S)$ events reconstructed in this mode (about 300) is consistent with the number of events observed in the dimuon channel, when both are corrected for acceptance and reconstruction efficiencies, demonstrating that we understand these corrections [42].

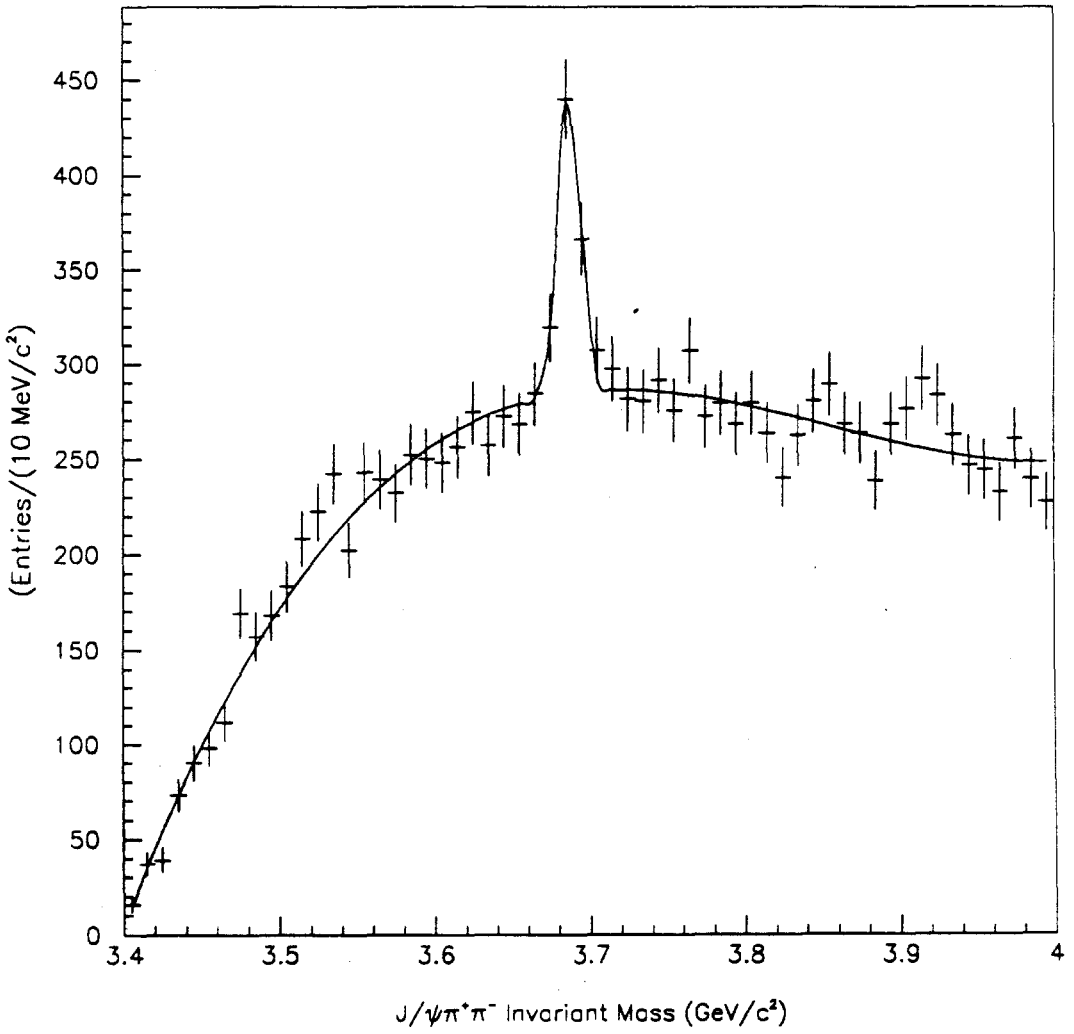

Figure 4.9. Reconstructed $J/\psi\pi^+\pi^-$ invariant mass distribution.

CHAPTER 5

B DECAYS WITH J/ψ IN THE FINAL STATE

Experiments UA1 and CDF have shown the usefulness of the J/ψ meson as a tag for b quark decays [13, 14] (see Chapter 1). Although the associated branching ratios are small, the J/ψ, through its decay into muons, provides a clean signal (as demonstrated in Chapter 4), and a straight-forward trigger. Another advantage of decays into J/ψ is that, in many instances, the final state involves only charged particles, thus allowing full reconstruction of the mass and momentum of the decaying B. E672 is also capable of reconstructing both the primary and secondary vertices, i.e., measuring the B decay length, which, combined with the mass and momentum measurement, completely specifies the B time of flight.

5.1 Decay modes and branching ratios

In this thesis, the generic symbol B is used to refer to any particle containing a b quark. There are three known mesons that contain b quarks: B^+, B^0, and B_s. The B^+ is composed of a $u\bar{b}$ quark-antiquark pair, the B^0 is a $d\bar{b}$ pair, and the B_s is a $s\bar{b}$ pair. In addition to these mesons (and their charge conjugates), there also exist baryons which contain a b quark. All of these particles have significant decay modes containing the J/ψ in the final state [9, 10, 17].

The dominant diagram for B decay into J/ψ is the spectator decay shown in Fig. 5.1. It consists of a $b \rightarrow c$ transmutation in which the W decays into a $s\bar{c}$ pair. The resulting charm quarks pair up to form a charmonium bound state, and the s quark and spectator quark hadronize into a variety of states having strangeness. This is a color-suppressed decay

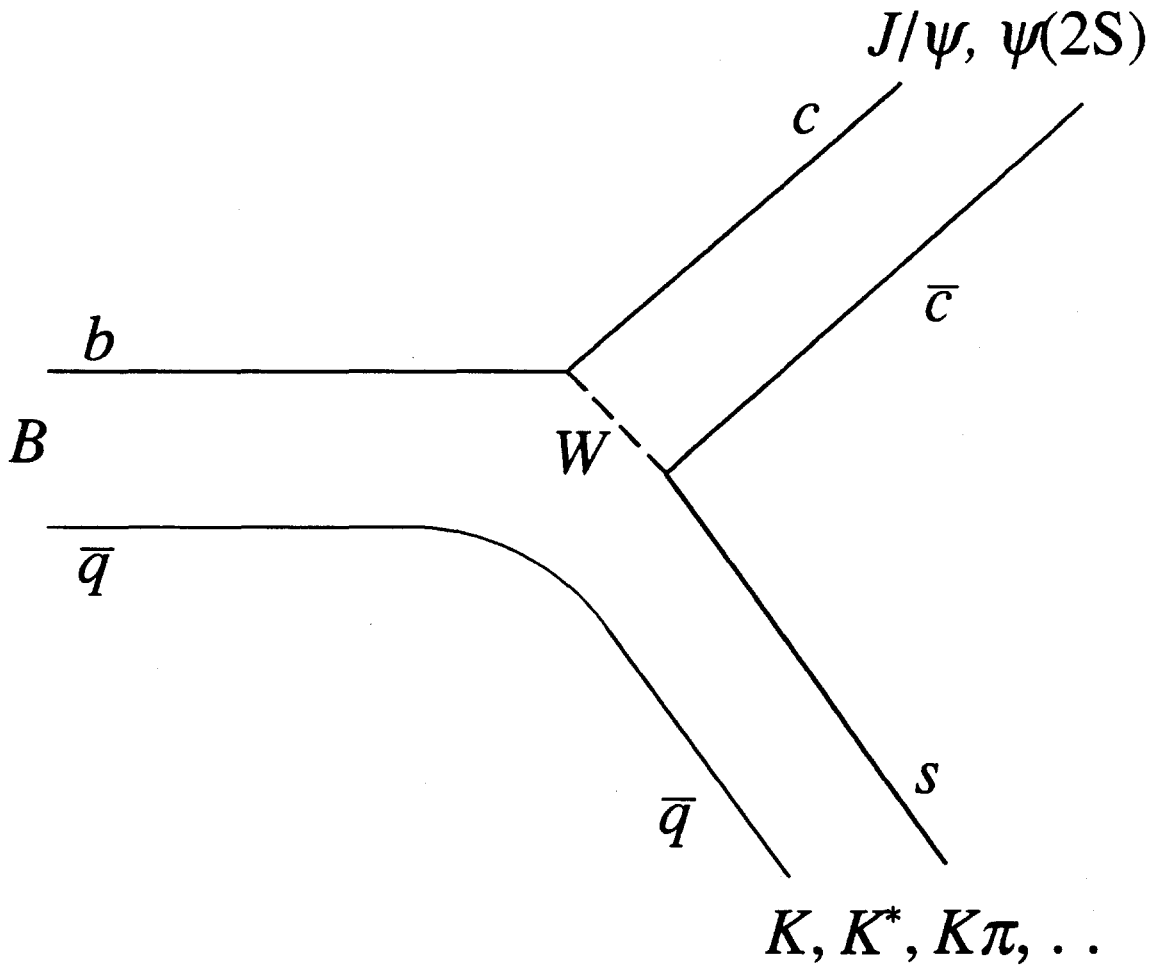

Figure 5.1. Quark diagram for B decay with J/ψ in the final state.

in that, in order to form charmonium, the $c\bar{c}$ pair must be produced in a colorless state. The Cabibbo favored final states for W decay are:

$$W \rightarrow \begin{pmatrix} d \\ \bar{u} \end{pmatrix}, \begin{pmatrix} s \\ \bar{c} \end{pmatrix}, \begin{pmatrix} e \\ \bar{\nu}_e \end{pmatrix}, \begin{pmatrix} \mu \\ \bar{\nu}_\mu \end{pmatrix}, \begin{pmatrix} \tau \\ \bar{\nu}_\tau \end{pmatrix}.$$

Due to the quark's color degree of freedom, there are three times as many available states in the hadronic channels as in the leptonic modes. The W, therefore, decays into the above final states with the weights 3 : 3 : 1 : 1 : 1, respectively. Only one of the three charm channels (the one with the anti-color of the c-quark from the $b \rightarrow c$ transmutation) is, however, available for charmonium production. This suppression can be overturned by the emission of a gluon in the charmonium formation, de-colorizing the state. This processes is suppressed by an order of α_s, but in the case of soft-gluon emission, α_s is on the order of unity.

The branching ratio for the inclusive process $B \rightarrow J/\psi + X$ has been measured by ARGUS and CLEO to be (1.12 ± 0.16)% [9, 10]. This branching ratio was measured for Bs produced at the upsilon(4S) resonance and therefore involves a mixture of B^+ and B^0 mesons only (the upsilon(4S) is too light to produce B_s mesons or b-baryons). CERN experiment L3 has recently published a $B \rightarrow J/\psi + X$ branching ratio of (1.3 ± 0.4)%, measured at the Z resonance, which includes decays from all b-hadron species [11]. This is the value appropriate for this analysis, since all B types, including baryons, are produced in high-energy hadronic collisions. In addition to the inclusive branching ratio, ARGUS and CLEO have measured exclusive B-decay branching ratios with the J/ψ in the final state [9, 10]. E672 detects J/ψs by their decay into opposite-sign muon pairs. The branching ratio for this decay has been measured by MARK III to be (5.97 ± 0.25)% [43]. The combined branching ratios for the exclusive B decays experimentally accessible to E672 (those with charged particles only in the final state) are

shown in Table 5.1.

Table 5.1. Branching ratios for B-decay modes with J/ψ in the final state.

Decay mode	Combined Branching Ratio
$B \rightarrow J/\psi X \rightarrow \mu^+\mu^- X$	$(7.8 \pm 2.4)\times10^{-4}$
$B^+ \rightarrow J/\psi K^+ \rightarrow \mu^+\mu^- K^+$	$(4.6 \pm 1.2)\times10^{-5}$
$B^+ \rightarrow J/\psi K^+ \pi^+\pi^- \rightarrow \mu^+\mu^- K^+ \pi^+\pi^-$	$(6.6 \pm 2.9)\times10^{-5}$
$B^0 \rightarrow J/\psi K_s^0 \rightarrow \mu^+\mu^- \pi^+\pi^-$	$(1.3 \pm 0.6)\times10^{-5}$
$B^0 \rightarrow J/\psi K^{0*} \rightarrow \mu^+\mu^- K^+\pi^-$	$(7.7 \pm 2.3)\times10^{-5}$
$B^0 \rightarrow J/\psi K^+\pi^-$ (non-res) $\rightarrow \mu^+\mu^- K^+\pi^-$	$(6.0 \pm 3.0)\times10^{-5}$

5.2 Decay signatures and backgrounds

$B \rightarrow J/\psi + X$ decays are uniquely tagged by J/ψs emerging from secondary vertices. As was shown in the previous chapters (see Figs. 2.3 and 4.4), we are able to reconstruct primary vertices with an average resolution of 10 μm in the transverse plane and 0.35 mm in the longitudinal direction. Monte Carlo studies indicate that Bs produced at E672's fixed-target energy travel, on average, a distance of 1.6 cm in the longitudinal direction and 150 μm in the transverse plane (see next section). Since these decay lengths are much larger than the vertex resolutions, it is expected that both the primary and secondary vertices should be resolved in a substantial number of the B decays occurring in our apparatus. The actual number reconstructed depends on the efficiencies of the reconstruction and analysis programs, described in the next chapter. A significant background to secondary-vertex J/ψs from B decays is produced by secondary interactions, events in which a high-momentum

particle from the primary interaction interacts further downstream in the target and produces a J/ψ. Events with J/ψs from vertices in regions where no target material is present are particularly interesting because they do not suffer from this background.

5.3 Monte Carlo simulations

Monte Carlo simulations were used to tune analysis programs, evaluate the detector acceptance, and find reconstruction-program efficiencies. These were GEANT3-based full detector simulations [44]. Kinematically correlated beauty-particle pairs were generated according to distributions in x_F and p_T measured by E653 [45], given by:

$$\frac{d^2\sigma}{dp_T dx_F} \propto \left(1-\left|x_F - x_0\right|\right)^n \cdot e^{-bp_T^2}, \tag{5.1}$$

$$\text{with } x_0 = 0.17 \pm 0.09,\ n = 3.6^{+2.3}_{-1.7},\ \text{and } b = 0.09^{+0.04}_{-0.03}.$$

Pairs were generated with parameters equal to the central values given above, and, in addition, with values varied within the corresponding errors (in order to determine systematic uncertainties). The theoretical distributions given by NDE [1] and Berger [2] were fit to the form given in Eq. (5.1), and the parameters found were consistent with those measured by E653 within relatively large errors. The offsets, x_0, found in these fits are, however, systematically lower than the values obtained by E653. The implications of this discrepancy are discussed in Chapter 9. The generated Bs were made to decay according to an exponential distribution with a mean lifetime of 1.32 ps, as measured by LEP [11] (this value was varied by ± 0.2 ps in order to determine systematic uncertainties). One of the Bs in each event, chosen at random, was forced to decay into a J/ψ + hadrons, with the J/ψ subsequently decaying into a muon pair. The other B in the event was made to decay into

a kaon plus a randomly chosen number of pions (up to a maximum of 5). Fig. 5.2 shows the decay-length distributions in the longitudinal and transverse directions for the Monte Carlo generated *B* events. The mean decay length in the longitudinal direction is 1.6 cm, and that in the transverse is 150 μm.

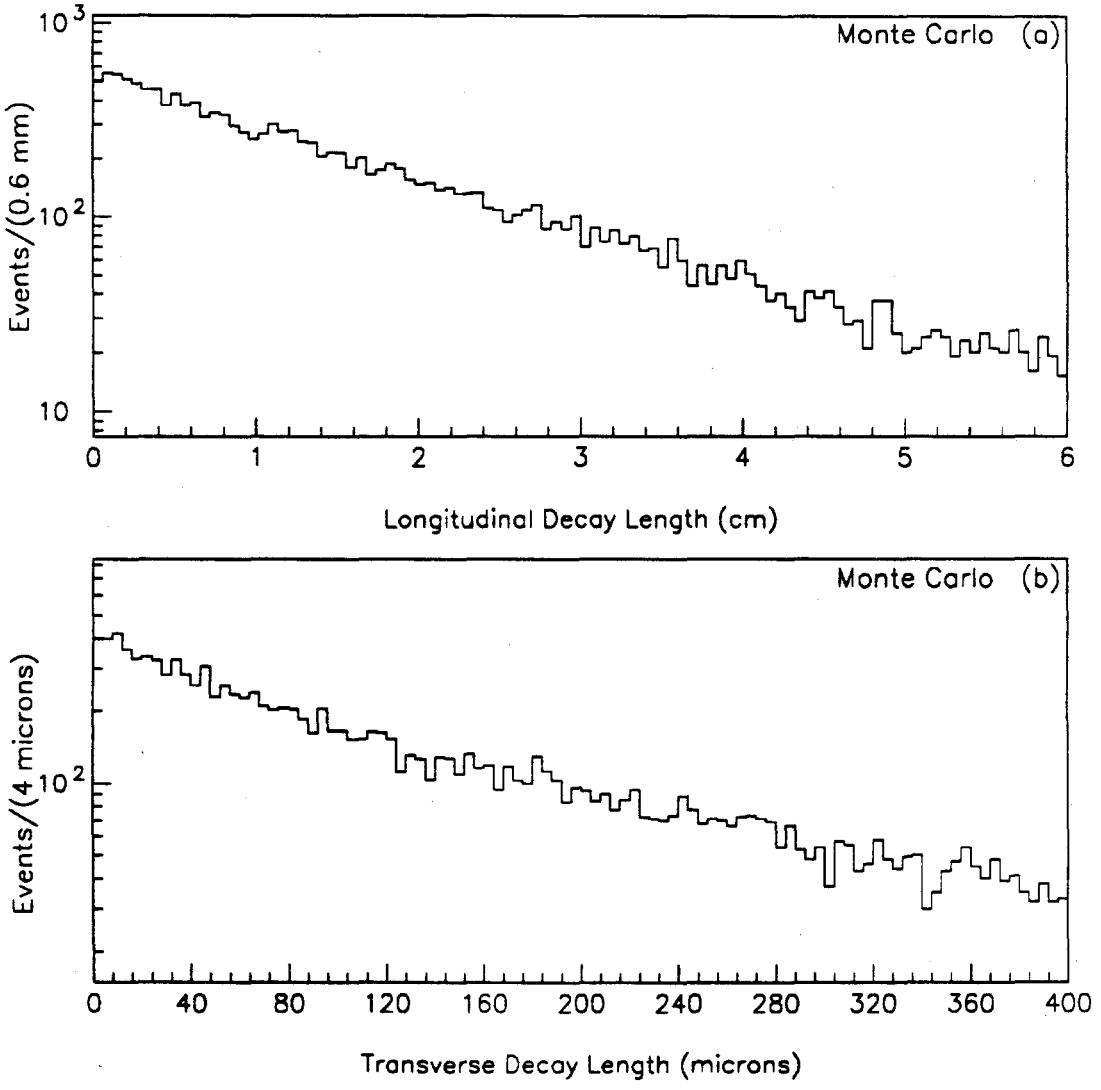

Figure 5.2. Monte Carlo *B* decay lengths, (a) in the longitudinal direction; (b) in the transverse plane.

The acceptance for dimuons from $B \rightarrow J/\psi + X$ decays as a function of the B's p_T is fairly flat up to a value of 4 *GeV/c*. The two-dimensional acceptance as a function of x_F and p_T is shown in Fig. 5.3; the acceptance is non-zero only in the forward region ($x_F > 0$), and has an integrated value of 33% in the region $0.1 < x_F < 0.8$, $p_T < 4.0$.

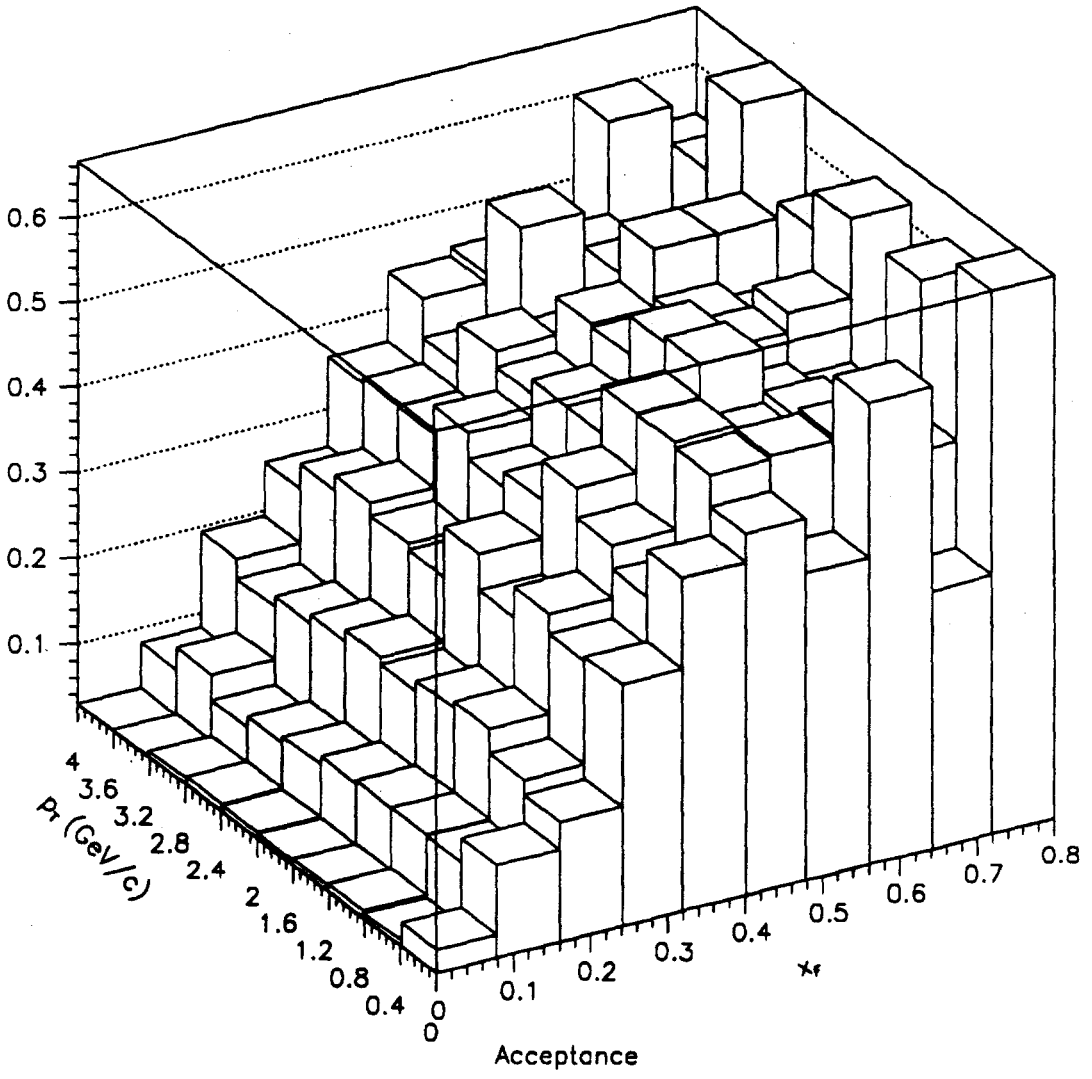

Figure 5.3. Two-dimensional acceptance for dimuons from B decays as a function of x_F and p_T of the B.

Hadrons for the underlying event were generated subject to energy and momentum conservation using a longitudinal phase space model [46]. The GEANT physics processes were implemented in this simulation (multiple scattering simulation is particularly important for the vertex reconstruction efficiency). The events were digitized as spectrometer hits (with appropriate detector noise and efficiency included) and a fake raw-data file was generated and run through the reconstruction and analysis programs. Figures 5.4-5.7 demonstrate how well the Monte Carlo event characteristics represent those of the real dimuon data. Figure 5.4 shows the distribution of impact parameters with respect to the primary vertex for charged tracks. The similarity between the generated and data distributions show that multiple scattering in the target is well simulated by GEANT; a crucial point for vertex finding analysis. The Monte Carlo multiplicity and momentum distributions are also shown to be consistent with those from the data in Figs. 5.5-5.7. Note that the hump in the p_T distributions at 1.5 *GeV/c* is due to muons from J/ψ decays.

Similar Monte Carlo simulations were done for direct and secondary-interaction J/ψ events. For the secondary-interaction simulation, ISAJET was used to generate particles from general pion-nucleus collisions [47]. Leading hadrons were allowed to interact further downstream in the target, with the probability of producing a J/ψ determined by the amount of material traversed and the J/ψ cross-section evaluated at the interacting particle's momentum.

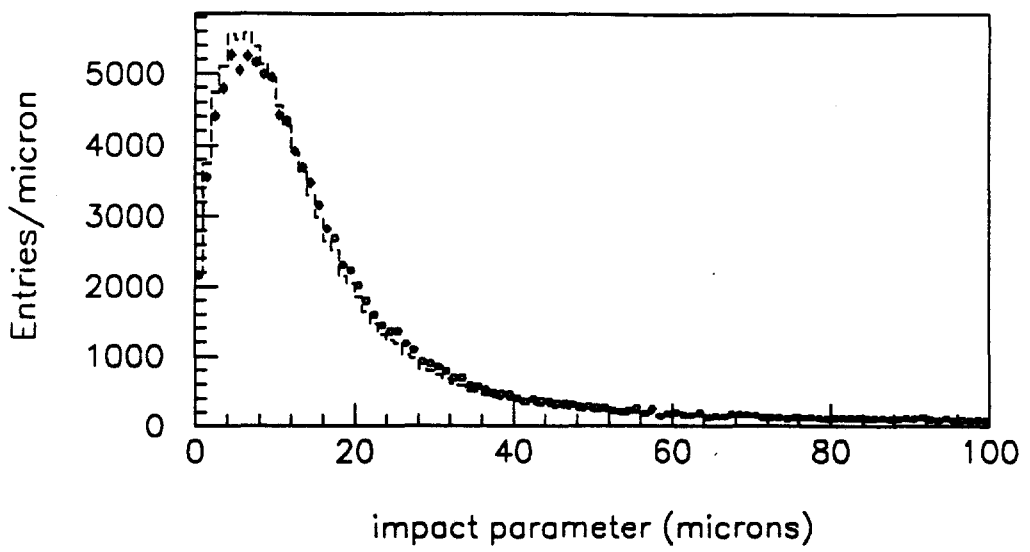

Figure 5.4. Distributions of impact parameter with respect to the primary vertex for charged tracks. Points are from dimuon data; dashed histogram is from Monte Carlo.

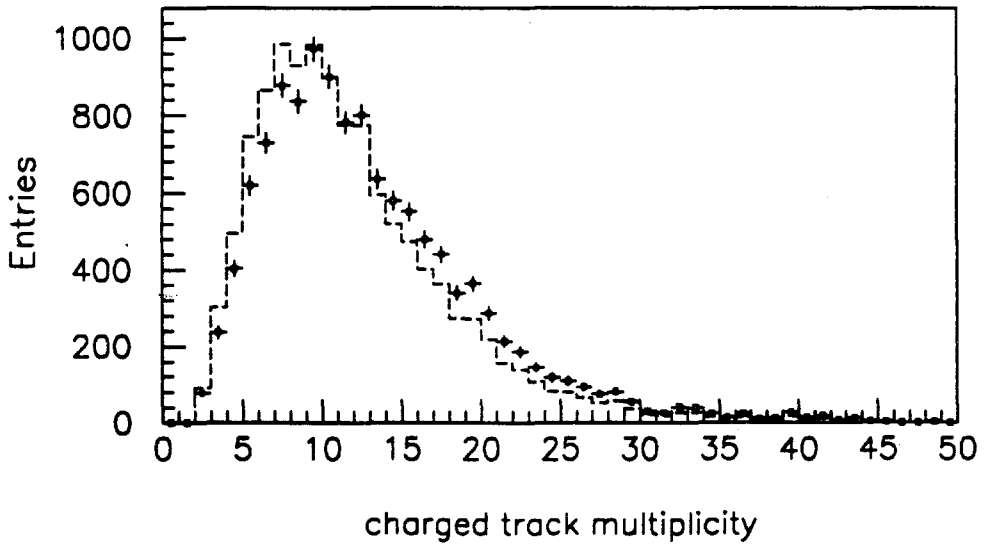

Figure 5.5. Charged track multiplicity distributions. Points are from dimuon data; dashed histogram is from Monte Carlo.

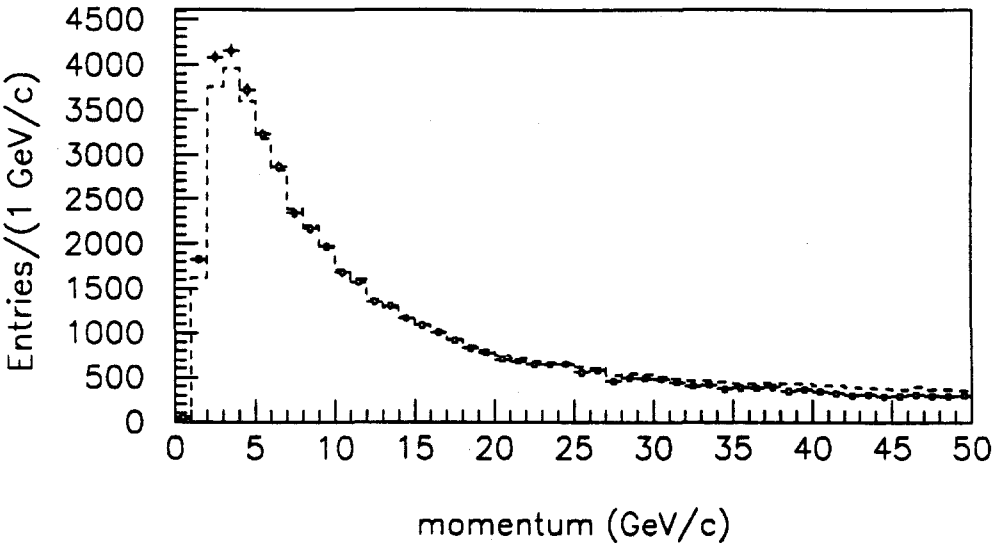

Figure 5.6. Charged track momentum distributions. Points are from dimuon data; dashed histogram is from Monte Carlo.

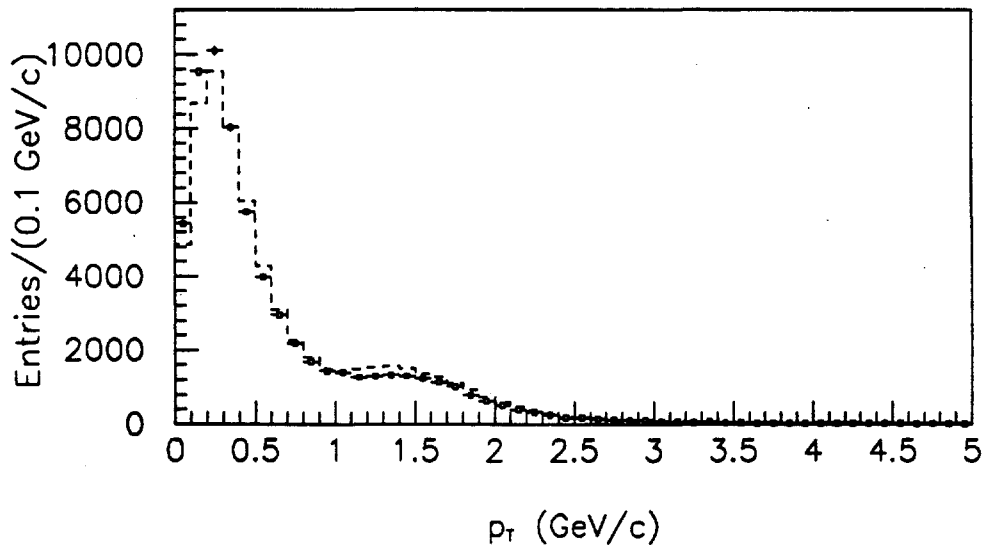

Figure 5.7. Charged track p_T distributions. Points are from dimuon data; dashed histogram is from Monte Carlo. The bump at 1.5 *GeV/c* is due to muons from J/ψ decay.

CHAPTER 6

J/ψs FROM SECONDARY VERTICES

The key to the analysis of $B \rightarrow J/\psi + X$ events lies in the reconstruction of the J/ψ vertex position. Since in many of these decays the secondary vertices have small multiplicities, there is a high probability that they will be missed by the initial vertex finding. A muon-oriented vertex finding procedure was, therefore, developed to reconstruct these vertices more precisely and with higher efficiency.

6.1 Dimuon oriented vertex finding

The J/ψ vertex position was found by a muon-oriented vertex refit: opposite sign muon pairs were selected in the mass range 2.85 $GeV/c^2 < M_{\mu\mu} < 3.35$ GeV/c^2. Those pairs that had consistent intersections in the x-z and y-z planes (those occurring at the same z position, within errors), were subject to a χ^2-minimizing fit with simultaneous vertex and J/ψ mass constraints (described in Appendix A). The resulting vertex was then used as a seed for an iterative vertex-fitting procedure which associated other charged tracks to this vertex. Only SSD-PWC linked tracks with transverse impact parameter within 1.5 standard deviations of the J/ψ vertex seed position were used in the fit. The reconstructed J/ψ vertex z-position distribution from the 1990 PSI-selected (see Chapter 4) data using this method is shown in Fig. 6.1. Almost all of the J/ψs in this sample are either produced directly or are from prompt decays of higher-energy charmonium states. The muon-oriented vertex finding algorithm should, therefore, reproduce the event's primary vertex in most cases, excluding secondary interactions and B decays.

That this indeed occurs is demonstrated by the target elements being clearly resolved in Fig. 6.1. It is also shown explicitly in Fig. 6.2, which shows the z-position differences between the primary and J/ψ vertices. The peak centered at zero in Fig. 6.2 is due to J/ψs

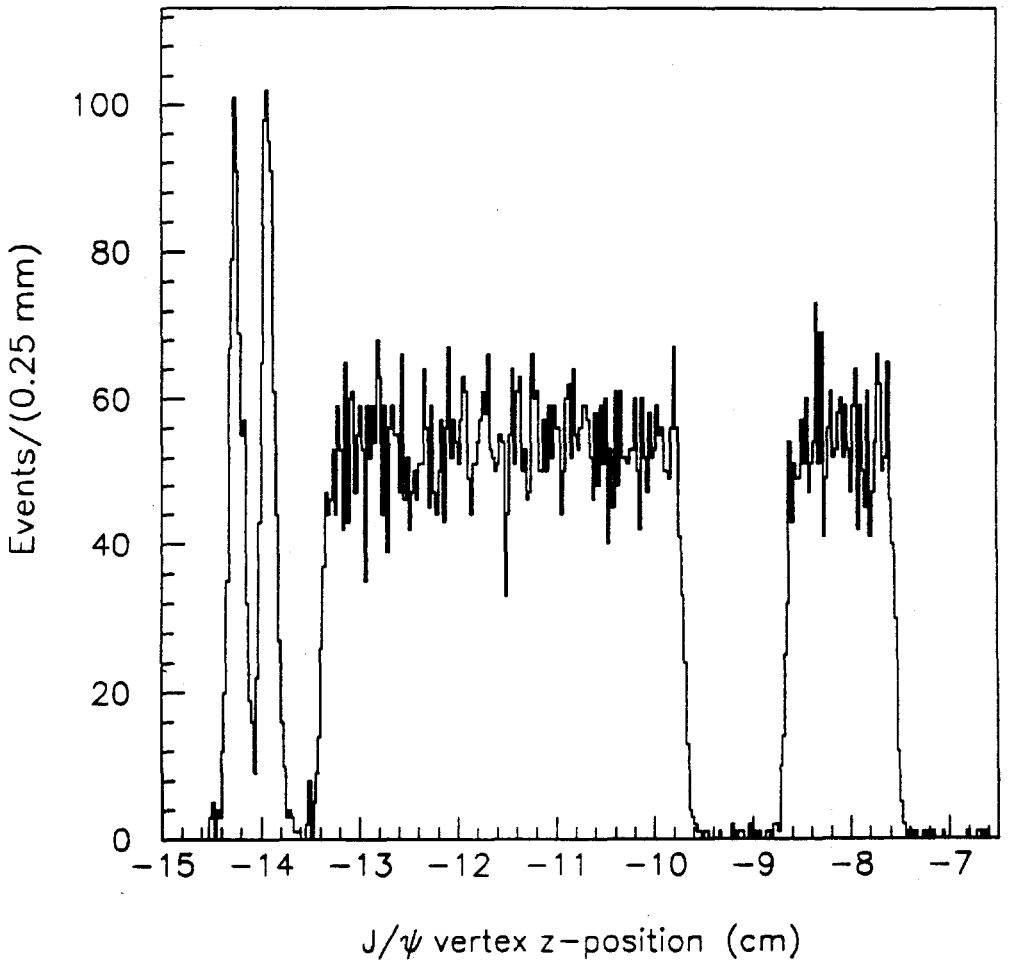

Figure 6.1. Reconstructed J/ψ vertex z-position distribution.

from primary vertices, while the entries at positive difference greater than 1 mm are attributed to secondary-vertex J/ψs from secondary interactions and B decays. The few events with a J/ψ vertex reconstructed well upstream (more than 1 mm) of the event's primary vertex (negative entries in Fig. 6.2) are attributed to false vertex reconstruction.

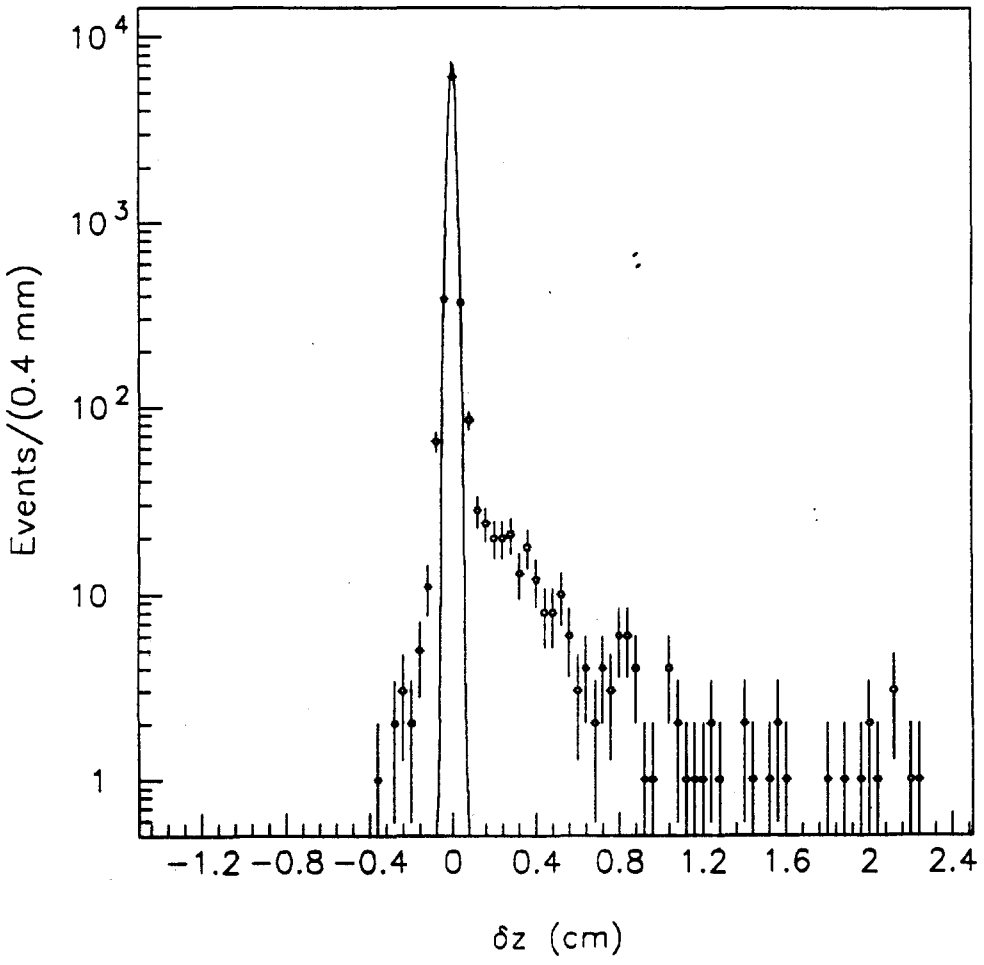

Figure 6.2. Difference between primary vertex z-position and J/ψ vertex z-position (J/ψ - primary).

The vertex-finding procedure was also tested on *B* Monte Carlo events (as described in Chapter 5). Figure 6.3 shows the differences between the reconstructed and Monte Carlo generated secondary J/ψ vertex positions in the longitudinal (z) and transverse (x, y) directions. These residuals agree with the uncertainties given by the vertex fit and the expected detector resolutions of σ_z = 0.35 mm, and σ_T = 10 μm.

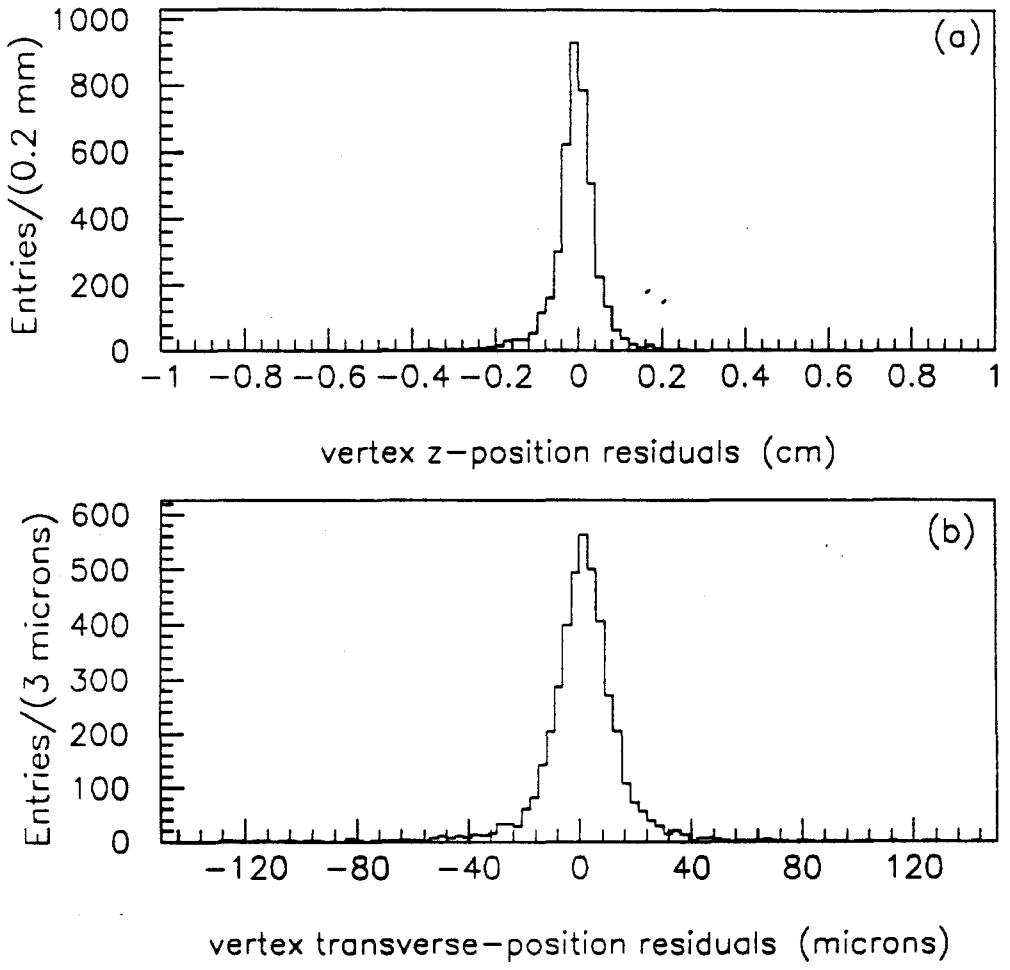

Figure 6.3. Difference between reconstructed and generated J/ψ secondary-vertex positions: (a) in the z direction; (b) in the transverse plane.

6.2 Vertex quality cuts

The event sample was then searched for cases in which the J/ψ vertex was downstream of the primary vertex. In order to clean the sample, several cuts were applied to these events:

(i) Only events with at least three SSD-PWC-vertex linked tracks from the primary vertex were kept, and a beam track having an impact parameter within 1.5 sigma of the primary vertex was required. Secondary J/ψ vertices with a beam track pointing at them within 1.5 sigma were discarded (631 events passed this cut).

(ii) Fiducial-volume cuts were made for both primary and secondary vertices: the primary had to come from the target region, and the secondaries had to be upstream of the first SSD plane (577 events passed these cut).

(iii) A significance greater than 3 was required for both the longitudinal and transverse separations between the primary and secondary vertices, with significance defined as the separation divided by the combined vertex uncertainty. An absolute longitudinal separation of 2.5 mm was also required (121 events passed these cuts).

(iv) Secondary J/ψ vertices with more than four associated hadrons were discarded in order to reduce the background from secondary interactions (73 events passed this cut).

6.3 The secondary vertex J/ψ sample

The primary- and secondary-vertex z-position distributions for the seventy-three events passing these cuts are shown in Figs. 6.4b and 6.4c, respectively (Fig. 6.4a shows the z-distribution for the primary-vertex J/ψs for reference, since the gaps in the target structure are visible in this distribution). Notice that there are events in which the secondary J/ψ

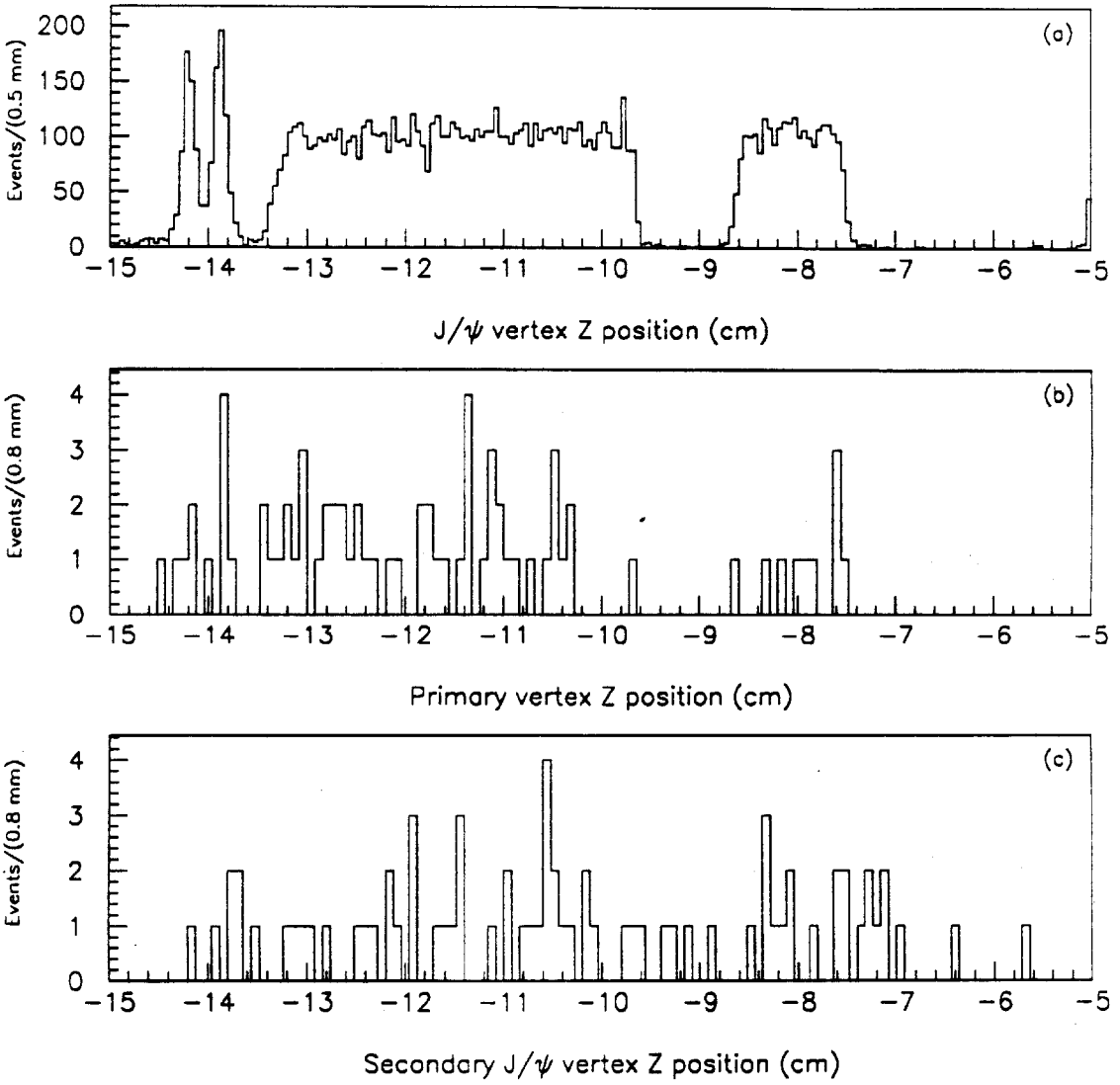

Figure 6.4. Vertex z-position distributions: (a) J/ψ vertex position for all events; (b) primary vertex position for events with a secondary J/ψ vertex (passing cuts); (c) secondary J/ψ vertex position for these events.

vertex occurs in the gap regions, and that none of the primary vertices occur in these regions.

The background to this signal from false vertex reconstruction was estimated using various methods. In one, the exact same set of cuts was imposed on the few events shown in Fig. 6.2 in which the reconstructed J/ψ vertex was upstream of the primary. None of these events passed all the cuts. A Monte Carlo simulation (as described in Chapter 5) of directly produced J/ψs with LPS-generated hadrons was also used to check background. The same procedure used on the real data was performed on these events, yielding a probability of $(3.2 \pm 1.4)\times10^{-4}$ for a spuriously reconstructed direct J/ψ event to pass the vertex quality cuts. Normalizing to the original 11.2K J/ψ events, the estimated background to the secondary-vertex J/ψ sample from false vertices is 4 ± 2 events. Another possible source of background comes from dimuon events coming from other physics processes (most notably double semileptonic D decays) in which the muons coincidentally meet to form a vertex and an invariant mass in the J/ψ range. The background from these types of events was estimated by taking dimuon pairs with an invariant mass in the side-band ranges above and below the J/ψ (excluding the $\psi(2S)$ mass range) and performing the same fit (with the mass constrained to that of the center of the band) and analysis as was used for the J/ψ. No events passed these cuts. As is the case with fake reconstruction, vertices from this type of background can occur upstream of the primary vertex as well as downstream of it. The absence of vertices passing the quality cuts occurring upstream of the primary vertex is strong evidence that this sample is relatively free of background, except, of course, that due to secondary interactions. Although the requirement of low secondary multiplicities certainly improves the likelihood of the J/ψ coming from a B decay, secondary-interaction events remain in the sample.

There are two reasonably large regions in the fiducial volume of the target-SSD system where there is no material present: -9.61 cm < z < -8.62 cm, and -7.50 cm < z < -5.1 cm. Events with secondaries in these gaps cannot contain a background from secondary interactions. The positions in the z-y plane of the J/ψ vertices in these gaps are shown in Fig. 6.5 (with z error bars). The hatched areas represent the Be target material, and the line at -5.6 cm represents the Mylar-foil window of the first SSD plane.

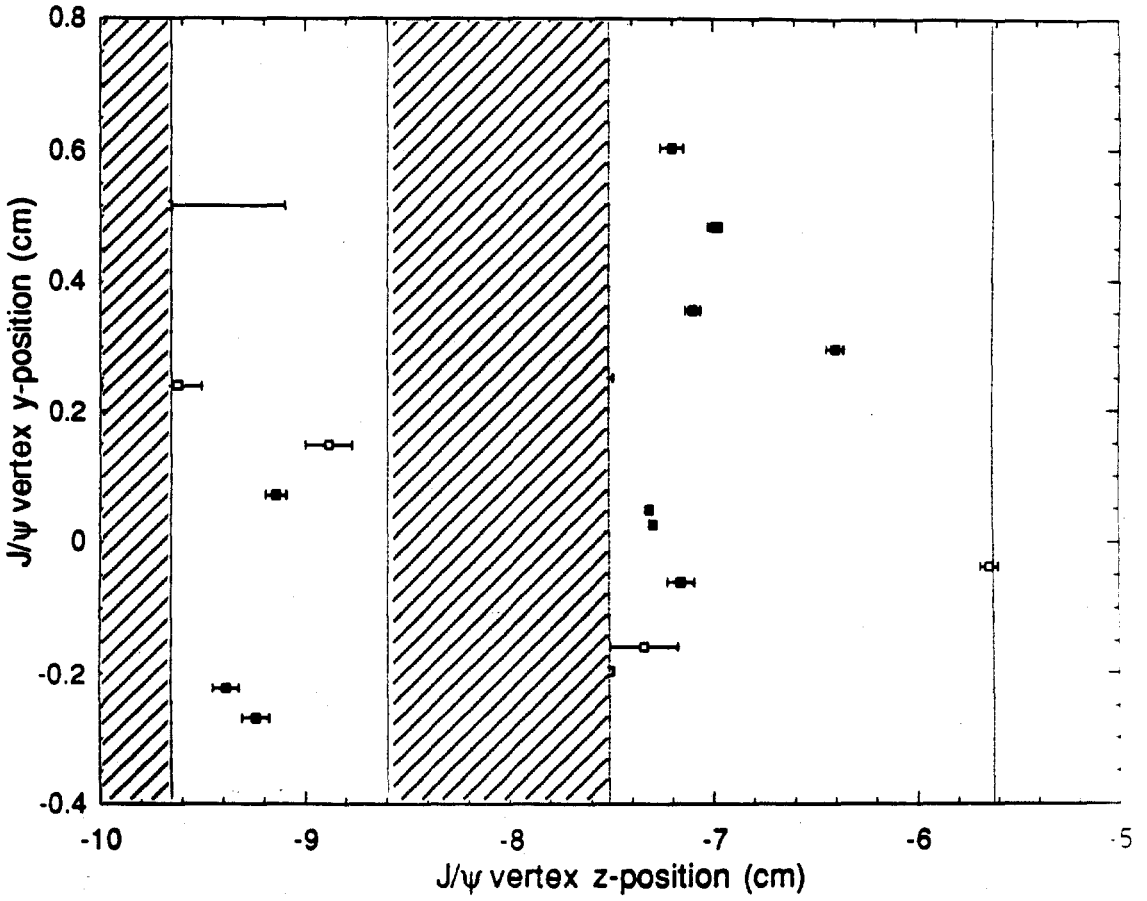

Figure 6.5. Secondary J/ψ vertex position in the y-z plane, showing events with vertices in gaps where no material is present. Hatched areas represent target material; the line at -5.6 cm represents a Mylar-foil window

There are ten events in which the J/ψ vertex is at least three standard deviations away from a region where material is present (these events are shaded in Fig. 6.5). In three events the vertex occurs in the air gap region between the Be targets, while seven events have their vertex occurring in the air gap between the upstream Be and the first SSD plane. Using secondary-vertex distributions from Monte Carlo simulations (see Fig. 6.6), the total number of J/ψs from B decays in the fiducial volume can be extrapolated from the number occurring in the gaps.

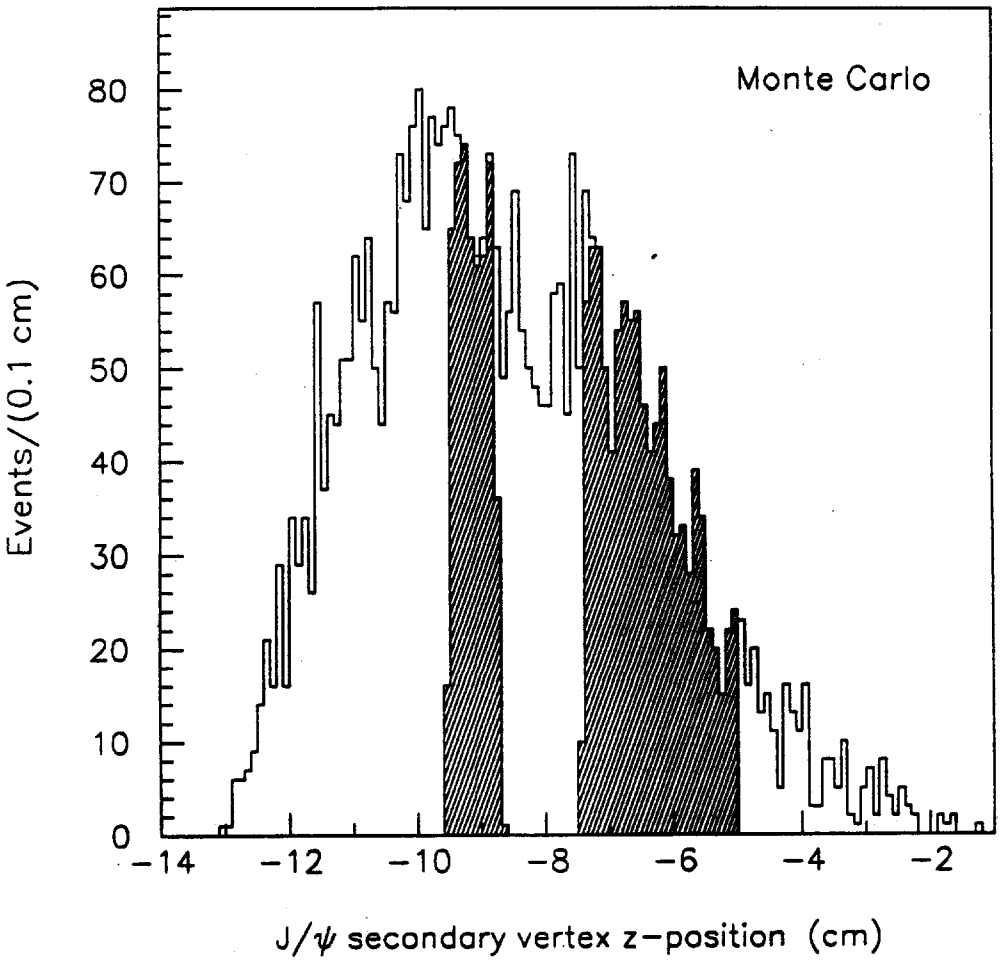

Figure 6.6. Secondary vertex distribution for J/ψs from B decays. Vertices occurring in air gap region are shaded

This analysis indicates that (35 ± 5)% of the total decays occur in the gap regions, and that approximately twice as many events should have their secondary vertices occurring in the downstream gap as in the upstream one. The ratio obtained from the data is 2.3. One of the estimated 4 ± 2 background events from fake vertex reconstruction is estimated to occur in the gaps. With this considerations, a background subtracted signal of 9 ± 3 secondary-vertex J/ψ events from B decays in which the secondary vertex occurs in a region where no material is present is obtained. Extrapolating, it is estimated that 26 ± 10 $B \rightarrow J/\psi + X$ events occurred in the entire fiducial volume. This number is from interactions in Be only; an additional four B events are expected to have been produced in Cu, giving a total of 30 $B \rightarrow J/\psi + X$ events in the 73 event sample. An analysis of secondary interactions using Monte Carlo and minimum-bias events indicates that approximately 80 secondary-interaction events are expected to pass the vertex quality cuts in the 11.2K J/ψ sample, with approximately 33 also passing the multiplicity cut [47]. This number added to the estimated number of B events (30) and false vertex reconstruction (4) gives a total of 67 events, consistent with the 73 ± 9 events found. A determination of the beauty hadroproduction cross-section using the gap signal is presented in Chapter 8.

An event display of one of the gap events is shown in Figs. 6.7 and 6.8. Only SSD tracks with a PWC link are shown. This event is of particular interest in that, in addition to the secondary J/ψ vertex coming from the air gap, it has another vertex downstream of the primary. As shown in Fig. 6.7, the event is extremely clean in the x-z view, with almost all of the SSD hits being associated with SSD-PWC linked tracks. There is, however, a group of hits in the central region that form a SSD segment that has no PWC link. This segment is associated with the primary vertex. The y-z view is somewhat noisy, but the hits not used

by the SSD-PWC linked tracks are not consistent with any additional segments. All three of the vertices in this event are well separated and occur at the same z positions in each view, and the primary vertex has a beam track pointing to it in each view (see Fig. 6.8).

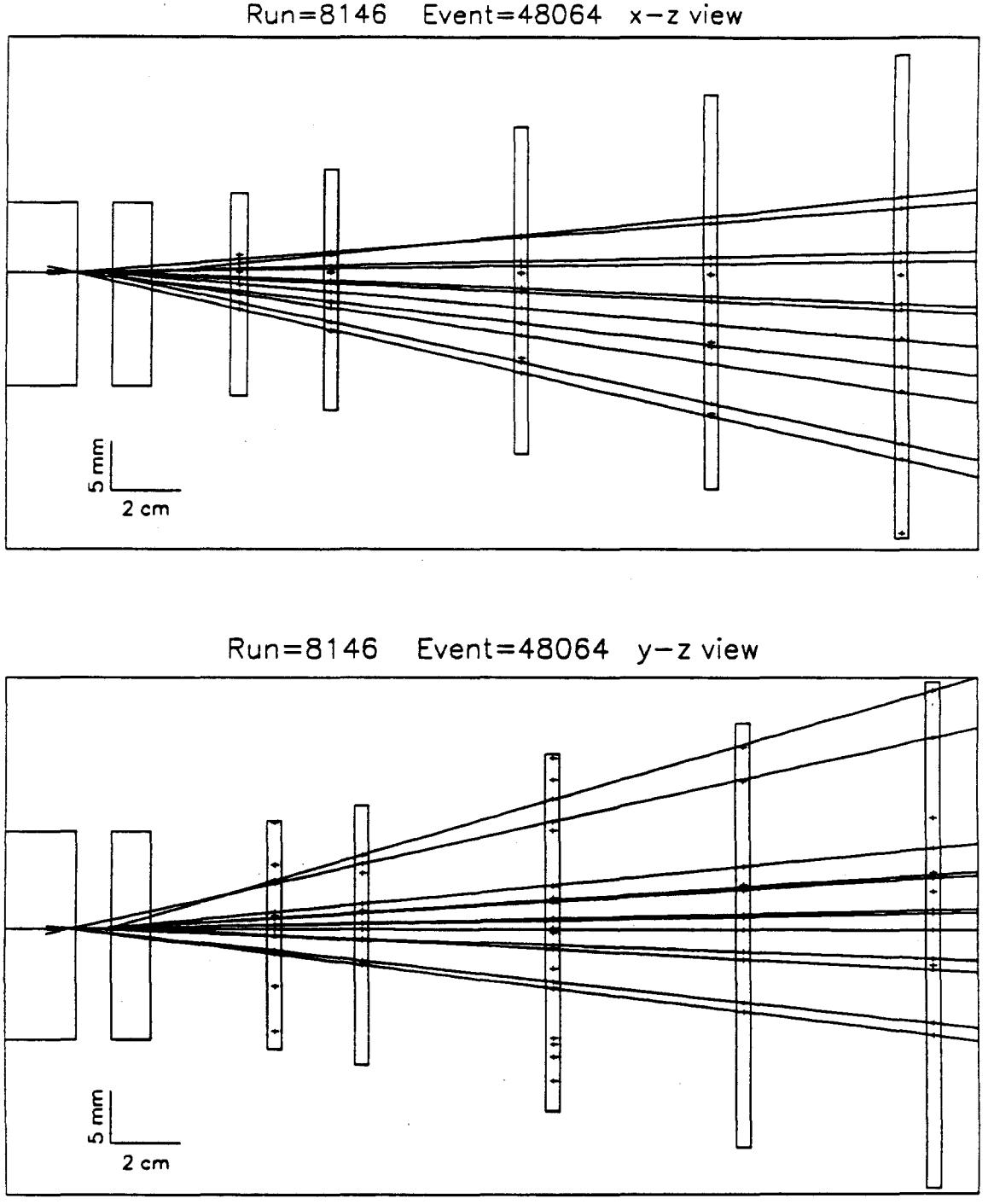

Figure 6.7. Event display of the J/ψ gap event having three vertices.

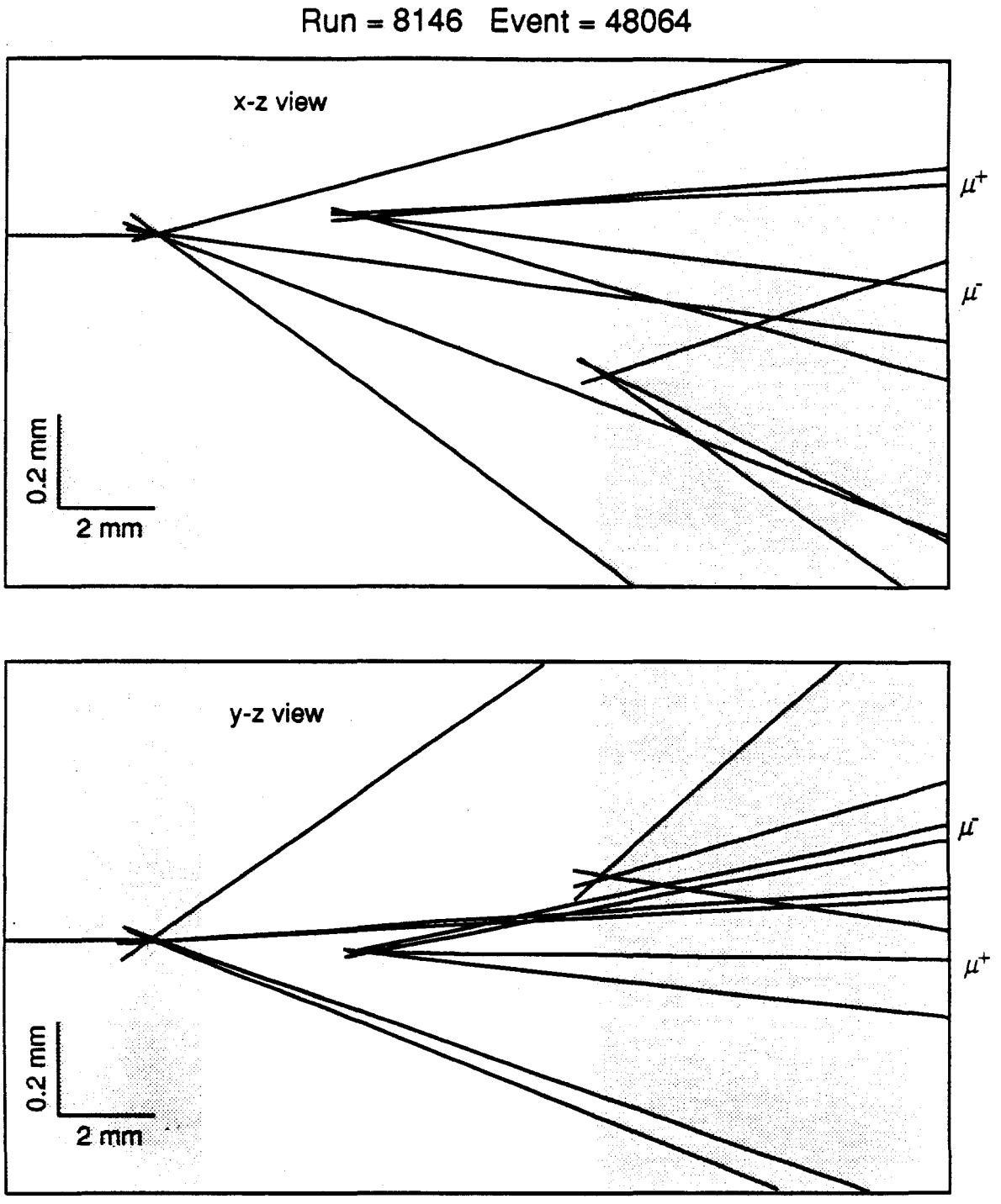

Figure 6.8. Enlargement of the vertex region for the three-vertex event shown in Fig. 6.7. The shaded area represents target material. The J/ψ in this event comes from the vertex in the air-gap region.

CHAPTER 7

EXCLUSIVE B DECAYS WITH J/ψ IN THE FINAL STATE

The decay modes $B \rightarrow J/\psi + K$ and $B \rightarrow J/\psi + K^*$ have significant channels that contain only charged particles in the final state, allowing full reconstruction of the mass and momentum of the B. Together with the decay length given by the vertex reconstruction, these quantities specify the lifetime of the decaying particle. The sample of secondary-vertex J/ψs was searched for these decay modes.

7.1 Exclusive $B^{\pm} \rightarrow J/\psi + K^{\pm}$ decay reconstruction

Events with three-prong secondaries (2 muons plus another track) from the sample of 73 secondary-vertex J/ψ events were selected as candidate $B^{\pm} \rightarrow J/\psi + K^{\pm}$ decays. Since there was no downstream hadron identification in this experiment, the non-muon track was assumed to be a kaon. Since the track density is high for fixed-target collisions at these energies, tracks from the underlying event can often be coincidentally associated with the secondary vertex. In order to reduce this background from the underlying event, the p_T (with respect to the beam axis) of the assumed kaon was required to be greater than 0.5 GeV/c. Figure 7.1 shows the kaon's p_T distribution from accepted Monte Carlo $B^{\pm} \rightarrow J/\psi + K^{\pm}$ events. The p_T distribution for charged tracks in direct J/ψ events (from real data) is shown in Fig. 7.2. As can be seen from these distributions, the cut on $p_T > 0.5$ GeV/c reduces the background considerably (61% rejection), while keeping 95% of the Monte Carlo B events. In addition to this cut, the high track density is taken into account by allowing events with 4-prong secondary vertices (2 muons plus 2 additional tracks) into the selection. These events were analyzed under the hypothesis of 3-prong B decays with an additional spurious

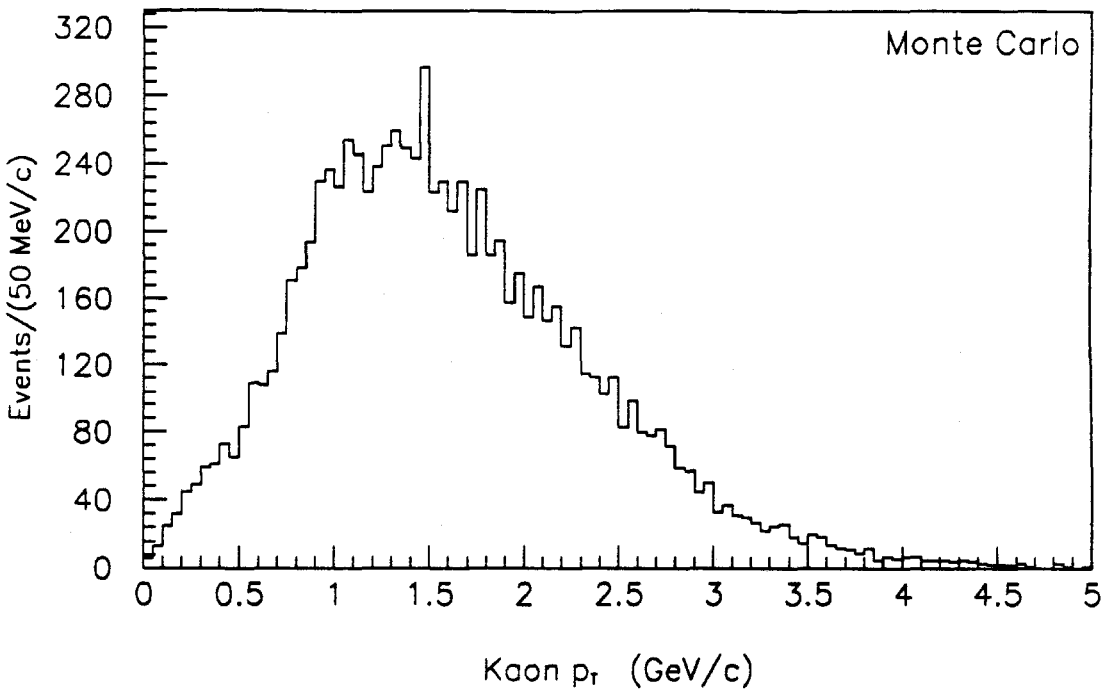

Figure 7.1. Decay kaon transverse momentum from detector accepted Monte Carlo $B \rightarrow J/\psi + K$ events.

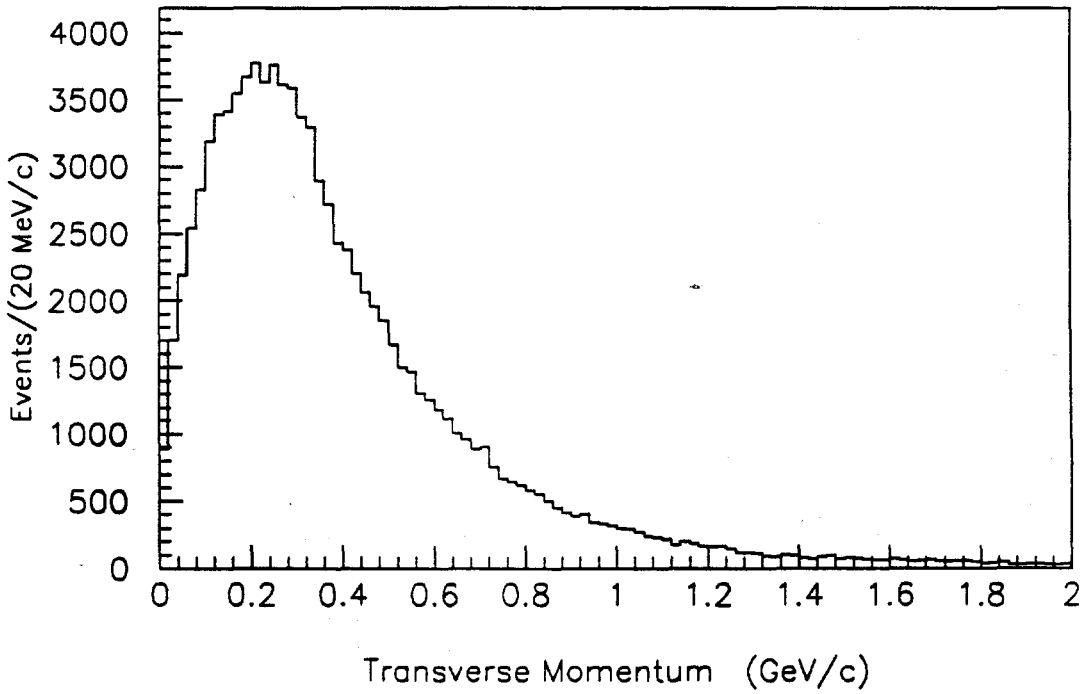

Figure 7.2. Charged track transverse momentum in real events (PSI sample).

track each. It should be noted that none of the 4-prong secondary vertices out of the 73 event sample had both secondary hadrons survive the p_T cut. The 4-prong events that had one track passing the p_T cut were vertex refit without the other track. For both the 3- and 4-prong vertices, the candidate kaon's momentum vector was added to that of the J/ψ to form a candidate B momentum vector. This vector was projected back from the secondary to the primary vertex, and a transverse impact parameter (δ_v) was calculated (see Fig. 7.3).

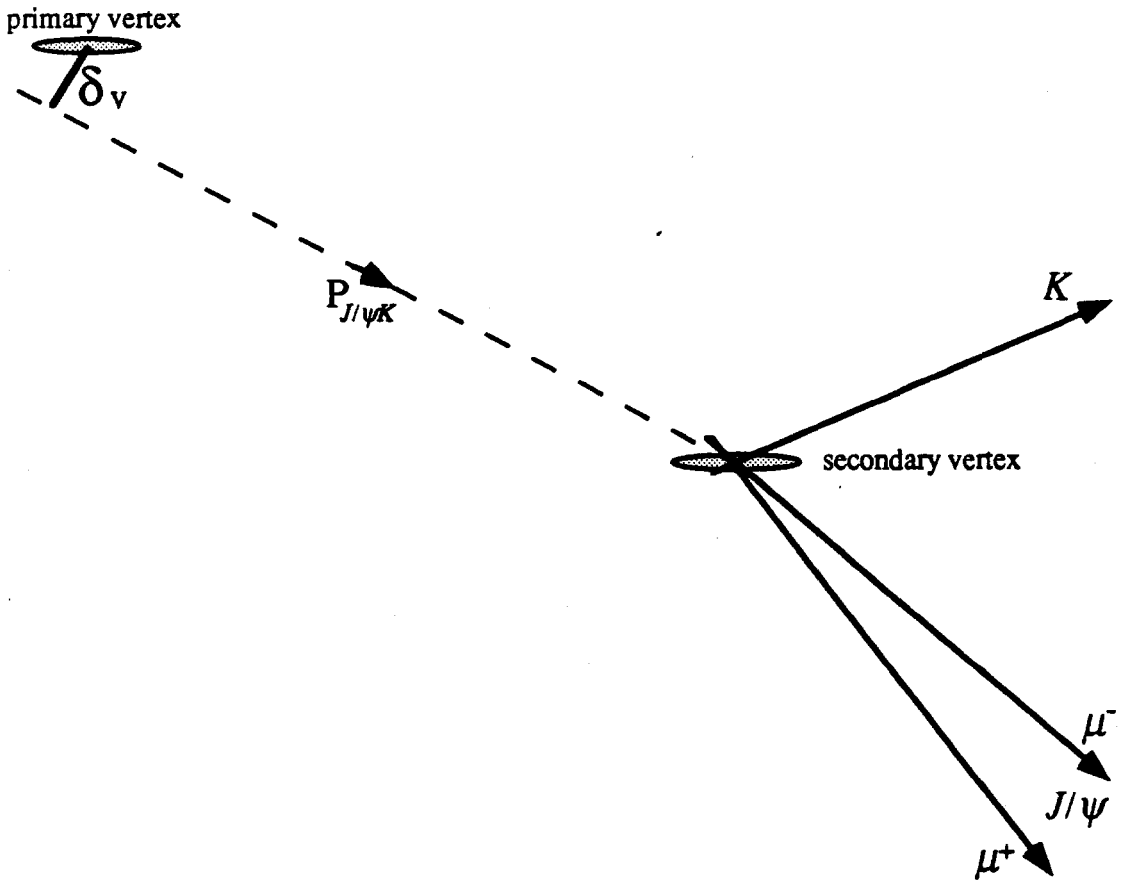

Figure 7.3. Schematic of B decay showing the secondary-vertex momentum vector's impact parameter with respect to the primary vertex (δ_v).

The distribution of the δ_v impact parameter for Monte Carlo events is shown in fig. 7.4. The width of the distribution is due to the measured momentum being smeared. Based on the Monte Carlo distribution, an event was considered a *B* candidate if δ_v was less than 80 microns.

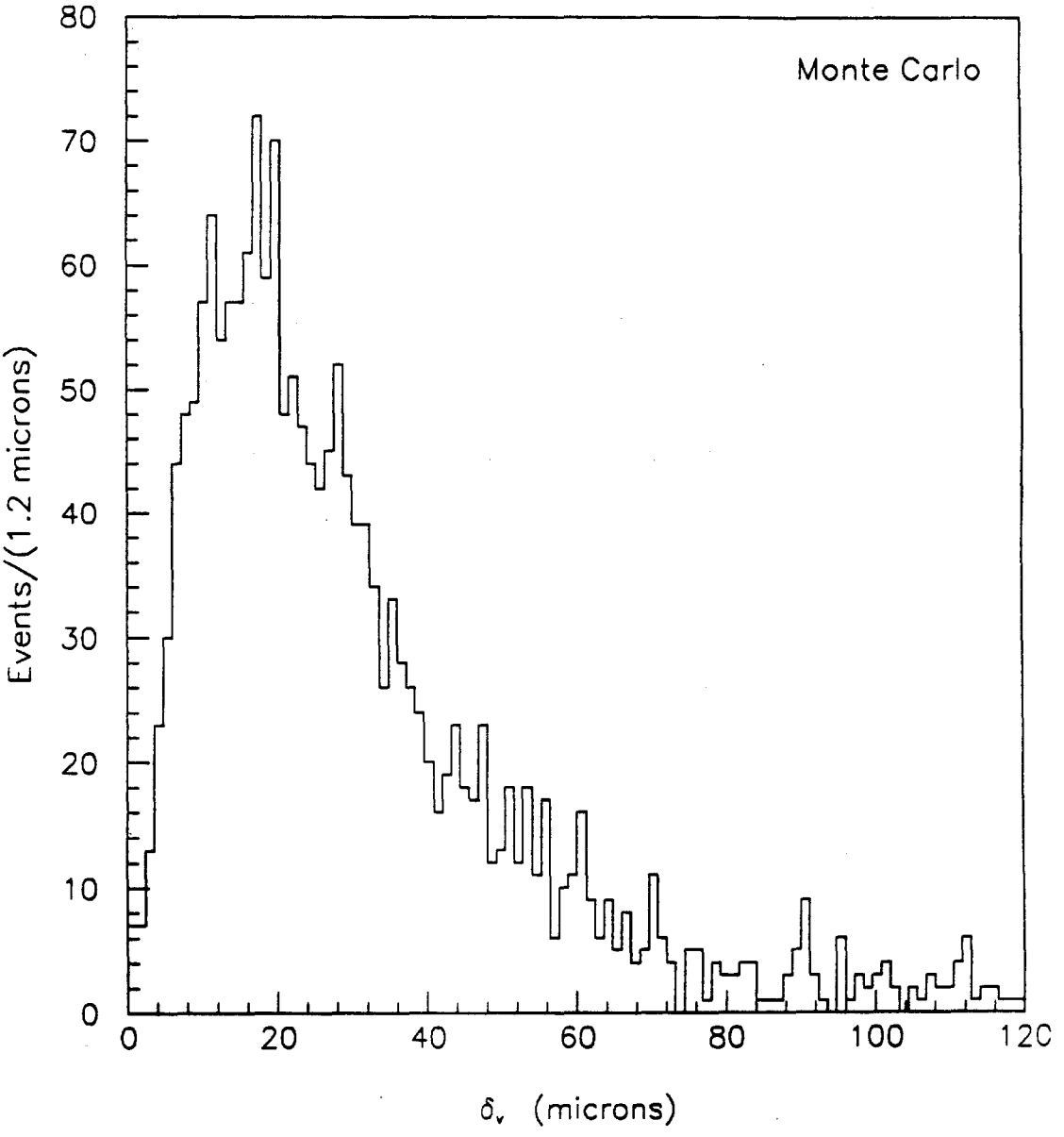

Figure 7.4. Reconstructed impact parameter of *B* momentum vector w.r.t. primary vertex (δ_v) for Monte Carlo $B^{\pm} \rightarrow J/\psi + K^{\pm}$ events

Figure 7.5 shows the reconstructed $J/\psi K^{\pm}$ invariant-mass distribution obtained by using the described method and cuts on Monte Carlo events. The distribution peaks at the PDG value of 5.28 GeV/c^2 [48] and has a standard deviation of 30 MeV/c^2.

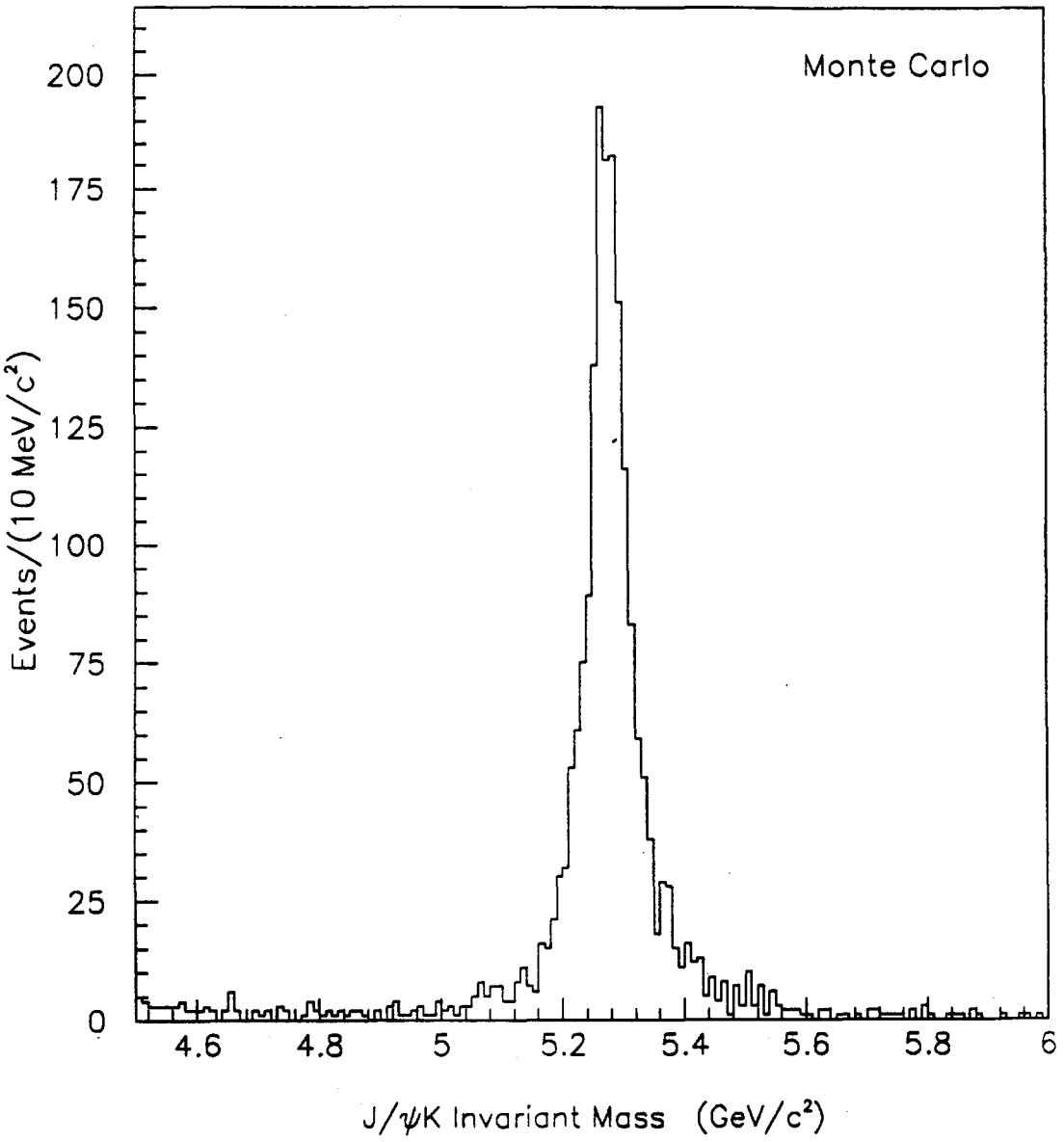

Figure 7.5. Reconstructed $J/\psi K^{\pm}$ invariant-mass distribution for Monte Carlo events

Four events from the secondary vertex J/ψ data sample survived the cuts. Their invariant-mass distribution is shown in Fig. 7.6 Two events fall in the expected B-mass region, one from each of the candidate charged decay modes: $B^+ \rightarrow J/\psi + K^+$, and $B^- \rightarrow J/\psi + K^-$.

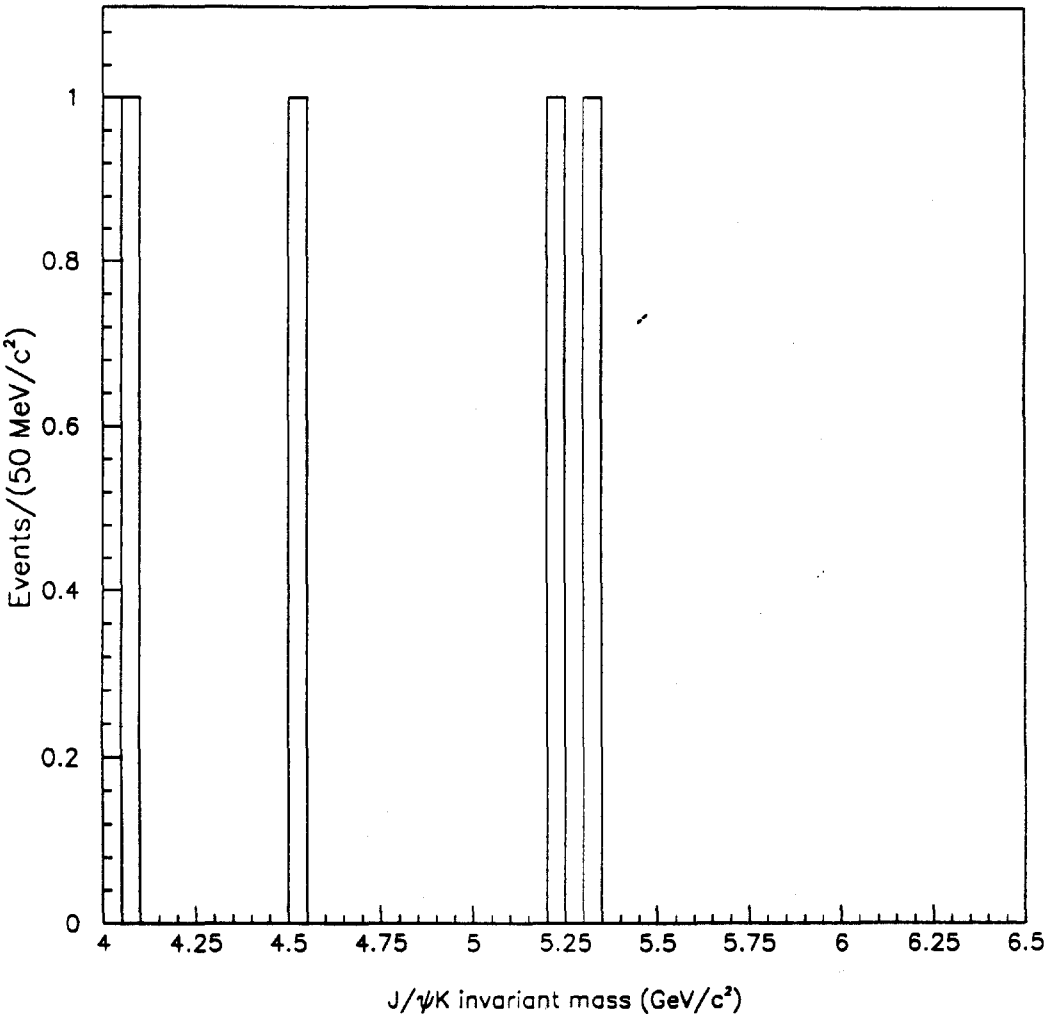

Figure 7.6 $J/\psi K^+$ invariant mass.

In order to show that the cuts used in this analysis were not selecting arbitrary events in the *B*-mass region, a background simulation using J/ψs from primary vertices was performed. $J/\psi K$ combinations from events with only one vertex were subjected to the same cuts as the combinations from secondary vertices (i.e. vertex multiplicity, hadron impact-parameter, and momentum cuts). The resulting invariant-mass distribution shown in figure 7.7 peaks near 4.1 GeV/c^2 and shows no evidence of enhancement in the *B*-mass region.

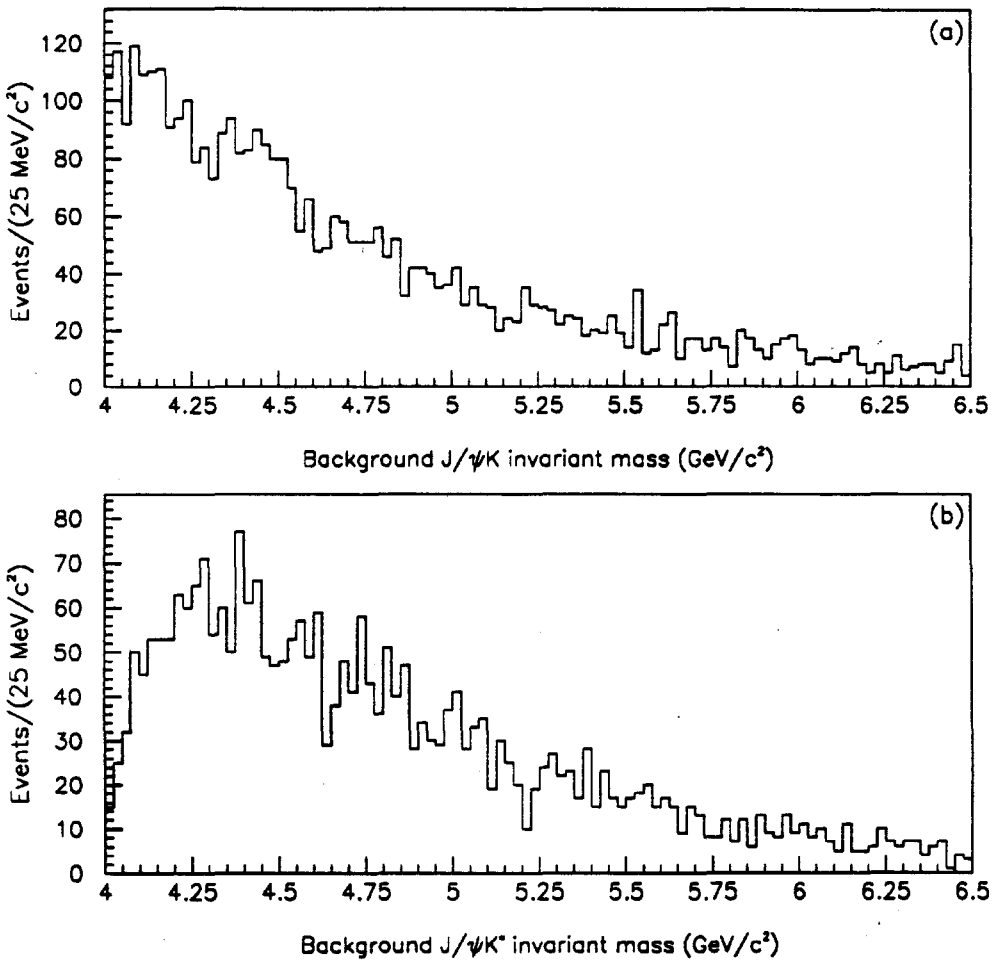

Figure 7.7. Background simulation invariant-mass distributions, (a) for $J/\psi K$ combinations from primary vertex; (b) for $J/\psi K^*$ combinations from primary vertex.

7.2 Exclusive $B^0 \rightarrow J/\psi + K^{0*}$ decay mode reconstruction

The search for the exclusive decay mode $B^0 \rightarrow J/\psi + K^{0*}$ (and its charge conjugate) proceeded as follows: K^{0*}s were observed by their decay into $K^{\pm}\pi^{\mp}$pairs. Since there was no downstream hadron particle identification in this experiment, a kinematic criterion for kaon identification was used to reduce combinations. As a result of the Lorentz boost on particles of unequal mass the kaon from a K^{0*} decay will always receive a momentum of at least a half of that of the pion. Therefore, to calculate the mass of a pair of tracks, the kaon mass was assigned to one track and the pion to the other (and visa versa), and the combination was accepted if the track assigned the kaon mass had a momentum greater than half of the other track. The invariant-mass distribution for zero-net-charge combinations of charged track pairs meeting this criteria is shown in Figure. 7.8. A K^{0*} peak is observed at the PDG mass value of 897 MeV/c^2 [48].

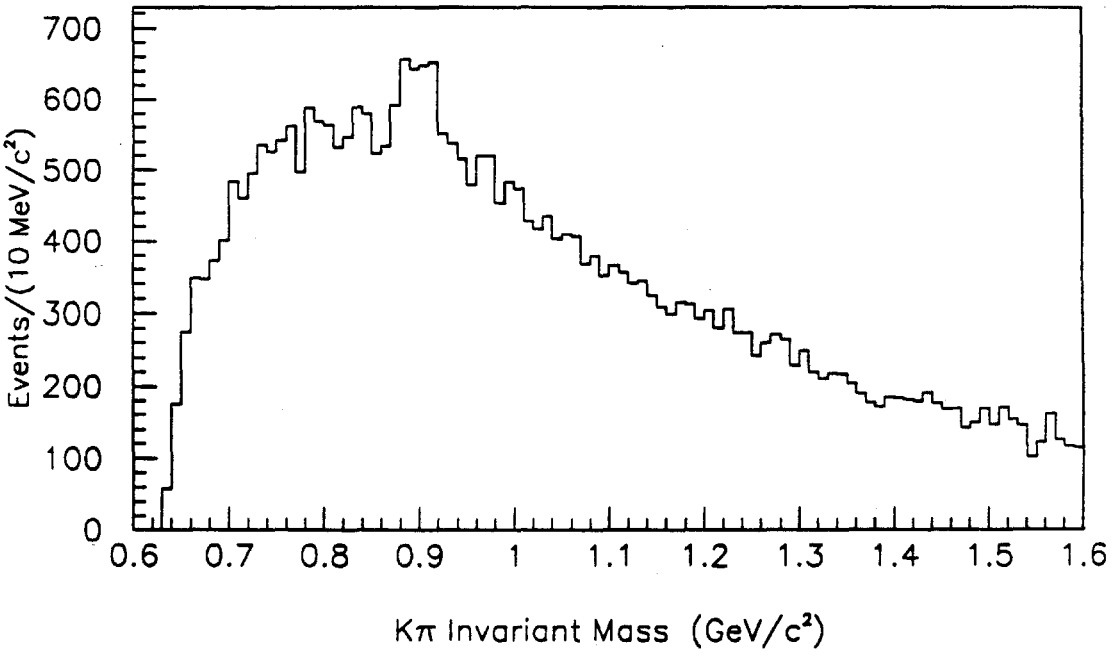

Figure 7.8. $K^{\pm}\pi^{\mp}$ invariant mass distribution.

Charged track pairs from 4- and 5-prong secondary vertices then selected in the observed K^{0*} mass region and combined with the J/ψ in the same manner as in the charged-kaon analysis. Only $K^{\pm}\pi^{\mp}$ pairs having resultant p_T greater than 0.5 GeV/c with respect to the beam axis were kept, and the candidate B momentum was required to point back to the primary vertex to within 100 μm (this cutoff is larger than the single kaon case, since there is more smearing due the additional track involved in the measurement). Five events passed these cuts, three of which have reconstructed masses in the expected B-signal range (see Fig. 7.9). The secondary vertex for one of the events in the B-mass range occurs in a region where no target material is present.

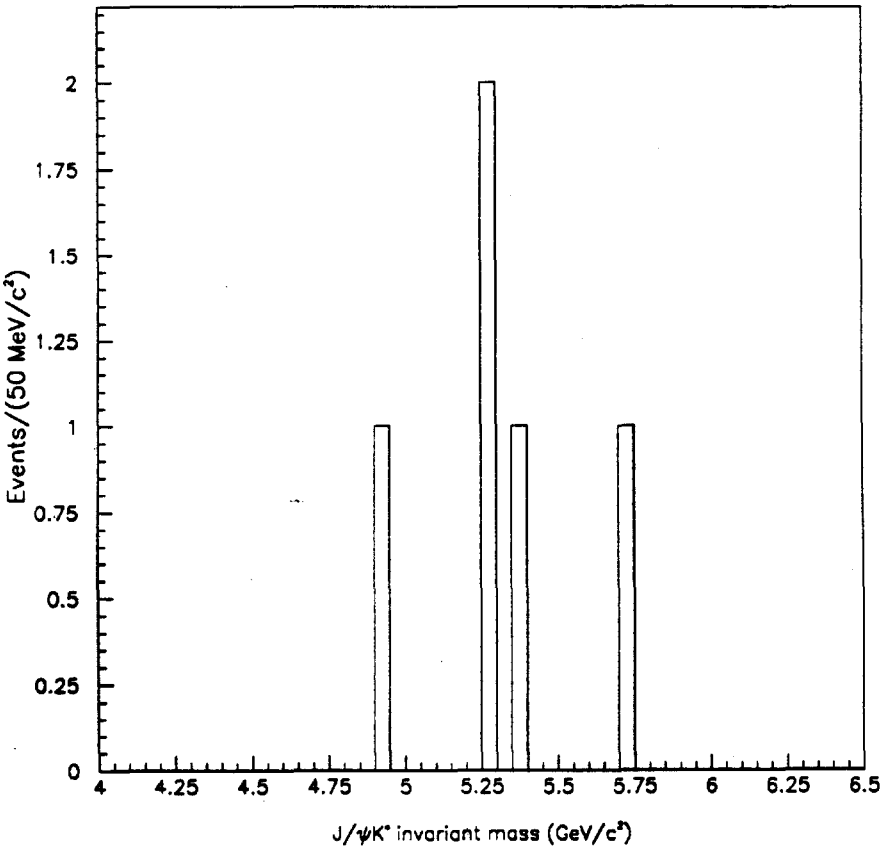

Figure. 7.9. $J/\psi K^{0*}$ invariant mass.

7.3 Event characteristics

The combined $J/\psi K^{\pm}$ and $J/\psi K^{0*}$ invariant-mass distribution is shown in Fig. 7.10 There is a clear excess of events near the nominal *B*-meson mass. A background analysis using primary vertex events subject to the same cuts as the *B* candidate sample shows no evidence for arbitrary enhancement in the *B*-mass region due to the imposed cuts (see Fig. 7.7).

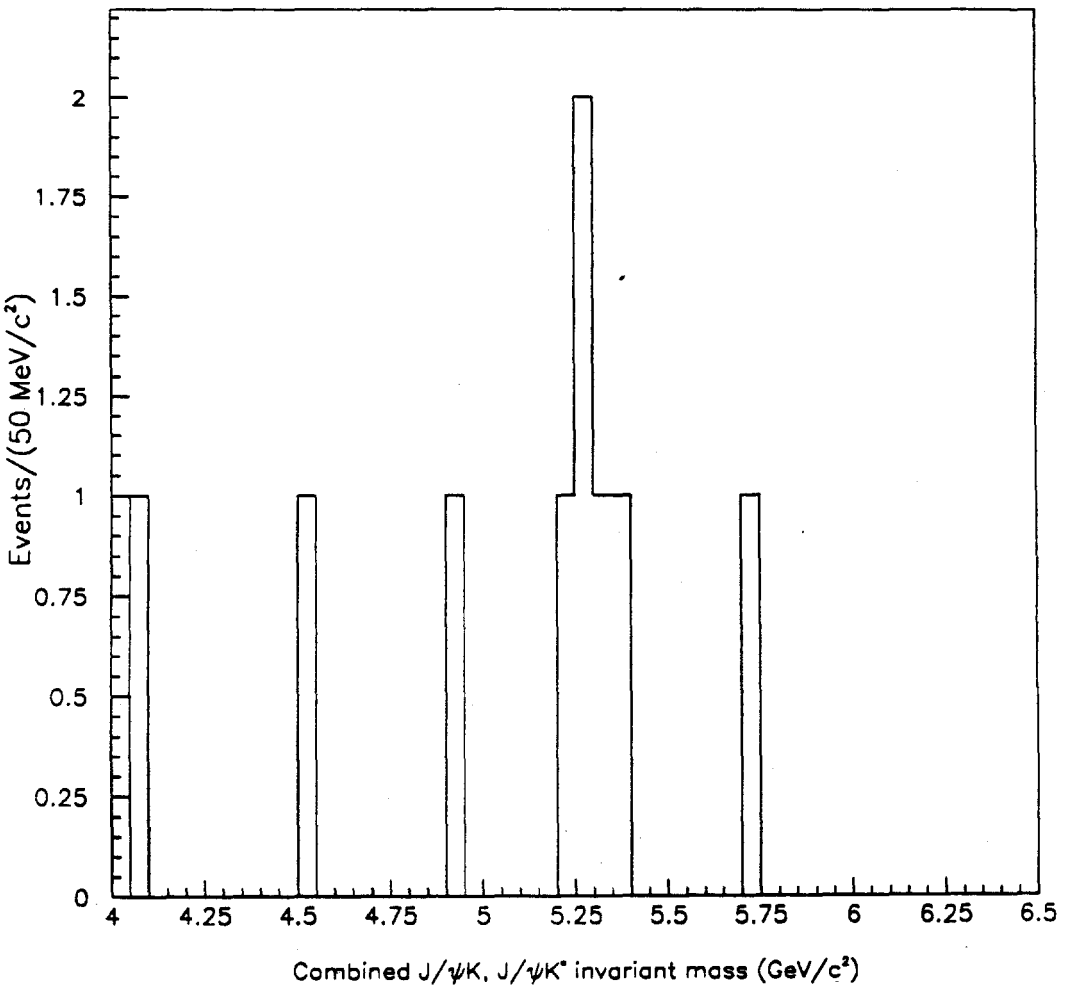

Figure 7.10 Combined $J/\psi K^{\pm}$, $J/\psi K^{0*}$ invariant mass.

The event characteristics, including the decay particle lifetimes, for the five *B*-decay candidates are shown in Table 7.1. The lifetimes for these events are consistent with the LEP measured mean *B* lifetime of 1.3 ps [11].

Table 7.1 *B*-candidate event characteristics

Postulated decay mode	B-candidate mass (GeV/c^2)	B-candidate momentum (GeV/c)	Decay length (cm)	Lifetime (ps)
$B^+ \rightarrow J/\psi + K^+$	5.31	281	2.91	1.8
$B^- \rightarrow J/\psi + K^-$	5.24	163	0.49	0.5
$\overline{B}^0 \rightarrow J/\psi + \overline{K}^{0*}$	5.36	287	0.41	0.3
$B^0 \rightarrow J/\psi + K^{0*}$	5.29	210	0.51	0.4
$\overline{B}^0 \rightarrow J/\psi + \overline{K}^{0*}$	5.25	198	1.49	1.3

CHAPTER 8

BEAUTY HADROPRODUCTION CROSS SECTION

A determination of the beauty quark hadroproduction cross section, using the 10 events in which there is a secondary vertex J/ψ occurring in an air gap region, is presented in this chapter. It was demonstrated in Chapter 6 that the background to this signal is understood and is equal to 1 event; giving a signal of 9 ± 3 B events. The exclusive decay reconstructions presented in the previous chapter are too few in number to facilitate a statistically significant cross-section determination. They do, however, show that the selection process and reconstruction programs are finding B decays.

8.1 Use of J/ψ as normalization

A cross section can be calculated from the following equation:

$$\sigma = \frac{N}{Br \cdot L \cdot \varepsilon_L \cdot \varepsilon_t \cdot \varepsilon_r \cdot acc}, \tag{8.1}$$

where: N is the number of observed events, Br is the branching ratio, L is the luminosity, ε_L is a luminosity correction factor, ε_t is a trigger efficiency correction, ε_r is the off-line reconstruction efficiency, and acc is the detector acceptance. The luminosity correction factor includes corrections due to dead-time, muon halo rejection, and "clean" interaction and beam particle requirements. With "clean" meaning no other interactions within 3 beam buckets of the event, and no other beam particle occurring within 20 ns of the event. The trigger efficiency includes corrections for the pretrigger counter efficiencies and dimuon trigger processor efficiency. The values for these corrections are discussed elsewhere [23, 42].

At this stage in the general E672 analysis, only preliminary results are available for the

luminosity and its correction. Because of this, the beauty cross-section will be determined using the observed number of J/ψs and the J/ψ cross-section as previously measured by E672 [23]. This is done by taking the ratio of the cross-sections as determined by Equation 8.1:

$$\frac{\sigma_{b\bar{b}}}{\sigma_{\psi}} = \frac{N_{b\bar{b}} \cdot Br_{\psi} \cdot L \cdot \varepsilon_L^{\psi} \cdot \varepsilon_t^{\psi} \cdot \varepsilon_\tau^{\psi} \cdot acc_{\psi}}{N_{\psi}^{'} \cdot Br_{b\bar{b}} \cdot L \cdot \varepsilon_L^{b\bar{b}} \cdot \varepsilon_t^{b\bar{b}} \cdot \varepsilon_\tau^{b\bar{b}} \cdot acc_{b\bar{b}}} \tag{8.2}$$

The number of J/ψs must be corrected for atomic number (A) dependence effects, since B production is expected to go like A^1, while we have measured that J/ψ production is proportional to $A^{0.9}$ [49]. Since the Bs and J/ψs were observed in the same data set, the luminosity, and the luminosity and trigger corrections cancel in Equation 8.2, giving the expression for the beauty cross-section:

$$\sigma_{b\bar{b}} = \frac{N_{b\bar{b}} \cdot \sigma_{\psi} \cdot Br_{\psi} \cdot \varepsilon_\tau^{\psi} \cdot acc_{\psi}}{N_{\psi}^{'} \cdot Br_{b\bar{b}} \cdot \varepsilon_\tau^{b\bar{b}} \cdot acc_{b\bar{b}}} \tag{8.3}$$

The Bs and direct J/ψs used for the cross-section determination were restricted to having had been produced in the Be target material, and they had to have an x_F greater than 0.1. All 10 of the events with a secondary-vertex J/ψ occurring in the air gaps meet these criteria. There are 9264 ± 105 reconstructed J/ψs meeting these criteria. The A-dependence corrected number of J/ψs from Be (A = 9) is: $N_{\psi}^{'} = N_{\psi} \cdot A^{0.1} = 11540 \pm 130$. A value for $\sigma_{\psi} \cdot Br_{\psi \to \mu\mu} = (7.6 \pm 1.5)$ nb/nucleon ($x_F > 0.1$), as measured by E672 previously [23,49], was used for this beauty cross-section determination.

8.2 Acceptances and efficiencies

The acceptances and reconstruction efficiencies were determined from Monte Carlo simulations as described in Chapter 5. For an event to be considered accepted, it must result

in two muons, both of which make it through the active area of the muon system. The muon acceptances in the forward direction ($x_F > 0.1$) are 43% and 33% for directly produced J/ψs and $B \rightarrow J/\psi + X$ events, respectively. A sample of about 40 thousand Monte Carlo $B \rightarrow J/\psi + X$ events was used to determine the reconstruction efficiency. The sample had an almost equal amount of 2, 3, 4, and 5 prong decay vertex events. The total reconstruction efficiency for these events was determined to be 36%, with 35% of these events occurring in the air gap giving a total effective efficiency for finding a $B \rightarrow J/\psi + X$ gap event of : (0.36)(0.35) = 13%. The breakdown of the factors leading to the total reconstruction efficiency is as follows:

(i) J/ψ reconstruction: the linking of a muon track through the entire apparatus has an efficiency of 86%, leading to an efficiency for reconstructing both muons of: (.86)(.86) = 74% . A reconstructed invariant mass cut of 2.85 $GeV/c^2 < M_{\mu\mu} <$ 3.35 GeV/c^2 kills 7% of the J/ψs. The total J/ψ reconstruction efficiency is therefore: (.86)(.86)(.93) = 69%. It should be noted that this efficiency is for J/ψs coming from B decays, the efficiency for prompt J/ψs is 80%.

(ii) The J/ψ vertex fit, described in Appendix A, is 94% efficient.

(iii) Primary vertex reconstruction: the reconstruction of the primary vertex, and the requirement of at least three tracks fully linked to it is 84% efficient. The requirement of a beam track pointing to the primary kills 24% of the events, giving a total primary vertex reconstruction efficiency of: (.84)(.76) = 64%.

(iv) The vertex separation and quality cuts, described in Chapter 6, have an efficiency of 87%

These factors lead to a total reconstruction efficiency for $B \rightarrow J/\psi + X$ events of: (.69)(.94)(.64)(.87) = 36%. The total reconstruction efficiency for directly produced J/ψs is 75%, it consists of factors i (80%), an ii (94%) listed above.

8.3 Cross-section calculation

As mentioned in chapter 5, E672's signal of secondary vertex J/ψs can include decays of all the b-hadron species, including baryons. Consequently, and since b-quarks are always produced with their antiquark in pairs, we are measuring the $b\bar{b}$ hadroproduction cross section The branching ratio appropriate for the signal of secondary-vertex J/ψs is the $b \rightarrow J/\psi+X$ branching ratio of $(1.3 \pm 0.4)\%$ as determined by L3, which includes decays from all b-hadron species [11]. The combined branching ratio used for the cross-section determination ($Br_{b\bar{b}}$) must also include the $J/\psi \rightarrow \mu\mu$ branching ratio of $(5.97 \pm 0.25)\%$ [43], and a factor of 2 since both the b-hadron and the $\bar{b}$-hadron can decay into J/ψ; $Br_{b\bar{b}\rightarrow\psi\rightarrow\mu\mu}$ is therefore equal to: (2)(.0597)(.013) = $(1.6 \pm 0.5)\text{x}10^{-3}$.

To summarize, the values of the parameters needed in the beauty cross-section determination using the background subtracted signal of 9 ± 3 secondary-vertex J/ψs occurring in the air gap regions are:

$$N_{b\bar{b}} = 9 \pm 3$$

$$N'_{\psi} = 11540 \pm 130$$

$$\sigma_{\psi} \cdot Br_{\psi\rightarrow\mu\mu} = (7.6 \pm 1.5) \text{ nb/nucleon}$$

$$\varepsilon_r^{\psi} = 75\%$$

$$acc_{\psi} = 43\%$$

$$\varepsilon_r^{b\bar{b}} = 13\%$$

$$acc_{b\bar{b}} = 33\%$$

$$Br_{b\bar{b}\rightarrow\psi\rightarrow\mu\mu} = (1.6 \pm 0.5)\text{x}10^{-3}$$

Using these values, with Equation 8.3, a beauty hadroproduction (π^--A collisions at 530 *GeV/c*) cross-section in the forward direction of:

$$\sigma_{b\bar{b}} = (28 \pm 9 \pm 8) \text{ nb/nucleon} \quad (x_F > 0.1),$$

is obtained (where the first error is statistical, and the second is systematic).

The main sources of systematic error are due to uncertainties in normalization (18%), branching ratios (14%), *B* production x_F distribution (12%), and reconstruction efficiencies (10%). The uncertainty due to the *B* production and decay characteristics, were determined by varying the production x_F distribution and the *B* lifetime in Monte Carlo events as mentioned in Chapter 5. The reconstruction efficiency uncertainty was also determined from Monte Carlo; effects due to variations in detector noise, detector efficiencies, and number of tracks in the underlying event were studied. The normalization uncertainty is due to the errors on the J/ψ cross section. A measurement of this value by E672, with much higher statistics, is now underway [42]. This measurement will reduce the normalization uncertainty to the 10% level.

CHAPTER 9

CONCLUSIONS

9.1 Summary of results

In π^--A collisions at 530 *GeV/c*, we have found candidates for *B*-meson decays in modes involving the J/ψ. In seventy-three events, a J/ψ was observed to emerge from a low-multiplicity secondary vertex, a characteristic of *B*-hadron decay. While there is a background to this signal from secondary interactions, in ten of these events the J/ψ vertex occurs in air gap regions where these interactions are highly unlikely. The background to this signal is determined to be 1 event, leaving 9 ± 3 beauty events. A hadroproduction cross-section in the forward direction of:

$$\sigma_{b\bar{b}} = (28 \pm 9 \pm 8) \text{ nb/nucleon} \quad (x_F > 0.1),$$

has been determined from these events. Extrapolating the number of gap events, using Monte Carlo analysis, we estimate 26 ± 10 of the 73 events in the entire fiducial volume are beauty decays.

Five exclusive *B* decays; three in the $B^0 \rightarrow J/\psi + K^{0*}$ mode, and two in the $B^{\pm} \rightarrow J/\psi + K^{\pm}$ mode, were fully reconstructed. While small in number, these events provide a clean signal in the invariant-mass distribution.

9.2 Comparison to theory and other experiments

In order to compare the beauty cross-section determination of the previous section to theory and other experiments, it must be extrapolated from the forward direction ($x_F > 0.1$) to all x_F regions. Due to the discrepancies (see Chapter 5) in the *B* production x_F

distribution between those measured (with very large uncertainties) by E653 and Berger's theoretical predictions, this extrapolation is extremely uncertain. The discrepancy is demonstrated in Figure 9.1, in which both distributions are plotted (normalized to the same number of events). The extrapolation from $x_F > 0.1$ to all x_F results in multiplicative factors of 1.49 and 1.98 using the E653 distribution and Berger's distribution, respectively. As was done for the acceptance and reconstruction efficiency calculations, the E653 distribution will be used, and the variation of Berger's distribution from this will be accounted for in the systematic uncertainty (a 20% effect).

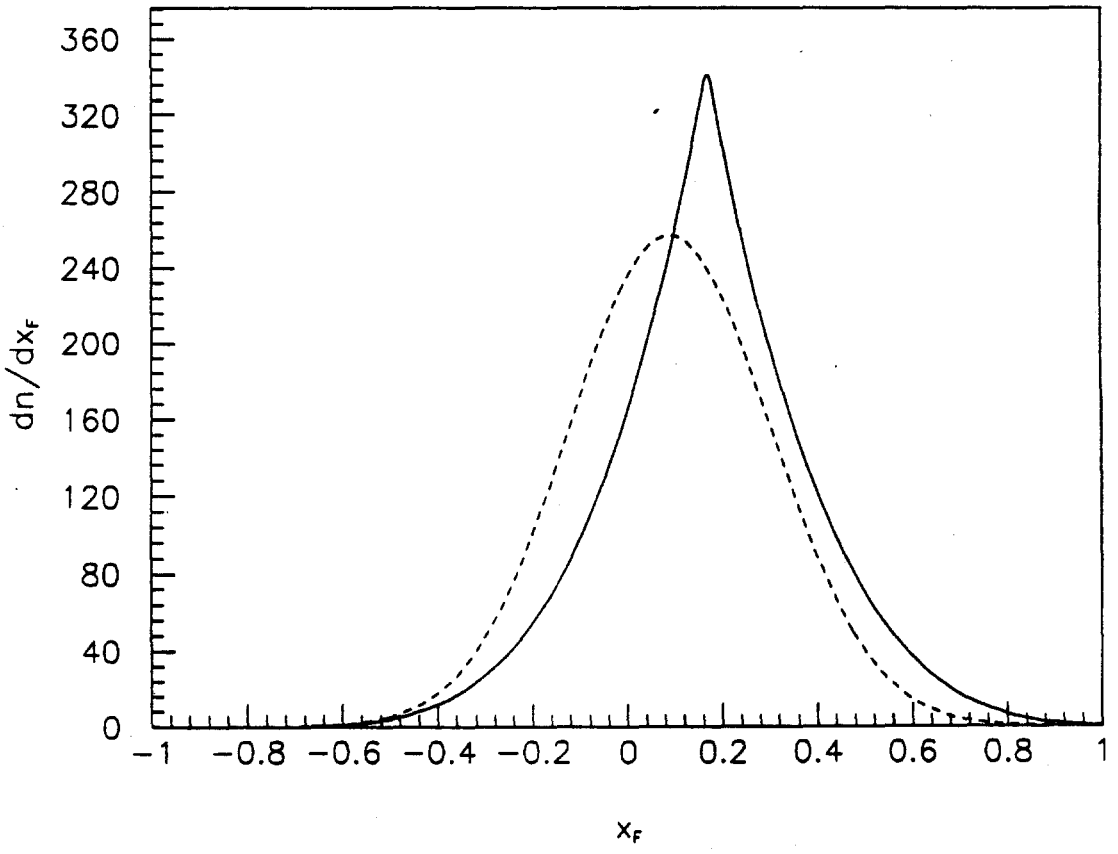

Figure 9.1 $B x_F$ distributions: solid line is from E653 fit, dashed line is theoretical predictions by Berger.

Extrapolating, a total cross-section is obtained of:

$$\sigma_{J/\psi} = (42 \pm 13\ ^{+16}_{-13})\ \text{nb/nucleon},$$

where the first uncertainty is statistical, and the second is systematic. This value seems high when compared to the value obtained by E653 of $33 \pm 11 \pm 7$ nb/nucleon [21], at a pion beam momentum of 600 *GeV/c*. Since the cross section is expected to increase with beam momentum, our point (at 530 *GeV/c*) should be slightly lower than E653's. The uncertainties on both measurements are large, however, so the measurements are not statistically inconsistent. Our total cross section measurement is also larger than Berger's prediction (see fig 9.2), but not at a significant level here either. Both our, and E653's measurements, as well as that of WA78 are shown in Figure 9.2 along with Berger's predictions. Both of the other experiment's points lie in the theoretical band.

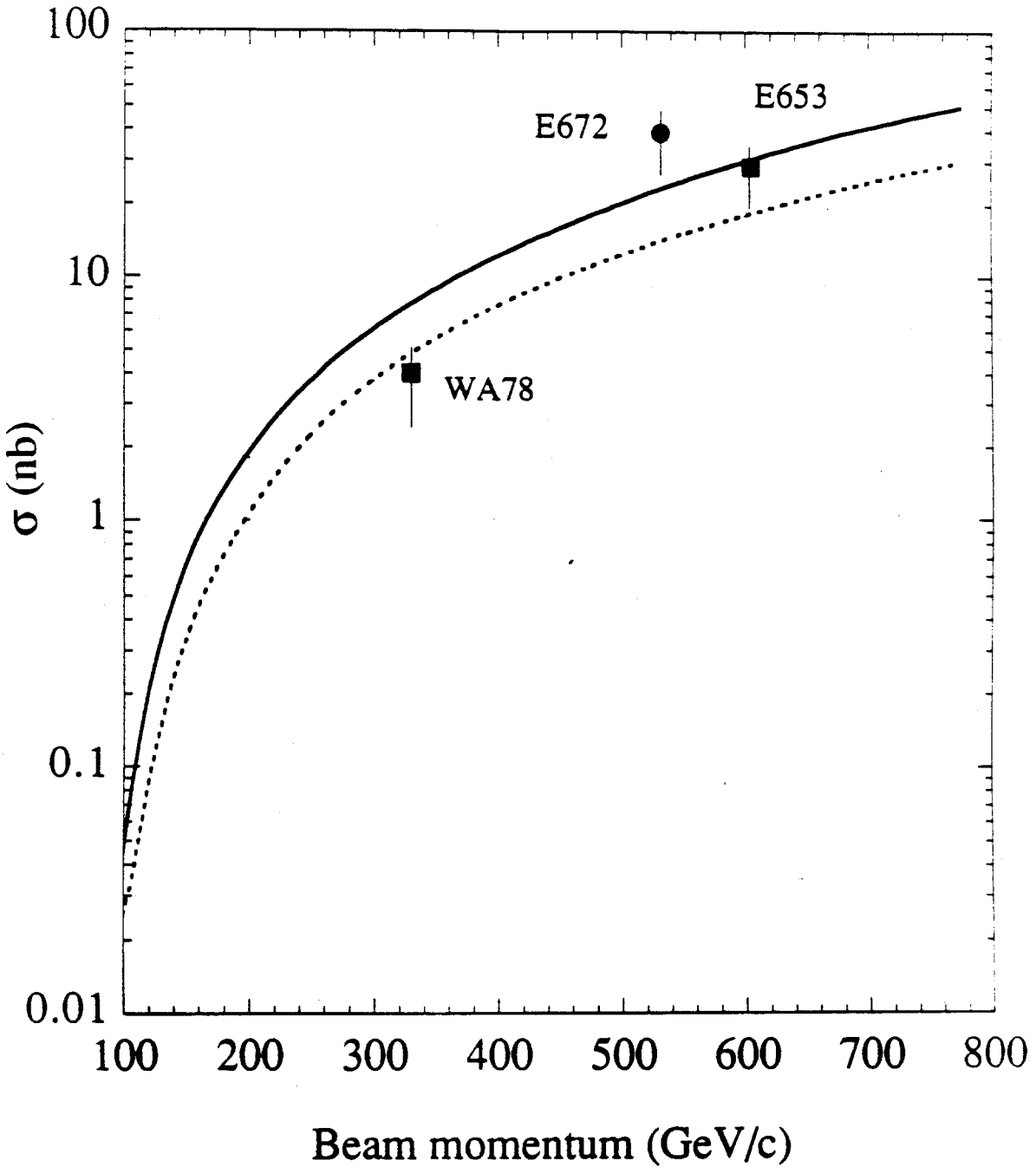

Figure 9.2. Berger's beauty cross section predictions as a function of beam momentum, along with measurements from E653, WA78, and this experiment (E672).

9.3 Conclusion

This experiment has helped show that fixed-target beauty physics is possible. A high-statistics experiment with a larger x_F acceptance could well measure the total beauty cross section with the precision needed to really test the theoretical calculations. Measurements of the production x_F and p_T distributions, as well as atomic number dependence would also be very interesting. We have also shown that exclusive decays into J/ψ can be reconstructed in a fixed-target environment. This has large implications for a CP violation experiment since the $B^0 \rightarrow J/\psi + K_s^0$ decay is considered one of the flagship events for this study. An experiment designed for this study would have to have a very large acceptance since the other B in these events has to be tagged for a CP analysis. It also remains to be seen if the rates needed for this study are accessible to a fixed target experiment.

APPENDIX

THE J/ψ VERTEX FIT

The vertex position and the momentum vector of the J/ψ is determined by a vertex fit of the muon track parameters in which the J/ψ mass is used as a constraint. Muon pairs are described by a vector of 10 parameters (p) consisting of x-z and y-z slopes and intercepts, and inverse momenta for both muons, and their error matrix (E) (see Fig. A.1),

$$\mathbf{p} = (m_{1x}, b_{1x}, m_{1y}, b_{1y}, \rho_1, m_{2x}, b_{2x}, m_{2y}, b_{2y}, \rho_2). \qquad \text{(A.1)}$$

It should be noted that these parameters are not true measurements; they are determined from the SSD-PWC-MUON fit described in Chapter 4, and are taken as virtual measurements to find an estimate of the new track parameters (q) and the J/ψ parameters [50]. A 6 parameter vector (x) is used to describe the J/ψ; it consists of the J/ψ inverse momentum, x-z and y-z slopes, and the vertex position (see Fig. A.1),

$$\mathbf{x} = (v_x, v_y, v_z, m_{\psi x}, m_{\psi y}, \rho_\psi). \qquad \text{(A.2)}$$

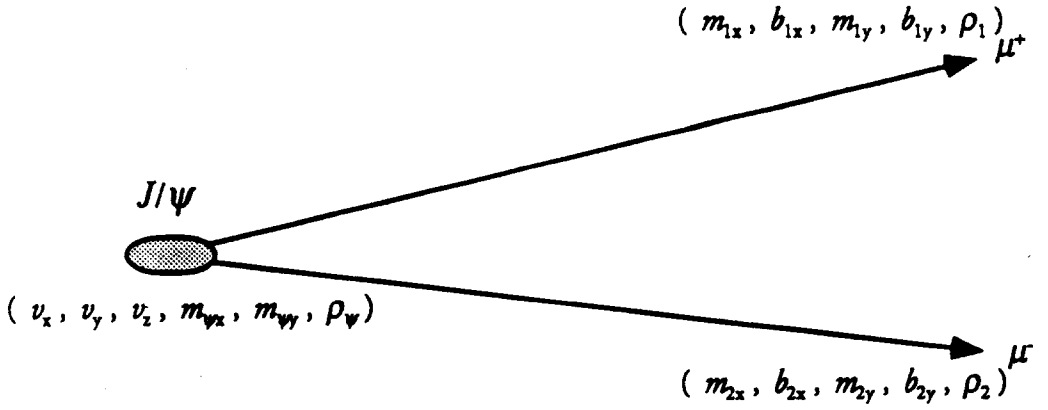

Figure A.1. Diagram of J/ψ decay into muon pairs, showing parameters used in the vertex fit.

The J/ψ and muon parameters are related by a set of 8 constraint equations

$$\frac{m_{\psi x}}{\left(m_{\psi x}^2+m_{\psi y}^2+1\right)^{1/2}\rho_\psi}=\frac{m_{1x}}{\left(m_{1x}^2+m_{1y}^2+1\right)^{1/2}\rho_1}+\frac{m_{2x}}{\left(m_{2x}^2+m_{2y}^2+1\right)^{1/2}\rho_2} \tag{A.3}$$

$$\frac{m_{\psi y}}{\left(m_{\psi x}^2+m_{\psi y}^2+1\right)^{1/2}\rho_\psi}=\frac{m_{1y}}{\left(m_{1x}^2+m_{1y}^2+1\right)^{1/2}\rho_1}+\frac{m_{2y}}{\left(m_{2x}^2+m_{2y}^2+1\right)^{1/2}\rho_2} \tag{A.4}$$

$$\frac{1}{\left(m_{\psi x}^2+m_{\psi y}^2+1\right)^{1/2}\rho_\psi}=\frac{1}{\left(m_{1x}^2+m_{1y}^2+1\right)^{1/2}\rho_1}+\frac{1}{\left(m_{2x}^2+m_{2y}^2+1\right)^{1/2}\rho_2} \tag{A.5}$$

$$\left(\frac{1}{\rho_\psi^2}+M_\psi^2\right)^{1/2}=\left(\frac{1}{\rho_1^2}+M_\mu^2\right)^{1/2}+\left(\frac{1}{\rho_1^2}+M_\mu^2\right)^{1/2} \tag{A.6}$$

$$v_x = m_{1x}v_z + b_{1x} \tag{A.7}$$

$$v_x = m_{2x}v_z + b_{2x} \tag{A.8}$$

$$v_y = m_{1y}v_z + b_{1y} \tag{A.9}$$

$$v_y = m_{2y}v_z + b_{2y}, \tag{A.10}$$

where Eqs. (A.3), (A.4), and (A.5) are momentum conservation equations in the x, y, and z directions, respectively; (A.6) is a conservation of energy equation with the J/ψ mass imposed; and Eqs. (A.7-10) are straight line equations for the muon tracks which are constrained to form a common z-vertex position in both the x-z and y-z views.

According to the Least-Squares Principle [51], the best estimates of **q** and **x** are those for which

$$\left.\begin{aligned} \chi^2 = (\mathbf{p}-\mathbf{q})^T \mathbf{E}^{-1} (\mathbf{p}-\mathbf{q}) \ \text{ is a minimum}, \\ \text{and} \quad \mathbf{c} = \mathbf{0}, \end{aligned}\right\} \tag{A.11}$$

where **c** is a vector corresponding to the eight constraint equations, Eqs. (A.3-10). These equations are solved using Lagrangian multipliers. A vector of 8 multipliers (λ) is introduced, and a new χ^2 is formed and minimized,

$$\chi^2 = (\mathbf{p}-\mathbf{q})^T \mathbf{E}^{-1} (\mathbf{p}-\mathbf{q}) + 2\lambda^T \mathbf{c}. \tag{A.12}$$

There are now 24 unknowns (10 from **q**, 6 from **x**, and 8 from λ). The χ^2 is minimized when its derivatives with respect to all 24 unknowns are zero, leading to the following set of equations,

$$\left.\begin{aligned} \nabla_q(\chi^2) = -2\mathbf{E}^{-1}(\mathbf{p}-\mathbf{q}) + 2(\mathbf{F}_q)^T \lambda = \mathbf{0}, \quad & (10 \text{ eqs.}) \\ \nabla_x(\chi^2) = 2(\mathbf{F}_x)^T \lambda = \mathbf{0}, \quad & (6 \text{ eqs.}) \\ \nabla_\lambda(\chi^2) = 2\mathbf{c} = \mathbf{0}, \quad & (8 \text{ eqs.}) \end{aligned}\right\} \tag{A.13}$$

where the matrices $\mathbf{F_q}$ and $\mathbf{F_x}$ are defined by

$$(F_q)_{ij} \equiv \frac{\partial c_i}{\partial q_j}, \qquad (F_x)_{ij} \equiv \frac{\partial c_i}{\partial x_j}. \tag{A.14}$$

The solution of the set of equations (A.13) is found iteratively as outlined in Ref. [50]. To start the iteration the virtual measurements (p) are taken as the initial values of **q**. The initial values of **x** are found by satisfying 6 of the constraint equations (A.3, A.4, A.5, A.7, A.8, and A.9). The other two constraint equations (A.6, and A.9) will, in general, not be satisfied. For the next iteration, a Taylor expansion of the constraint equations about **q** and **x** is performed. With this expansion and equations (A.13), it is possible to express all the unknowns of the (n+1)-th iteration by the quantities of the preceding (n-th) iteration [50]. The iterations are continued, with new Taylor expansions of c about the new values of q and x, until the change in χ^2 between successive steps becomes small. The **x** parameters are also checked for convergence as a criteria for continued iteration.

Only muon pairs with an invariant mass in the range 2.85 $GeV/c < M_{\mu\mu} < 3.35$ GeV/c (see Fig. 4.8) with a consistent z-vertex position (within errors) in the x-z and y-z planes are subject to the fitting procedure. Figure A.2 shows the distribution of the difference between the z-vertex position in the x-z plane and that in the y-z plane for dimuons in the above mass range from the 1990 PSI sample. These positions are considered consistent if their difference divided by the error in the difference is less than unity. The χ^2 (per degree of freedom) distribution from the fit for muon pairs passing the above cuts is shown in Fig. A.3; only candidates with a $\chi^2 < 1$ are accepted.

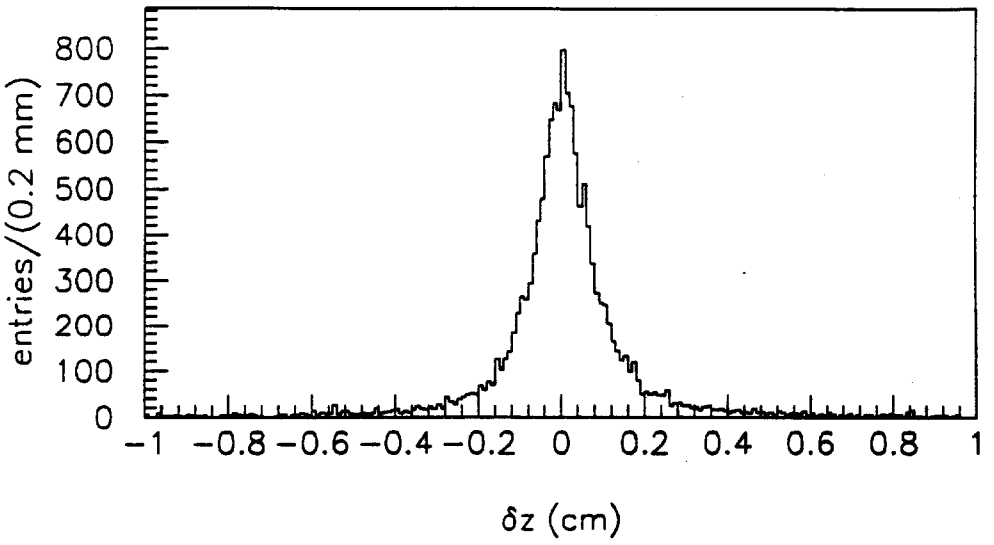

Figure A.2. Difference between dimuon vertex z-position as found in the x-z and y-z views.

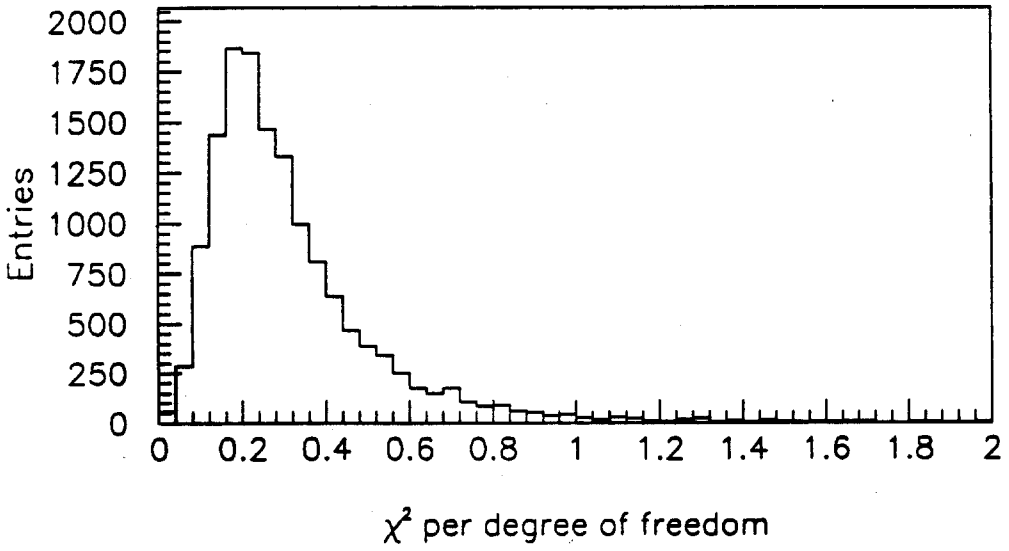

Figure A.3. χ^2 per degree of freedom distribution from J/ψ vertex fit.

The fitting procedure was tested on Monte Carlo $B \rightarrow J/\psi + X$ events as well as directly produced J/ψ Monte Carlo events. The procedure reproduced the primary vertex found in the initial vertex finding (see Chapter 4) with a 98% efficiency for direct J/ψ events. The efficiency for finding secondary J/ψ vertices was increased using this procedure by a factor of 26% over the initial vertex finding, with an increased accuracy in vertex position determination. This is demonstrated in Fig. A.4 which shows the difference between the reconstructed and generated J/ψ vertex z-position for Monte Carlo B events. The solid line is the distribution for positions determined by the J/ψ vertex fitting procedure, while the dashed is that for the initial vertex finding. The asymmetric tail in the distribution for the initial vertex finding is due to false association of tracks between the primary and secondary vertices; this tends to move the reconstructed secondary vertex position towards that of the primary. Notice that this tail is absent from the J/ψ fitted distribution. In addition to the increased accuracy in vertex position, the J/ψ momentum determination is improved by the mass constraint imposed in the fit as demonstrated in Fig. A.5.

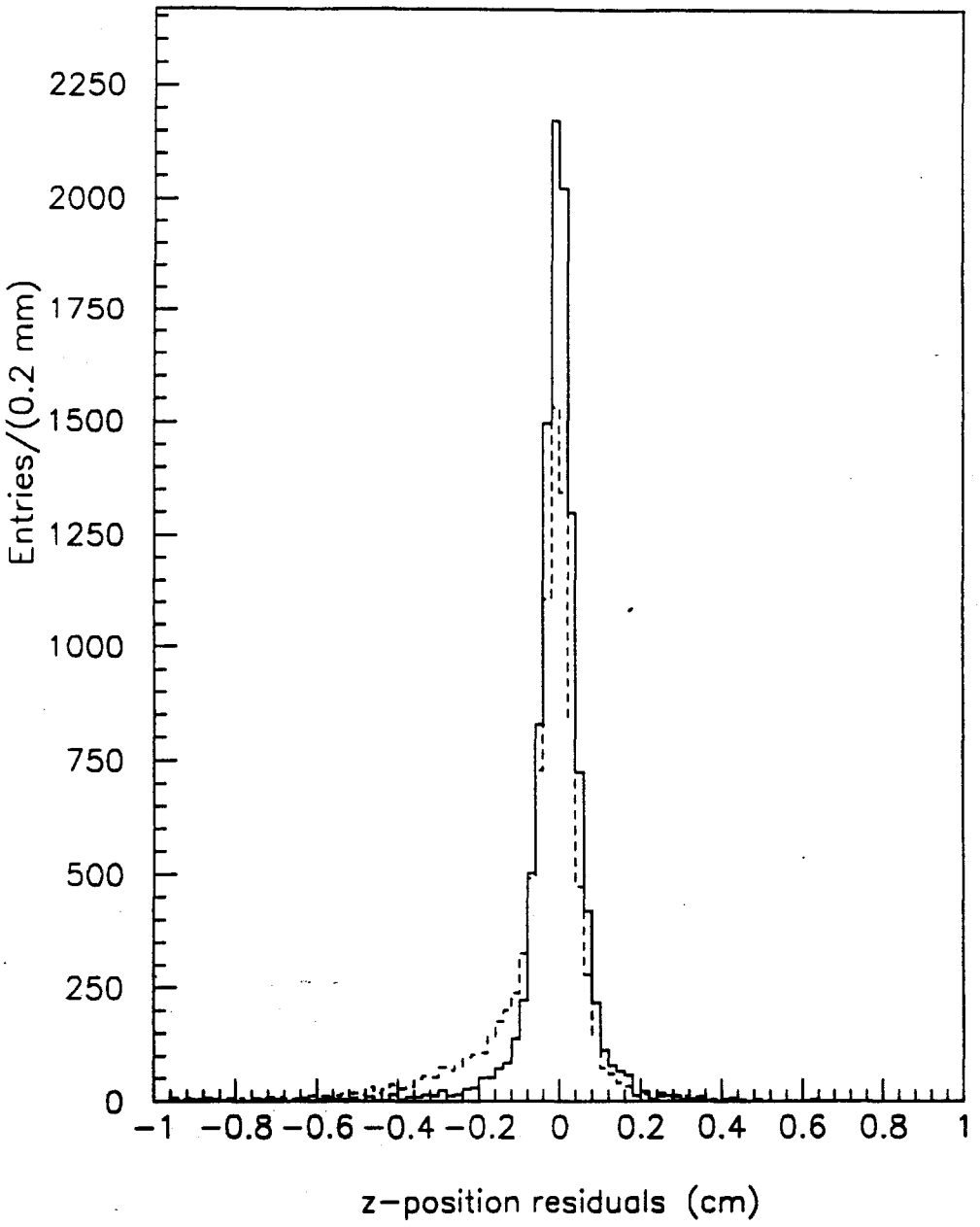

Figure A.4. Difference between reconstructed and generated J/ψ vertex positions in the z-direction for Monte Carlo B decays. The solid line is the distribution for positions determined by the J/ψ vertex fitting procedure, while the dashed is that for the initial vertex finding.

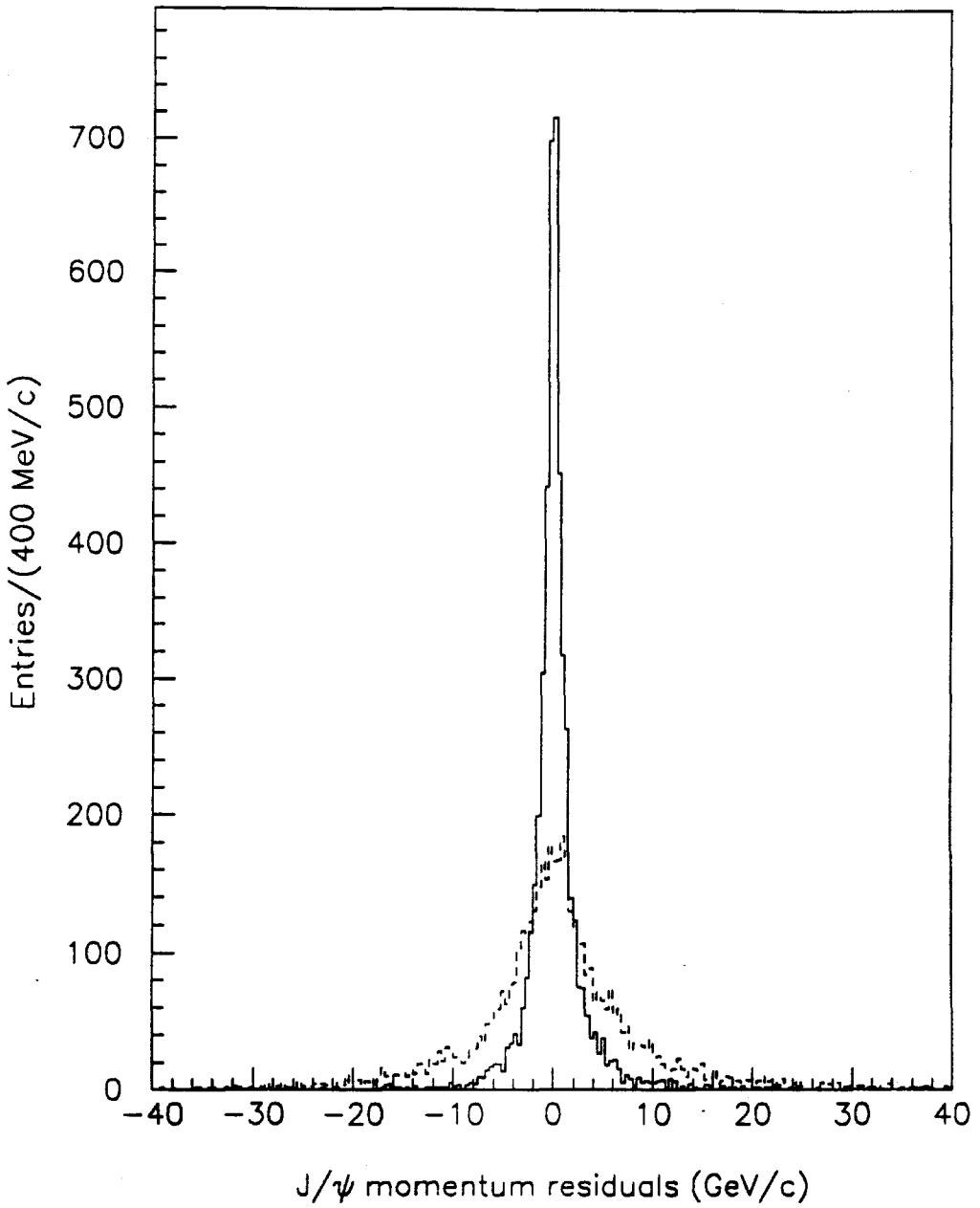

Figure A.5. Difference between reconstructed and generated J/ψ momentum for Monte Carlo B decays. The solid line is the distribution as determined by the J/ψ vertex fitting procedure, while the dashed is that for the initial vertex and track finding.

REFERENCES

1. P. Nason, S. Dawson, and R. K. Ellis, Nucl. Phys. **B303**, 607 (1988); **B327**, 49 (1989).

2. E. L. Berger, "Heavy Flavor Production", ANL-HEP-CP-88-26, June 1988.

3. J. C. Collins, D. E. Soper, and G. Sterman, Nucl. Phys. **B263**, 37 (1986).

4. E. L. Berger, "Heavy Quark Production in Hadron Collisions", ANL-HEP-CP-87-53, June 1987.

5. P. Mazzanti, and S. Wanda, Phys. Rev. **D26**, 602 (1982).

6. W. A. Bardeen, A. Buras, D. W. Duke, and T. Muta, Phys. Rev. **D18**, 3998 (1978).

7. J. F. Owens, Phys. Rev. **D30**, 943 (1984).

8. WA78 Collab., Phys. Lett. **B158**, 186 (1985).

9. ARGUS Collab., Z. Phys. **C43**, 543 (1990).

10. P. Shipsey, "*B* Physics with CLEO", PU-91-654, May 1991.

11. V. Sharma, "A Review of *b* Physics at LEP", to be published in the proceedings of the DPF92 conference, Nov. 1992.

12. UA1 Collab., Phys. Lett. **B256**, 121 (1991).

13. A. Sansoni "*B*-Physics at CDF", Proceedings of the XXVI Rencontre de Moriond, March 1991.

14. UA1 Collab., Phys. Lett. **B213**, 405 (1988).

15. CDF Collab., "Inclusive J/ψ, $\psi(2S)$, and *b*-quark Production in $p\bar{p}$ Collisions at $\sqrt{s}$ = 1.8 TeV", FERMILAB-Pub-92/236-E, Aug. 1992.

16. CDF Collab., Phys. Rev. Lett. **B68**, 3403 (1992).

REFERENCES (continued)

17. UA1 Collab., Phys. Lett. **B273**, 540 (1991).

18. NA10 Collab., Z. Phys. **C39**, 7 (1986).

19. NA10 Collab., Phys. Lett. **B187**, 431 (1987); **B202**, 453 (1988).

20. WA78 Collab., " Inclusive $B\overline{B}$ Cross-Section in 320 GeV π^- Uranium Interactions", CERN-EP/89-118, Sept. 1989.

21. E653 Collab., Nucl. Instr. & Meth. **A289**, 146 (1990).

22. R. A. Sidwell (for the E653 Collaboration), Proceedings of 1991 Vancouver Particles and Fields Meeting, D. Axen, D. Bryman, and M. Comyn eds. 516 (World Scientific, 1992).

23. E672 Collab., FERMILAB-Pub-91/62-E, Mar., (1991).

24. E706 Collab., "Production of Direct Photons and Neutral Mesons at Large Transverse Momenta by π^- and p Beams at 500 GeV/c", in preparation.

25. I. Kourbannis, Ph.D. Thesis, Northeastern University, Boston, (1990).

26. E706 Collab., Nucl. Inst. and Meth. **A279**, 272 (1989).

27. S. Mani, Ph.D. Thesis, The University of Pittsburgh, Pittsburgh, Pennsylvania, (1982).

28. ZIPTRACK Manual, FNAL Computing Department, publication PN267.0 (1983).

29. S. Easo, Ph.D. Thesis, Pennsylvania State University, Pennsylvania, (1989).

30. R. Crittenden, R. Li "An introduction to the Mu-B MWPC", E672 note, (1989).

31. Nanometric Systems, Inc., Multi Wire Proportional Chamber Readout System, Oak Park, Illinois.

32. E672 Collab., Nucl. Inst. and Meth. **185**, 75 (1981).

33. P. Draper, Ph.D. Thesis, Indiana University, Indiana, (1987).

REFERENCES (continued)

34. C. Yosef, Ph. D. Thesis, Northeastern University, Massachusets, (1990).

35. E672 Collab., Nucl. Instr. and Meth. **A270**, 99 (1988).

36. "2738 PCOS III Manual", Lecroy Research Systems Corporation, (1982).

37. R. Crittenden,"High-Mass Dimuon Trigger Processor", E672 note no. 111, (1986).

38. "Vaxonline System", Fermilab Computing Department, PN252.0, (1982).

39. V. Sirotenko, E672 internal note.

40. "Bison Interrupt and Gate Control",Fermilab Computing Department, HN-3.2, (1984).

41. H. J. Martin, "Fits to the Muon Data", E672 note no. 221, (1988).

42. R. Li, Ph. D. Thesis, Indiana University, Indiana, (1993).

43. MARK III Collab., Phys. Rev. Lett. **68**, 282 (1992).

44. R. Brun, "GEANT3 User's Guide", CERN DD/EE/84-1, (1984).

45. R. Stanton, "Measurement of Lifetimes of Charged and Neutral beauty Hadrons from Fermilab E653", to be published in the proceedings of the DPF92 conference, Nov. 1992.

46. J. Bell, Journal Phys. Rev. **D19** 1 (1978).

47. V. Sirotenko, "Estimation of Background to B-Signal Due to J/ψ Production in Secondary Interactions", E672 Note, (1988).

48. Review of Particle Properties, Phys. Rev. D45, (1992)

49. R. Jesik, E672 internal note.

50. P. Billoir, R. Fruhwirth, M. Regler, Nuc. Inst. and Meth. in Phys. Res., A241 115 (1985).

51. Frodesen, Skjeggestadt, and Tofte, "Probability and Statistics in Particle Physics", Universitetsforlaget, 259 (1979).

VITA

RICHARD JESIK

Education

1993 Ph.D., Physics, University of Illinois at Chicago, Chicago IL
1990 M.S., Physics, University of Illinois at Chicago, Chicago IL
1987 B.S., Physics/Astronomy, Wichita State University, Wichita KS
1981-82 Northwestern University, Evanston IL

Professional Affiliations

1992 - Society of the Sigma Xi (national research honorary society)
1990 - American Physical Society: Division of Particles and Fields
1988 - Sigma Pi Sigma (national physics honorary society)
1983-90 Society of Physics Students (chapter President; U.I.C. 1989, W.S.U. 1985)

Research Experience

RESEARCH ASSISTANT

1988 - Department of Physics,University of Illinois at Chicago, Fermilab experiment E672

Teaching Experience

LECTURER

1993 Physics Department, University of Illinois at Chicago
1991 Physics Department, North Park College, Chicago IL

TEACHING ASSISTANT

1987-90 Physics Department, University of Illinois at Chicago
1987 Department of Physics and Astronomy, Wichita State University

Presentations

"Hadronic Production of Beauty"
XXVIII Rencontres de Moriond, Les Arcs, France, Mar. 24, 1993.

"Hadroproduction of Heavy Quarks, Results from E672"
Fermilab Joint Experimental Theoretical Physics Seminar (*Wine and Cheese*), Aug. 28, 1992, and University of Illinois at Chicago High Energy Physics Seminar, Nov. 16, 1992.

"Heavy Flavor Production in π^--A Collisions at 530 *GeV/c*"
XXVI International Conference on High Energy Physics, Dallas, TX, Aug. 8, 1992.

"Fermilab Experiment E672"
Poster session, annual DOE review of the Fermilab physics program, Fermilab, Mar. 31, 1992

"Inclusive Hadron Production of J/ψ and Associated Particles"
1991 Division of Particles and Fields conference, Vancouver, B.C., Aug. 20, 1991.

"J/ψ Hadroproduction"
University of Illinois at Chicago High Energy Physics Seminar, Nov. 12, 1990.

Publications

"Hadronic Production of Beauty"
R. Jesik (for the E672/E706 Collab.), to be published in the Proceedings of the XXVIII Rencontres de Moriond, Les Arcs, France, Mar. 20-27, 1993.

"Heavy Flavor Production in π^--A Collisions at 530 *GeV/c*"
R. Jesik (for the E672/E706 Collab.), in "Proceedings of the XXVI International Conference on High Energy Physics", Dallas, TX, Aug. 6-12, ed. J. Sanford, (American Institute of Physics, 1993), p. 824.

"Inclusive Hadron Production of J/ψ and Associated Particles"
R. Jesik (for the E672/E706 Collab.), in "The Vancouver Meeting", Proceedings of 1991 DPF Conference, Vancouver B.C., Aug. 18-22, 1991, eds. David Axen, D. Bryman, M. Comyn, (World Scientific publishing co., Singapore, 1992), p. 696.

"Properties of J/ψ Production in π^--Be and p-Be Collisions at 530 GeV/c"
E672/E706 Collab., Fermilab PUB-91/62-E, 1991.

"Hadronic Production of B mesons"
L. Dauwe (for the E672/E706 Collab.), to be published in the Proceedings of the 1992 DPF Conference, Batavia, IL, Nov. 9-14, 1992.

"Hadronic Production of χ_c mesons"
H. Mendez (for the E672/E706 Collab.), to be published in the Proceedings of the 1992 DPF Conference, Batavia, IL, Nov. 9-14, 1992.

"Production of χ states in π^--Nucleus Collisions at 530 *GeV/c*"
A. Zieminski (for the E672/E706 Collab.), in "Proceedings of the XXVI International Conference on High Energy Physics", Dallas, TX, Aug. 6-12, ed. J. Sanford, (American Institute of Physics, 1993), p. 1062.

"Hadroproduction of Vector Mesons and χ_c States in the Collisions of 530 *GeV/c* Pions with Nuclear Targets"
R. Li (for the E672/E706 Collab.), in the Proceedings of the XXVII Rencontres de Moriond, Les Arcs, France, Mar. 22-28, 1992, p. 385.

"Hadronic Production of Vector Mesons by 530 *GeV/c* Pions"
R. Li (for the E672/E706 Collab.), in "The Vancouver Meeting", Proceedings of 1991 DPF Conference, Vancouver B.C., Aug. 18-22, 1991, eds. David Axen, D. Bryman, M. Comyn (World Scientific publishing co., Singapore, 1992) , p. 699.

"Production of Vector Mesons in Hadron-A Interactions "
A. Zieminski (for the E672/E706 Collab.), in the Proceedings of IVth Conference on Intersections between Particle and Nuclear Physics, Tuscon, AZ, 1991, p. 891.

"Effects of a Hadron Irradiation on Scintillating Fibers"
Solenoid Detector Collaboration Fiber Tracking Group, to be published in the Proceedings of the IEEE Conference, Orlando, FL Oct. 26-30 1992.